



Studies of the Statistical Bias and Signal Characteristics of Laser Velocimeters

**D. O. Barnett and T. V. Giel, Jr.
ARO, Inc.**

January 1980

Final Report for Period July 1976 — September 1977

Approved for public release; distribution unlimited.

**ARNOLD ENGINEERING DEVELOPMENT CENTER
ARNOLD AIR FORCE STATION, TENNESSEE
AIR FORCE SYSTEMS COMMAND
UNITED STATES AIR FORCE**

NOTICES

When U. S. Government drawings, specifications, or other data are used for any purpose other than a definitely related Government procurement operation, the Government thereby incurs no responsibility nor any obligation whatsoever, and the fact that the Government may have formulated, furnished, or in any way supplied the said drawings, specifications, or other data, is not to be regarded by implication or otherwise, or in any manner licensing the holder or any other person or corporation, or conveying any rights or permission to manufacture, use, or sell any patented invention that may in any way be related thereto.

Qualified users may obtain copies of this report from the Defense Technical Information Center.

References to named commercial products in this report are not to be considered in any sense as an indorsement of the product by the United States Air Force or the Government.

This report has been reviewed by the Office of Public Affairs (PA) and is releasable to the National Technical Information Service (NTIS). At NTIS, it will be available to the general public, including foreign nations.

APPROVAL STATEMENT

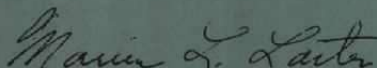
This report has been reviewed and approved.



MARSHALL K. KINGERY
Project Manager
Directorate of Technology

Approved for publication:

FOR THE COMMANDER



MARION L. LASTER
Director of Technology
Deputy for Operations

UNCLASSIFIED

REPORT DOCUMENTATION PAGE		READ INSTRUCTIONS BEFORE COMPLETING FORM
1 REPORT NUMBER AEDC-TR-78-65	2 GOVT ACCESSION NO.	3 RECIPIENT'S CATALOG NUMBER
4 TITLE (and Subtitle) STUDIES OF THE STATISTICAL BIAS AND SIGNAL CHARACTERISTICS OF LASER VELOCIMETERS		5 TYPE OF REPORT & PERIOD COVERED Final Report - July 1976 - September 1977
		6 PERFORMING ORG REPORT NUMBER
7 AUTHOR(s) D. O. Barnett and T. V. Giel, Jr., ARO, Inc., a Sverdrup Corporation Company		8 CONTRACT OR GRANT NUMBER(s)
9 PERFORMING ORGANIZATION NAME AND ADDRESS Arnold Engineering Development Center/DOT Air Force Systems Command Arnold Air Force Station, Tennessee 37389		10. PROGRAM ELEMENT, PROJECT, TASK AREA & WORK UNIT NUMBERS Program Element 65807F
11 CONTROLLING OFFICE NAME AND ADDRESS Arnold Engineering Development Center/DOS Air Force Systems Command Arnold Air Force Station, Tennessee 37389		12. REPORT DATE January 1980
14 MONITORING AGENCY NAME & ADDRESS (if different from Controlling Office)		13. NUMBER OF PAGES 145
		15. SECURITY CLASS. (of this report) UNCLASSIFIED
		15a. DECLASSIFICATION/DOWNGRADING SCHEDULE N/A
16 DISTRIBUTION STATEMENT (of this Report) Approved for public release; distribution unlimited.		
17 DISTRIBUTION STATEMENT (of the abstract entered in Block 20, if different from Report)		
18 SUPPLEMENTARY NOTES Available in Defense Technical Information Center		
19 KEY WORDS (Continue on reverse side if necessary and identify by block number) laser velocimeters turbulent flow accuracy signals chemical reactions recognition data acquisition bias instrumentation		
20 ABSTRACT (Continue on reverse side if necessary and identify by block number) Analyses are presented of (1) the statistical bias of individual realization laser velocimeters (LV's) and (2) the theoretical signal amplitudes obtained from dual-scatter (fringe) LV's. The analyses are compared to experimental data obtained from a subsonic, confined, seeded jet. The statistical bias study reviews the various formulations relating LV sampling characteristics to the velocity field and shows that, theoretically, bias is reduced by random sampling, introduction of fixed-time delays between samples, and nonuniformities in		

UNCLASSIFIED

UNCLASSIFIED

20. ABSTRACT (Continued)

seeding. These concepts are tested by a bias simulation program which simulates LV response to a turbulent flow by applying various sampling laws to hot-wire anemometer data. The finite-difference algorithms suggested by various investigators to eliminate bias from LV data fail if the sampling rate is less than the local integral time scale of the turbulent flow. Velocity data for the near field of a uniformly seeded subsonic jet exhausting into a plenum were obtained by pitot probes, hot-wire anemometers, and a Bragg-diffracted laser velocimeter. No consistent bias of the data was observed, indicating that routinely correcting LV data for statistical bias may lead to significant errors. The signal amplitude study considers the feasibility of discriminating against LV data from large particles by the signal amplitude observed by the Doppler data processor (DDP). Accordingly, the Mie scattering from particles traversing the nonuniformly illuminated probe volume is computed to determine representative light intensities incident on the photomultiplier tube (PMT). Amplification of the signal by the PMT and other sources of signal gain are considered to determine signal voltage at the DDP. Signal amplitude data obtained from LV measurements in the subsonic jet are presented for a range of particle sizes and compared to the analysis. It is concluded that the discrimination technique will discriminate qualitatively against large particles, but will yield uncertain results for light at visible wavelengths if particles are sized by this method.

UNCLASSIFIED

PREFACE

The work described herein was conducted by Headquarters, Arnold Engineering Development Center (AEDC), Air Force Systems Command (AFSC). The results were obtained by ARO, Inc., AEDC Division, a Sverdrup Corporation Company, contract operator of AEDC, AFSC, Arnold Air Force Station, Tennessee. The work was done under ARO Projects No. R32P-D9A and P32S-V4A, and the manuscript was submitted for publication on September 19, 1978.

Appreciation and acknowledgement are extended to B. P. Curry, ARO, Inc., for his assistance on a diversity of topics relating to the Mie scattering calculations and to E. W. Dorrell, Jr., ARO, Inc., who programmed the signal amplitude code presented in an appendix to this report.

A portion of the information contained in this report was submitted by T. V. Giel, Jr., formerly with ARO, Inc., in his dissertation to the University of Notre Dame in partial fulfillment of the requirements for the degree of Doctor of Philosophy.

CONTENTS

	<u>Page</u>
1.0 INTRODUCTION	7
1.1 Background	8
1.2 Scope of the Investigation	12
2.0 STATISTICAL BIAS STUDY	
2.1 Theoretical Considerations	14
2.2 Experimental Simulation	23
2.3 Results	34
2.4 Analysis of Influential Factors	56
3.0 SIGNAL AMPLITUDE STUDY	
3.1 MIE Scattering Characteristics	73
3.2 Signal Amplification	98
3.3 Experimental Signal Levels	103
3.4 Particle Sizing and Discrimination	107
4.0 CONCLUSIONS	114
REFERENCES	116

ILLUSTRATIONS

Figure

1. Dual-Scatter Laser Velocimeter	9
2. Estimated Bias for Arithmetic Mean Velocity and Turbulent Intensity	20
3. Bias of the Axial Velocity Component in Turbulent Flows ($S = 0$)	22
4. Fluidized Bed Seeder	25
5. Test Apparatus	26
6. Laser Velocimeter and Traverse System	28
7. Hot-Wire Anemometer Calibration	34
8. Histograms of Particle Interarrival Times	36
9. Data Rate Variation in Jet Near Field	37
10. Particle Size Distribution	39

<u>Figure</u>	<u>Page</u>
11. Hot-Wire Measurements of Axial Velocity Distributions	42
12. Hot-Wire Measurements of Local Turbulence Intensities	47
13. Radial Variation of Integral Time Scales	49
14. Radial Distribution of Skew Coefficient	50
15. Radial Distribution of Axial Kurtosis Coefficient	51
16. Comparison of IRLV Mean Velocity with "Biased" Predictions	52
17. Comparison of IRLV and Hot-Wire Local Turbulence Intensities	54
18. Centerline Distribution of Axial Velocities and Turbulence Intensities	55
19. Effect of Data Randomization	57
20. Simulation Program Predictions of Sampling Rate Effect on the Velocity Bias of a Sinusoidal Flow	60
21. Simulation Program Predictions of the Velocity Bias of a Turbulent Flow	63
22. Bias Reduction Resulting from Minimum Processing Time	68
23. Magnitude of Mean Velocity Bias for Particle Concentration Fluctuations	72
24. Magnitude of Turbulent Intensity Bias for Fluctuations in Particle Concentration	72
25. Mie Scattering Coordinate System	75
26. Variation of Mie Intensity with Particle Size Parameter for Water Droplets ($m = 1.33$)	78
27. Effect of Refractive Index on Mie Intensity Function in Forward Scatter ($\theta = 0$ deg)	80
28. Effect of Refractive Index on Normalized Mie Intensity in Backscatter ($\theta = 180$ deg)	81
29. Effect of Scattering Angle on Intensity Functions ($\alpha = 3.05$)	82
30. Effect of Scattering Angle on Intensity Functions ($\alpha = 12.21$)	85

<u>Figure</u>	<u>Page</u>
31. Effect of Lens f-Number on Scattering Function ($\alpha = 3.05$)	88
32. Effect of Lens f-Number on Scattering Function ($\alpha = 12.2$)	89
33. Probe Volume Coordinate System	91
34. Intensity Variation in the Probe Volume ($X_1^* = 0$)	92
35. Variation of Average Illuminating Intensity with Probe Volume Location	95
36. Effect of Particle Size on Light Scattered for Forward-Scatter System	96
37. Effect of Particle Size on Light Scattered for Backscatter System	97
38. PMT Calibration Arrangement	100
39. PMT Amplification for Several Power Supply Voltages	101
40. Effect of Supply Voltage on PMT Current Amplification	102
41. PMT Saturation Levels	104
42. Histogram of Oleic Acid Signal Amplitudes	106
43. Effect of Particle Size on Signal Amplitude	108
44. Signal Level Variation with Illuminating Intensity	110
45. Signal Amplitude Variation with Size for Several Particulates	111
46. Effect of Illuminating Intensity on Signal Amplitudes for Several Particulates	112

TABLES

1. Precision Uncertainty of Laser Velocimeter	29
2. Jet Flow-Field Data	41

APPENDIXES

A. Relationship Between Short- and Long-Term Averages	127
B. MIELV Program	129
C. Probe Volume Intensity Program (PVIP)	134
NOMENCLATURE	137

1.0 INTRODUCTION

Much of the testing and research at Arnold Engineering Development Center (AEDC) evaluates quantitatively the flows characteristic of reactive propulsion systems. Although the range of conditions experienced in such studies is diverse, extremely high velocities, turbulence levels, and temperatures are often encountered in a single, chemically reacting medium. In recent years attention has been given, therefore, to nonintrusive instrumentation systems which can determine the velocity, density, temperature, or species concentration in such flows without contact with the fluid medium.

Particular attention has been given to techniques for determining the nature of the velocity field in turbulent shear flows since convection mechanisms contribute to the development of the temperature field and chemical reactions and to the thrust of a propulsive device. The predominant nonintrusive instrument for this purpose, the laser velocimeter (LV), has been used to measure (1) the mean velocity and turbulence structure in heated and unheated jets at velocities ranging from the low-subsonic to near-hypersonic regimes (Refs. 1 and 2), (2) the recirculation and mixing in reacting, coaxial hydrogen-air jets (Refs. 3 and 4), (3) the fully developed turbulent pipe flows (Ref. 1), and (4) the change in centerline exhaust velocity of a large turbofan engine with throttle setting (Ref. 5).

Although each of these experiments was successful in meeting its stated objectives, a critical assessment of various factors influencing the results revealed many potential sources of error in the measurements. Specifically, the accuracy of the data may be influenced by (1) the LV design, (2) experimental procedures, (3) data acquisition and reduction techniques, (4) Instrumentation uncertainties, and (5) particle dynamics effects. Detailed discussions of these possible errors are given in several AEDC publications (Refs.

1, 2, and 6 through 10) and in the open literature (Refs. 11 through 14). The present study, however, concerns the elimination of two sources of possible serious errors--statistical bias and large particle lags. Since the overall LV development at AEDC includes development of burst processors (Refs. 15 and 16) as well as LV utilization, the topics of statistical bias and large-particle discrimination techniques apply to the entire scope of laser velocimetry at AEDC.

1.1 BACKGROUND

A dual-scatter laser velocimeter, such as shown in Fig. 1, consists of (1) a laser, which provides a monochromatic, coherent light source, (2) illuminating optics, which split the laser beam into two or more essentially equal intensity beams then refocus them to form an optical probe volume, (3) collector optics, which collect light scattered by particles traversing the interference fringes established in the probe volume, and (4) system electronics, which amplify the signals and determine the frequency, f_D , at which the particles intercept the fringes. Since the fringe spacing, K_δ , is determined solely by the illuminating optics (see Ref. 17), the particle velocity normal to the plane of the fringes, V , is simply the product $K_\delta f_D$. If the particles are small enough to nearly duplicate the spatial and temporal variations of the fluid velocity, an extremely accurate measurement of local fluid velocity can be obtained.

When the concentration of particles large enough to be detected by the LV is low, as in most gaseous flows, data will be obtained intermittently as single particles are swept through the probe volume. In studying the sampling characteristics of laser velocimeters operated in such an individual realization mode, Mayo (Ref. 18) observed that the interval between particle arrivals was described by a Poisson probability distribution having a rate parameter which was proportional to the flux of particles passing through the probe volume. He con-

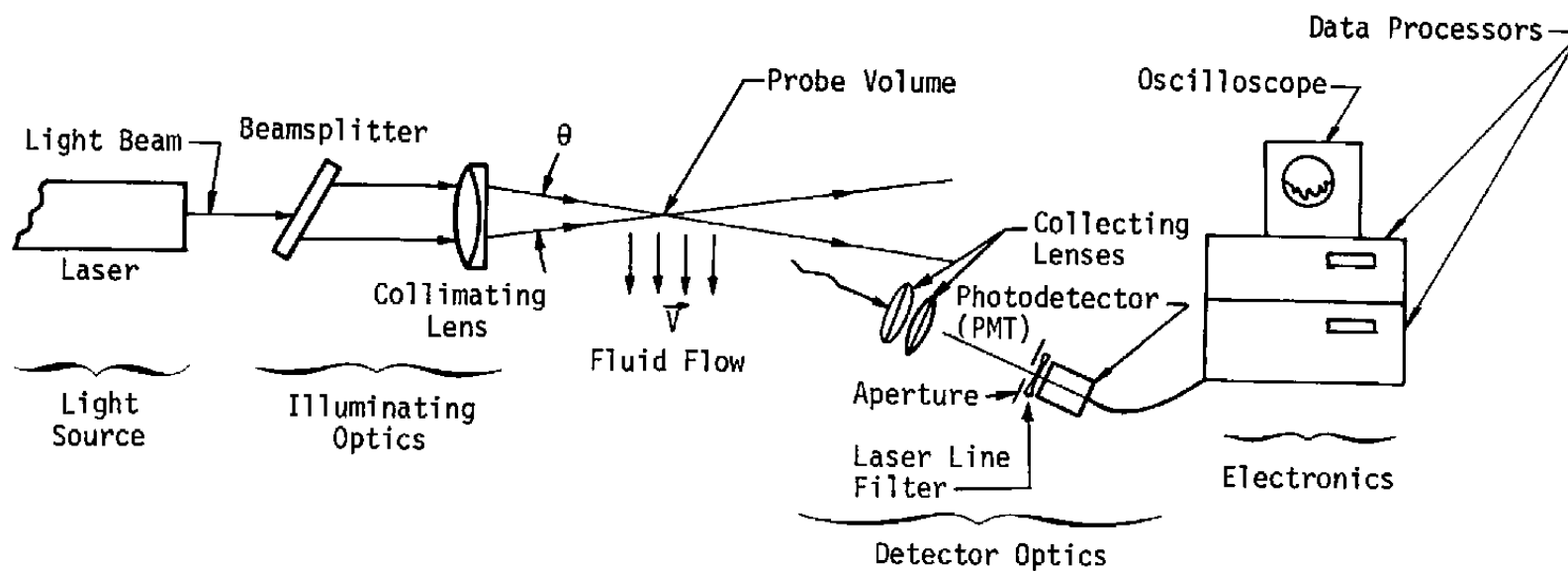


Figure 1. Dual-scatter laser velocimeter.

cluded that, since the sampling rate and measured velocity were inter-related, individual realization laser velocimeters (IRLV's) would overestimate the mean velocity at a point. A similar conclusion was independently reached by McLaughlin and Tiederman (Ref. 19), who termed the phenomenon statistical bias. Barnett and Bentley (Ref. 20) showed that the mean velocity was biased in direct proportion to the turbulence intensity, thus identifying a potentially serious source of error in shear flows.

Since the publication of these pioneering studies, considerable research has been devoted to determining the conditions under which bias occurs and to developing data acquisition or processing techniques to eliminate bias (Refs. 21 through 25). Considerably less work has been devoted to the experimental verification of the magnitude of bias (Refs. 26 and 27). Data obtained at AEDC (Ref. 1) have, moreover, not shown any conclusive evidence that the theoretically predicted bias exists. Despite this lack of experimental verification many experimentalists routinely correct IRLV data for bias and some commercial burst counters developed for LV applications (Ref. 28) process IRLV data using algorithms developed to remove bias.

The magnitude and existence of statistical bias are of particular concern to the LV development activities at AEDC since (1) data obtained in turbulent and transient flows could be especially influenced by bias and (2) burst processor development activities should consider direct removal of any significant data biases.

In using an IRLV, a data set containing measurements of the velocity of many individual particles is obtained. The response of each particle to the spatial or temporal velocity variations in the fluid is dictated by the trajectory, shape, size, and density of the particle. If these parameters could be controlled for all particles in a data set, it would be possible to accurately predict

how closely the LV measurements correspond to the actual fluid velocity at a point. In applications where the flow is seeded with a single size and type of particle, this condition may be approached but not reached because of particle agglomeration or the presence of other particles in the fluid. Other applications preclude active seeding of the flow so that natural particulates of widely varying properties contribute to a data set.

Ideally, then, an IRLV should measure particle size as well as velocity if the best accuracy of the instrument is realized. Significant advances in particle size determination by laser velocimetry have been made by Farmer (Ref. 29) and later by Roberds (Ref. 30). In both studies, the signal visibility of the individual Doppler burst is determined and related to the particle size through scattering theory. Under carefully controlled conditions (Ref. 29), the visibility is independent of index of refraction and the dimension of the particle normal to the probe volume fringe planes can be determined. Such results, however, are not unique if the visibility is low, i.e., a single visibility value is characteristic of several particle sizes. The visibility method is at present additionally limited to relatively low frequencies (10 MHz or less), making it of limited utility since high velocities or acousto-optical modulation (Ref. 31) of the signal to determine flow direction can lead to much higher signal frequencies. Recently, moreover, several investigations (Refs. 32, 33, and 34) have raised serious questions as to the validity of the visibility concept in backscatter applications.

Because of these limitations, use of signal visibility to determine particle size is not presently suitable for many applications. If, however, the criterion of simultaneous particle size and velocity determination is relaxed, an alternate approach may be considered. Reference 2 presents LV data obtained from a highly accelerated (1.3×10^4 ft/sec²), naturally seeded flow. In many cases there were

such wide variations in measured velocities in each data set that the mean velocity was useless as an indicator of local fluid velocity. Note, however, that the upper velocity limit of the measured probability distributions approached the gas velocity in acceleration regions, whereas the lower limit was near the gas velocity after a sudden deceleration. Since these results are typical of the particle dynamic behavior of an ensemble of particles having a wide distribution of sizes and shapes, an appreciable increase in LV accuracy may result if signals arising from large particles can be excluded from a data set.

Andrews and Seifert (Ref. 35) attempted to size particles by the amplitude of light scattered by a reference-beam LV. Pfeiffer and von Stein (Ref. 36) reported that discriminating against signals whose amplitude exceeded a predetermined threshold value led to significant improvements in dual-scatter LV accuracy in accelerated flows. Again, the instrument manufacturers (Ref. 28) seized on these results and have produced data processors that incorporate signal amplitude discriminators. Unfortunately, these studies do not provide the detail necessary for, *a priori*, accurately estimating the particle sizes being excluded from consideration in obtaining data. If the threshold is set too low, data acquisition rates are adversely affected, and too high a setting will allow too many large particles to be considered. Moreover, the complexity of the Mie scattering process is such that a slight variation in either the particle characteristics or the LV system could significantly alter the results. Although the concept of discrimination on the basis of signal amplitude is intuitively and operationally attractive, further study is warranted before incorporating this concept into future LV systems and processors.

1.2 SCOPE OF THE INVESTIGATION

The present analytical and experimental study was undertaken to determine (1) the magnitude of statistical bias in individual realization

laser, velocimeter data and (2) the suitability of discriminating against signals from large particles on the basis of signal amplitude. Because of the importance of these concepts in obtaining improved measurements in the shear flows prevalent in many tests, the experimental data were obtained in the shear layer formed by a subsonic jet exhausting into a quiescent medium. To minimize the uncertainty of particle dynamic effects on the data, all particulates exceeding $0.1\text{ }\mu\text{m}$ in diameter were filtered from the air supply and the flow then seeded with particles having known characteristics by either a fluidized bed seeder or aerosol generator. Entrainment of particles from the ambient air was reduced by confining the developing jet flow field within an enclosure having transparent walls to permit LV utilization. The length of the enclosure was chosen to enhance recirculation along the edge of the jet, thus increasing uniformity of seed concentration across the jet.

In Section 2.0, pitot-static, hot-wire, and one-component LV data of the axial and radial variation of velocity and turbulence intensity in the jet near field are presented for axial location to nozzle exit diameter ratios of 2, 4, 6, and 8. The data are compared to statistical bias theories and a bias simulation program developed for the studies to determine (1) the magnitude of statistical bias, (2) its relationship to seeding rate and turbulence structure, and (3) the factors influential in the reduction of bias in jet flows.

Section 3.0 summarizes those conditions that influence the amplitude of signals detected by dual-scatter laser velocimeters. Specifically, the influence of particle size, index of refraction, illuminating intensity variation, and LV collector optics on the amplitude of the Mie scattering intensity at the phototube is discussed. Photomultiplier characteristics and other signal-amplification electronic components are then considered in arriving at the signal voltage level observed by the data processor. The theoretical signals are compared to those observed from the subsonic jet for particles of varying sizes. An

assessment of the potential for discriminating against large particles by signal amplitude discrimination is made.

2.0 STATISTICAL BIAS STUDY

To experimentally evaluate the magnitude of the statistical bias presumed present in IRLV measurements of the mean velocity and higher velocity moments, those flow conditions that lead to biased results must be identified and controlled. The bias observed in a given application depends upon the turbulence level, data acquisition system, data reduction procedure, and concentration of the particles from which the data are obtained. Moreover, bias can only be determined relative to other instrumentation systems. Therefore, the absolute accuracy of the LV and supporting instrumentation must be within certain bounds if the effect is to be observed.

2.1 THEORETICAL CONSIDERATIONS

The bias model proposed by Barnett and Bentley (Ref. 20) has been extended to identify the primary bias-creating flow conditions and the anticipated magnitude of the bias. This model was chosen because it leads directly to a quantitative assessment of the statistical bias and it directly relates arithmetic averages to the "unbiased" temporal averages which form the bias of many turbulent theories.

The temporal average of any moment, f , of the velocity may be obtained over an interval T from

$$\hat{f} = \frac{1}{T} \int_{t_0}^{t_0+T} f(t) dt \quad (1)$$

IRLV systems, however, measure the velocity only at those discrete times when a particle is crossing the LV probe volume, so that \hat{f} can only be approximated by a numerical integration such as

$$\bar{f} = \frac{\sum_{i=1}^M f_i \Delta t_i}{\sum_{i=1}^M \Delta t_i} \quad (2)$$

In Eq. (2) the f_i are velocity quantities evaluated for each of M discrete LV measurements and the Δt_i are the times separating the respective measurements. When the intervals between successive measurements are small, \bar{f} will be a good approximation of \hat{f} . The numerical integration will, furthermore, reduce to the arithmetic average of the IRLV data set under certain conditions. For example, if the interval between successive samples Δt_i is constant, Eq. (2) will reduce to

$$\bar{f} = \frac{1}{M} \sum_{i=1}^M f_i = \langle f \rangle \quad (3)$$

where the angle brackets denote the arithmetic average of f_i .

The nature of statistical bias in individual realization velocimetry is also evident from Eq. (2) since a Reynolds decomposition of the velocity moment and time interval into

$$f_i = \langle f \rangle + f'_i \quad (4)$$

$$\Delta t_i = \langle \Delta t \rangle + \Delta t'_i \quad (5)$$

allows the numerical approximation of the temporal average to be written

$$\bar{f} = \langle f \rangle [1 + R_{f\Delta t}] \quad (6)$$

where the correlation function is defined as

$$R_{f\Delta t} = \frac{1}{M} \sum_{i=1}^M \frac{f'_i \Delta t'_i}{\langle f \rangle \langle \Delta t \rangle} \quad (7)$$

It is apparent, then, from Eq. (6) that if a correlation exists between the velocity and the interarrival time between particles, the arithmetic average will be biased with respect to the approximate temporal average. On the other hand, if the velocity moment and time between samples, f_i and Δt_i , are statistically independent, as in the case where Δt_i is constant, the two averages are identical.

The relationship of the velocity, V_i , to the time interval, Δt_i , in a time-varying flow can be established under certain conditions. Accordingly, assume that (1) the particle number density (or concentration), N , is constant throughout the flow field, (2) the LV probe volume is spherical so that it presents a constant cross-sectional area, A , to all particles traversing it, (3) the fluid density, ρ , is constant, and (4) all particles are travelling at the fluid velocity (negligible lag). Then the number of particles that enters the probe volume in Δt_i is

$$\delta N_i = NA \int_{t_0}^{t_0 + \Delta t_i} V(t) dt = NA \Delta t_i \hat{V}_i \quad (8)$$

where \hat{V}_i is the mean fluid velocity during the time between successive samples, Δt_i . It is implicitly assumed in Eq. (8) that fluid is not recirculated through the probe volume so that each particle can enter the probe volume only once. If every particle velocity is processed by the LV (i.e., $\delta N_i = 1$), then the interarrival time and the mean fluid velocity during Δt_i are related by

$$\Delta t_i = \frac{1}{NA \hat{V}_i} \quad (9)$$

If Δt_i is small, then $V(t)$ is essentially constant over the interval and $\hat{V}_i \approx V_i$, the measured particle velocity, and from the discussion following Eq. (7) it is expected that the LV data set would be biased. For a time-varying flow, characterized by a single frequency, this condition is readily obtained if Δt_i is much less than the period of the flow oscillation. Turbulent flows, however, are typified by an

energy-cascading process extending over a spectrum of frequencies. Accordingly, it is more difficult to determine whether a relationship exists between data rate and the temporal velocity variation in turbulent flows, although such a relation clearly exists for simple flow pulsations. Some insight is gained if the variance of the flow velocities measured over Δt_i is compared to the variance of the instantaneous velocities. In Appendix A these variances are related by

$$\overline{(\hat{V}_i - \hat{V})^2} = \frac{2(\overline{V_i - \hat{V}})^2}{\Delta t_i} \int_0^{\Delta t_i} R(\tau) \left[1 - \frac{\tau}{\Delta t_i}\right] d\tau \quad (10)$$

where the autocorrelation coefficient is defined as

$$R(\tau) = \left[\overline{(V_i - \hat{V})^2}\right]^{-1} \lim_{T \rightarrow \infty} \int_0^T (V(t) - \hat{V})(V(t + \tau) - \hat{V}) dt \quad (11)$$

When all the Δt_i time intervals are sufficiently small $R(\tau)$ approaches unity for all τ much less than Δt_i (Ref. 37). Then it follows immediately from Eq. (10) that $\overline{(\hat{V}_i - \hat{V})^2} \approx \overline{(V_i - \hat{V})^2}$. An obvious condition leading to this equality is for the mean velocity over Δt_i to equal the measured velocity ($\hat{V}_i \approx V_i$) as noted earlier. Conversely, if all Δt_i are large enough that $R(\tau)$ approaches zero faster than τ approaches Δt_i , Eq. (10) reduces to

$$\overline{(\hat{V}_i - \hat{V})^2} \approx \frac{2L_T}{\Delta t_i} \overline{(V_i - \hat{V})^2} \quad (12)$$

where the integral time scale is defined by

$$L_T \equiv \lim_{T \rightarrow \infty} \int_0^T R(\tau) d\tau \quad (13)$$

The time intervals are much larger than the integral time scale then, so

from Eq. (12), the quantity $\overline{(\hat{V}_i - \hat{V})^2}$ approaches zero and, from the theorem of the mean (Ref. 37), the mean velocities averaged over the interarrival

times approach the temporal mean velocity. For this case Eq. (9) shows that the particle interarrival times are constant so that no bias of the velocity moments computed from IRLV data would be expected. The data rates are, however, too low for practical use of a laser velocimeter, as is shown below.

The magnitude of the expected bias may be estimated by considering the short interarrival time case which requires that Eq. (9) become

$$\Delta t_i = \frac{1}{NA V_i} \quad (14)$$

and, from Eq. (2),

$$\bar{f} = \frac{\sum_{i=1}^M f_i / V_i}{\sum_{i=1}^M 1 / V_i} \quad (15)$$

Note that for small Δt_i and a sufficiently large data set $\bar{f} = \hat{f}$ is an accurate approximation so that the "true" temporal average and the finite-difference integration are equivalent. In the following, such equivalence is assumed. Therefore, the relation for $f_i = V_i$ is

$$\bar{f} = \bar{V} = \frac{1}{\langle \frac{1}{V} \rangle} \quad (16)$$

so that the fluid velocity is obtained from the harmonic average of the individual velocity measurements:

$$\bar{V} = \frac{1}{\langle \frac{1}{V} \rangle} = \frac{1}{\frac{1}{M} \sum_{i=1}^M \frac{1}{V_i}} \quad (17)$$

The more general case of the bias of the r^{th} central moment of velocity is readily obtained with Eq. (14) for short interarrival times if it is noted from the binomial theorem that

$$f_i = (V_i - \bar{V})^r \sum_{s=0}^r (-1)^s \binom{r}{s} V_i^{r-s} \bar{V}^s \quad (18)$$

where $\binom{r}{s}$ denotes the binomial coefficients. From Eqs. (15), (17), and (18), it follows that

$$\overline{(V - \bar{V})^r} = \sum_{s=0}^r (-1)^s \binom{r}{s} \langle V^{r-s+1} \rangle \bar{V}^{s+1} \quad (19)$$

For the second central moment $r = 2$ and Eq. (19) shows that arithmetic averages of the mean velocity are biased with respect to the temporal averages since

$$\langle V \rangle = \bar{V} (1 + \sigma_{\bar{V}}^2) \quad (20)$$

where the turbulence intensity is defined as

$$\sigma_{\bar{V}} = \sqrt{\frac{\overline{(V - \bar{V})^2}}{\bar{V}^2}} \quad (21)$$

Similarly, evaluating Eq. (19) for the third central velocity moment ($r = 3$) shows

$$\sigma_{\langle V \rangle} = \frac{\sigma_{\bar{V}}}{1 + \sigma_{\bar{V}}^2} (1 - \sigma_{\bar{V}}^2 + S \sigma_{\bar{V}}^{\frac{1}{2}})^{\frac{1}{2}} \quad (22)$$

where the skew coefficient is defined by

$$S = \frac{\overline{(V - \hat{V})^3}}{\left[\overline{(V - \hat{V})^2} \right]^{\frac{3}{2}}} \quad (23)$$

Consequently, the bias of any moment computed by arithmetic averages is proportional to the next higher moment of the velocity.

The estimated statistical bias of the mean velocity, $\langle V \rangle$, and turbulence intensity, $\sigma_{\langle V \rangle}$, when the average interval between realizations is much less than the flow integral time scale, is shown in Fig. 2. The arithmetic average velocity always overpredicts the temporal mean velocity, but the arithmetic turbulent intensity is

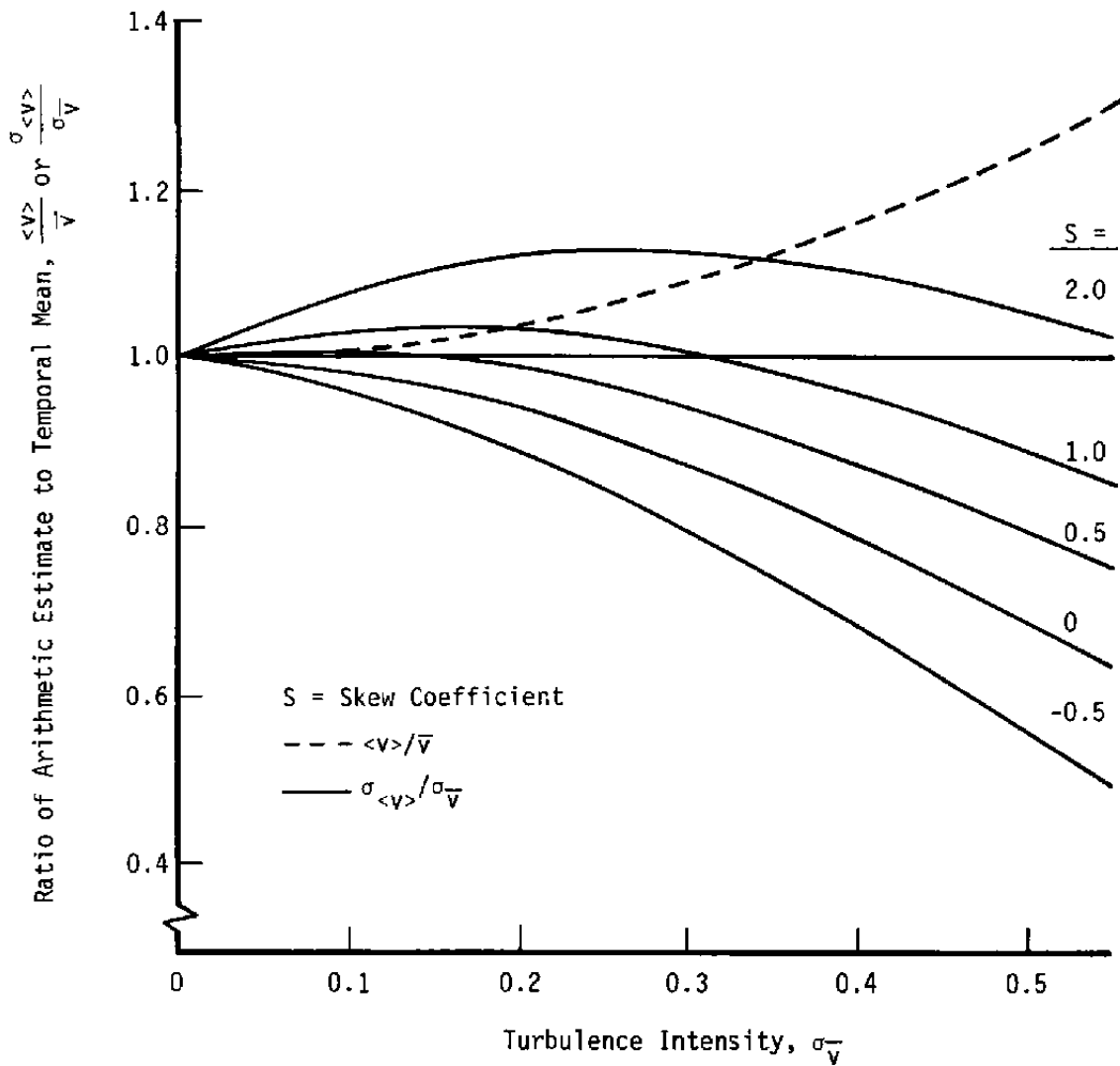


Figure 2. Estimated bias for arithmetic mean velocity and turbulent intensity.

strongly affected by the skewness of the velocity probability distribution. Note that for a Gaussian distribution of velocities ($S = 0$), local turbulent intensities computed from arithmetic averages will underestimate the true value.

The relationships derived above are valid only for a one-dimensional flow or an LV whose fringe system is normal to the local velocity vector because an LV with only one set of fringes responds to only one component of the velocity at a point. Since there are very few LV's that simultaneously respond to all three possible components of the velocity vector and turbulent flows are three dimensional in the fluctuation components of velocity, a more general relationship for turbulent flow measurements is useful. Consider a turbulent flow field in which the mean motion can be characterized primarily by a single component, U . The velocity vector at a point may then be written as

$$\vec{V}_i = (\langle U \rangle + u_i) \vec{i} + v_i \vec{j} + w_i \vec{k} \quad (24)$$

where u_i , v_i , w_i , are the fluctuation components along the coordinate axes defined by the orthogonal unit vectors (\vec{i} , \vec{j} , \vec{k}). The magnitude of the velocity vector is then

$$|\vec{V}_i| = \langle U \rangle \left(1 + 2 \frac{u_i}{\langle U \rangle} + \frac{u_i^2 + v_i^2 + w_i^2}{\langle U \rangle^2} \right)^{\frac{1}{2}} \quad (25)$$

Substituting Eq. (25) in Eq. (15) with $f_i = \langle U \rangle + u_i$ gives for the mean axial component measured by an LV system

$$\bar{U} = \langle U \rangle \frac{\sum_{i=1}^M \frac{\left(1 + \frac{u_i}{\langle U \rangle}\right)}{(1 + \alpha_i)^{\frac{1}{2}}}}{\sum_{i=1}^M \frac{1}{(1 + \alpha_i)^{\frac{1}{2}}}} \quad (26)$$

where

$$\alpha_1 = 2 \frac{u_1}{\langle U \rangle} + \frac{u_1^2 + v_1^2 + w_1^2}{\langle U \rangle^2} \quad (27)$$

Expanding Eq. (26) in a binomial series and truncating terms of third or higher order leads to

$$\langle U \rangle = \bar{U} \left(\frac{1 + \sigma_{\langle u \rangle}^2 - \frac{1}{2} (\sigma_{\langle v \rangle}^2 + \sigma_{\langle w \rangle}^2)}{1 - \frac{1}{2} (\sigma_{\langle v \rangle}^2 + \sigma_{\langle w \rangle}^2)} \right) \quad (28)$$

Figure 3 predicts the bias expected in turbulent flow IRLV measurements when $\sigma_{\langle v \rangle} = \sigma_{\langle w \rangle} = 2/3 \sigma_{\langle u \rangle}$ which Sami (Ref. 38) indicates are representative of the near field of a subsonic jet. The bias predicted

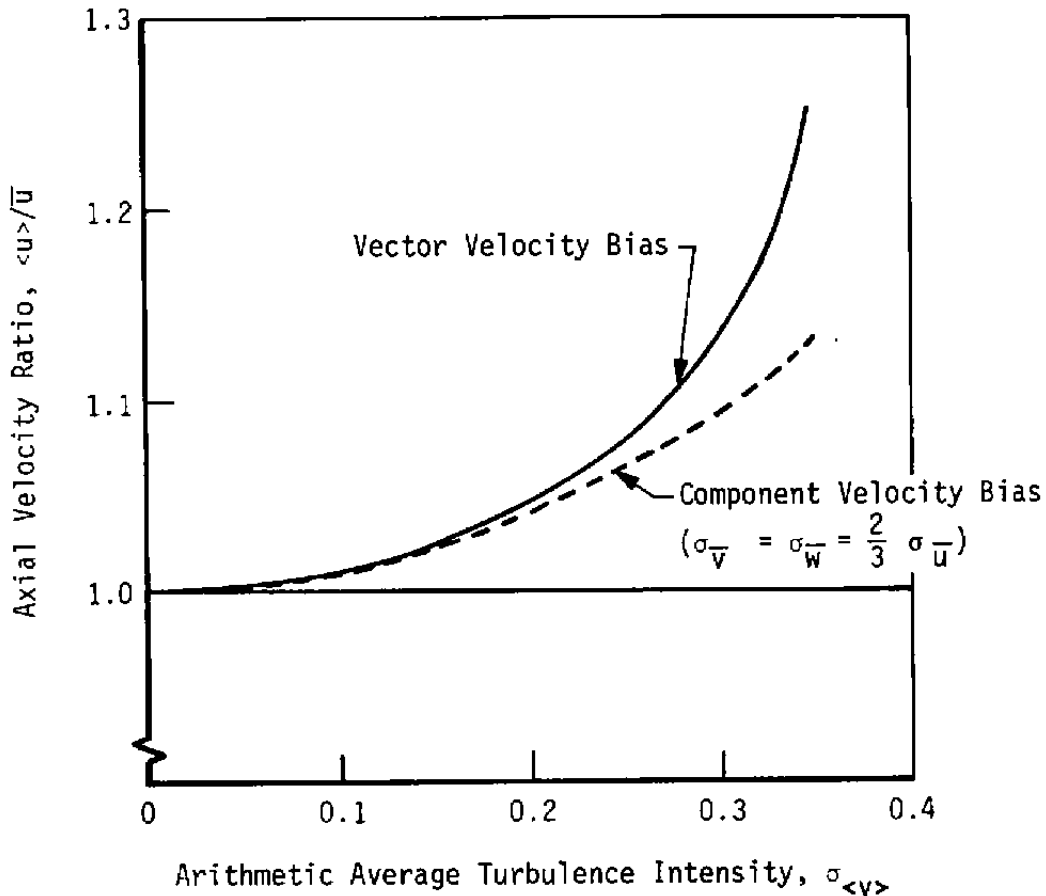


Figure 3. Bias of the axial velocity component in turbulent flows ($S = 0$).

for the arithmetically averaged component velocity is obviously less than the bias that would result in a one-dimensional flow. But, it is still large enough to be significant in many IRLV applications. Note that McLaughlin and Tiederman (Ref. 19) and Buchhave (Ref. 24) also show component bias to be generally less in three-dimensional than in one-dimensional flow.

Note that Eq. (28) is similar to the expression derived for a purely one-dimensional flow, Eq. (20), when the turbulent intensities associated with the (\vec{j}, \vec{k}) axes become negligible. However, the turbulent intensity associated with the bias in Eq. (28) is the arithmetic value rather than the temporal turbulent intensity. This is a consequence of the averaging techniques and truncations used in the derivation; but, as noted from Fig. 3, the error involved in the estimate is not large for turbulence levels of 30 percent or less. Since the binomial series will only converge for small values of α_1 , taking $\alpha_{<u>} = \alpha_u^-$ in Eq. (28) is not a restrictive assumption.

2.2 EXPERIMENTAL SIMULATION

With a relationship for the bias magnitude derived, the flow conditions desired in an experimental study of bias can be delineated. Specifically, the experiment must have (1) constant fluid density, (2) spatially and temporally invariant particle number density, (3) negligible particle-fluid lags, (4) single counting of each particle (i.e., rapid data acquisition system and negligible fluid recirculation) and (5) particles entering the probe volume frequently enough that \hat{V}_1 is approximately V_1 .

An air jet was selected for the experiments to provide a wide range of turbulent intensities in all component directions. Thus, arithmetic means of IRLV one-component data should be sufficiently biased for experimental identification in at least part of the flow. The jet exit

Mach number was kept below 0.1 to ensure that the fluid density could be considered constant. A fairly constant particle number density was obtained by filtering the supply air to remove all detectable particles and then seeding with a fluidized bed seeder (Fig. 4). Additionally, the jet was enclosed so that recirculation external to the jet tended to spatially equalize particle concentration.

By varying the supply pressure to the fluidized bed seeder the seed concentration was controlled and a range of particle interarrival times, Δt_1 , obtained. Based on particle dynamic calculations for the range of conditions in the jet, uniform 1- μ m-diam particles were used in the seeder because particles of that size accurately respond to fluid transients. Fluidized bed seeders will not provide a perfectly uniform particle concentration (Ref. 39); however, the vibrating seeder shown in Fig. 4 provided a more uniform particle number density than conventional seeders. The jet was also seeded with a Berglund-Liu monodisperse aerosol generator (Ref. 40) in a few of the tests, but this seeder could produce only low seed concentrations. Air from the seeder entered the jet stilling chamber after passing through a particle charge neutralizer. The neutralizer lessened particle agglomeration by minimizing electrostatic attraction, but some coagulation was observed in photomicrographs of particles collected from the test flow.

The stilling chamber and jet test apparatus is shown in Fig. 5. A coaxial mixer section of the stilling chamber mixed the seeded air with filtered air to establish the desired seed concentration. A shielded, self-aspirating, copper-constantan thermocouple and two static pressure ports in the center of the stilling chamber monitored the flow total conditions. A 25-to-1 area ratio contraction nozzle with a 2.54-cm-diam throat was at the end of the stilling chamber. The nozzle contour was matched to calculated potential flow streamlines to smoothly accelerate the air and particles to a uniform nozzle exit velocity.

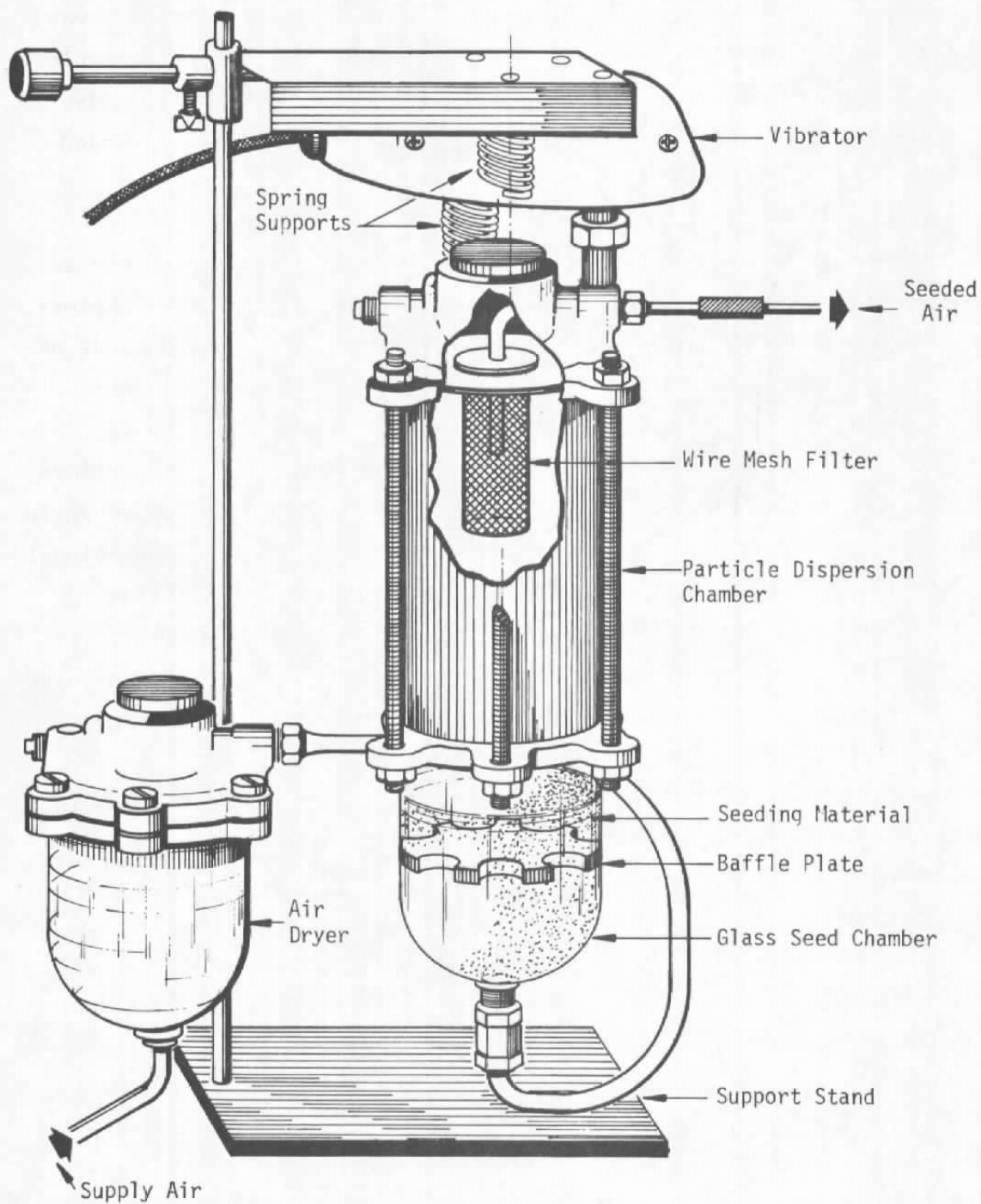


Figure 4. Fluidized bed seeder.

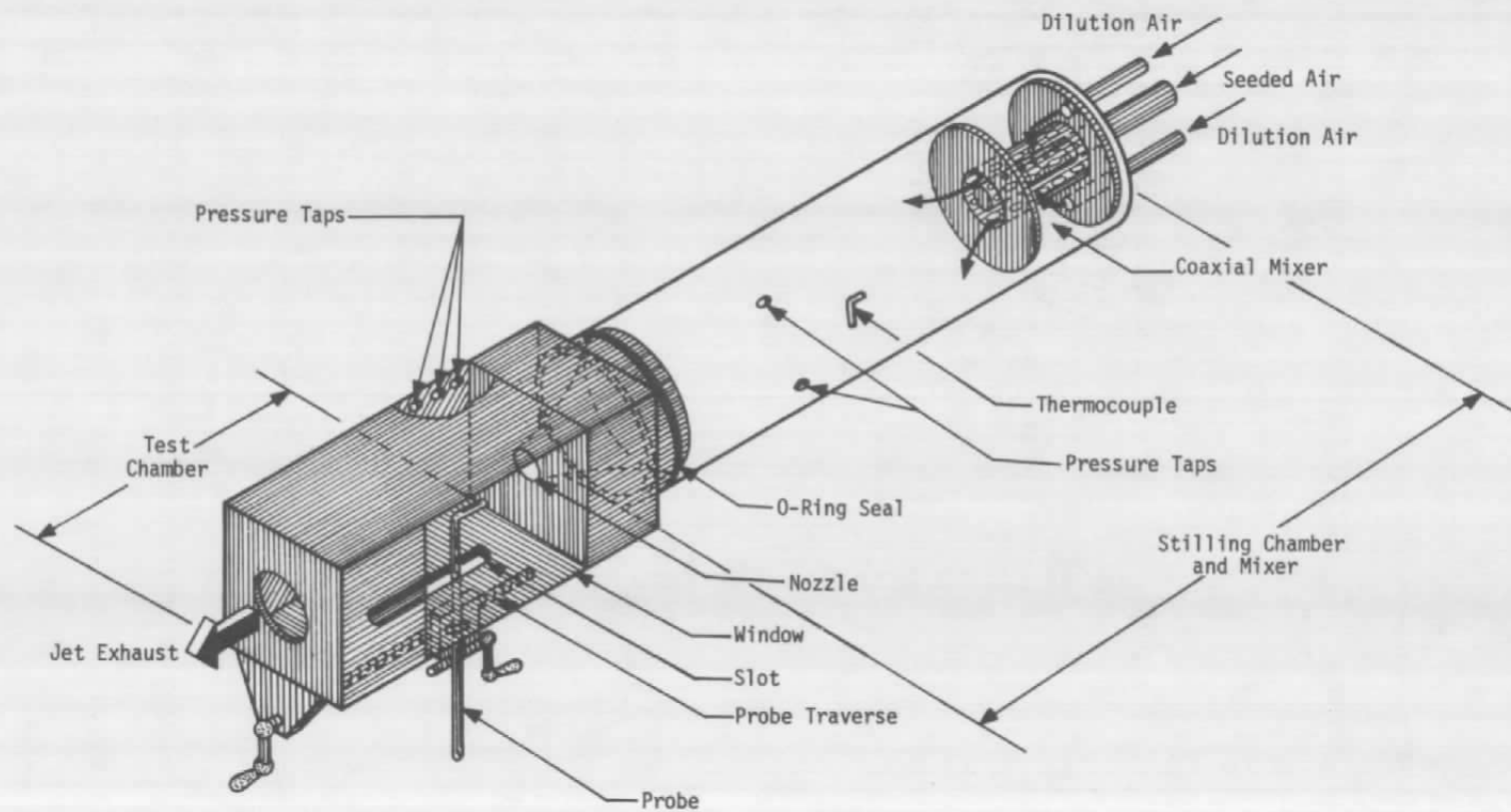


Figure 5. Test apparatus.

The jet was enclosed in a recirculation test chamber that was 18 nozzle diameters long and 5 diameters square. The front wall of this chamber was a thin, optically flat window which allowed LV measurements at axial stations up to $X/D = 9$. The other chamber walls were painted a flat black to minimize light reflections that could interfere with LV signals. Static pressure ports along the back wall of the test chamber were at stations $X/D = 2, 4$, and 8 . A slot in the bottom of the chamber could be opened to insert pitot and hot-wire probes mounted on the two-component traverse mechanism below the chamber.

2.2.1 LV Instrumentation

The LV system and associated electronics used in this study have been described in detail in Refs. 1 and 2. The present description will, therefore, concentrate on those factors influencing overall LV accuracy.

To measure statistical bias experimentally, the precision uncertainty in the IRLV measurements must be less than the bias. The IRLV and traverse system shown in Fig. 6 provided this precision in the low-speed jet measurements. A 514.5-nm wavelength light beam from an argon-ion laser was diffracted into several beams by the water-filled Bragg cell. The Bragg cell beam splitter described in Refs. 1, 2, and 15 measured negative velocities which frequently occur in highly turbulent jet flows. One nearly equal intensity beam pair from the Bragg cell was passed through the collimating lens, the beam expander, and the redirecting optics before being focused to form the LV probe volume. Although this system could measure two velocity components (see Ref. 2), only one was measured to simplify and speed up data acquisition.

For a dual-scatter LV system, Refs. 1 and 6 give the precision uncertainty as

$$\Delta u_i = \alpha - \beta u_i + \gamma u_i^2 \quad (29)$$

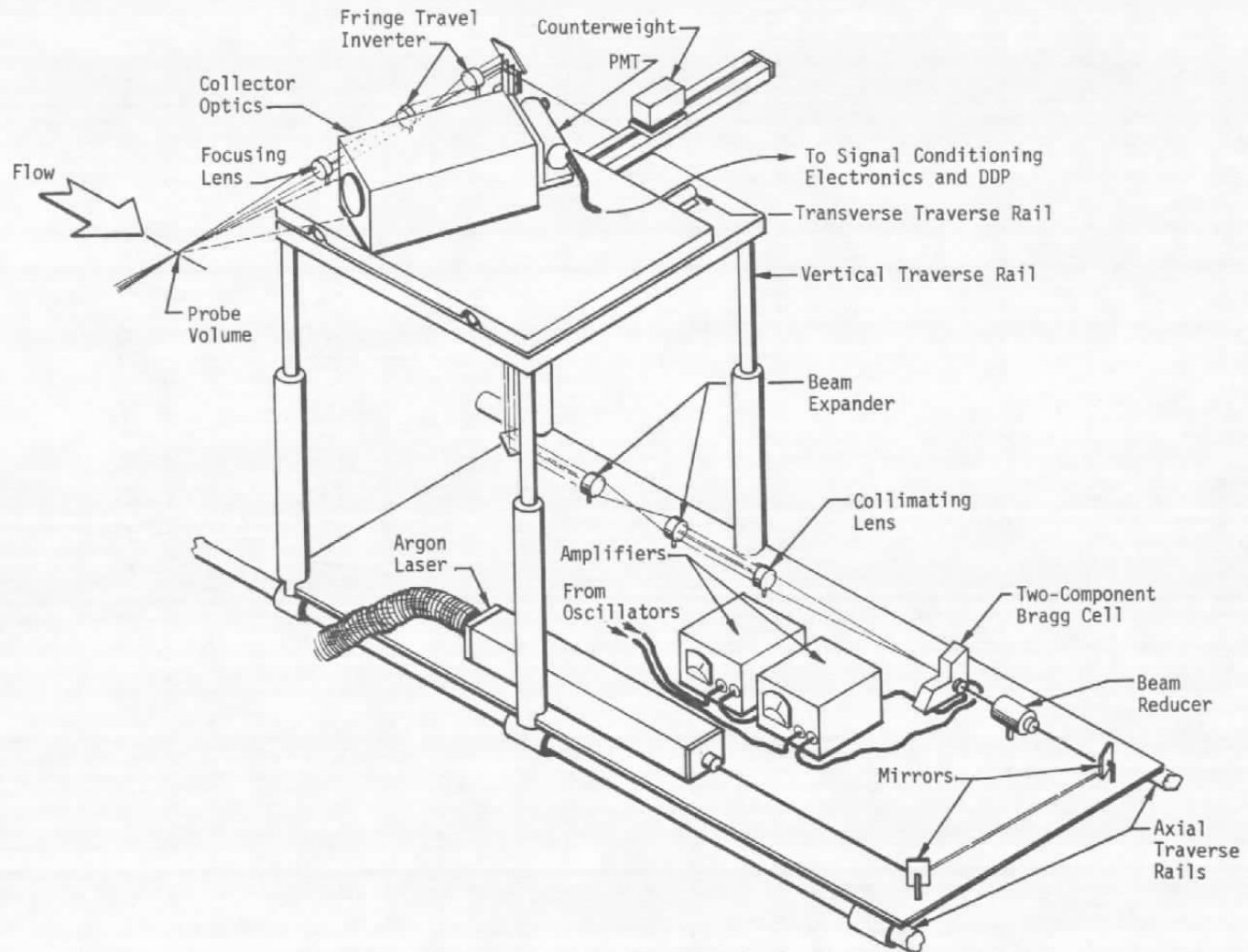


Figure 6. Laser velocimeter and traverse system.

where

$$\alpha = K_{\delta} f_o \left(\frac{\Delta f_o}{f_o} + f_o \Delta \tau_1 \right) \quad (30)$$

$$\beta = \frac{\Delta K_{\delta}}{K_{\delta}} - 2 f_o \Delta \tau_1 \quad (31)$$

$$\gamma = \frac{\Delta \tau_1}{K_{\delta}} \quad (32)$$

K_{δ} is the LV fringe spacing, f_o is the Bragg system reference frequency, and τ_1 is the measured LV burst period. The uncertainty in the LV fringe spacing, $\Delta K_{\delta}/K_{\delta}$, evaluated as described in Ref. 1 from LV calibrations, is ± 0.037 for the system K_{δ} of $18.5 \mu\text{m}$. The uncertainty in the 15-MHz reference frequency is estimated as $\Delta f_o/f_o = \pm 6.66 \times 10^{-4}$, and the uncertainty of the LV burst period, $\Delta \tau_1$, was determined in Ref. 2 to be ± 0.005 nsec for the particular LV burst counter processor used. Resulting precision uncertainties for velocities measured by this LV system are summarized in Table 1.

Table 1. Precision Uncertainty of Laser Velocimeter

Velocity, U		Precision, ΔU	
m/sec	ft/sec	m/sec	ft/sec
0	0	± 0.20	± 0.68
± 7.6	± 25	± 0.48	± 1.58
± 15.6	± 50	± 0.76	± 2.50
± 22.9	± 75	± 1.05	± 3.43
± 30.5	± 100	± 1.33	± 4.35
± 38.1	± 125	± 1.61	± 5.28

Because a finite number of measurements determines IRLV averages, the statistical confidence of these measurements must be considered. The 95-percent confidence interval for the arithmetic mean velocity is given in Ref. 1 as

$$\Delta < V > = \pm 1.282 \sqrt{\frac{\overline{(V - \hat{V})^2}}{M}} \quad (33)$$

The 95-percent confidence interval for the turbulence intensity is given in Ref. 41 as

$$\Delta \sigma_{<V>} = \pm 1.282 \sqrt{\frac{1}{M} \left[\frac{K-1}{4} + \frac{\overline{(V - \hat{V})^2}}{\hat{V}^2} \right]} \quad (34)$$

where K is the kurtosis coefficient, defined as

$$K = \frac{1}{T} \int_{-\frac{T}{2}}^{\frac{T}{2}} \frac{\overline{(V - \hat{V})^4}}{(V \sigma_{\hat{V}})^4} dt \quad (35)$$

To establish a better than 1.5-percent confidence interval for the mean velocity, all averages were calculated from at least 1,500 samples. For this sample size, a better than 3-percent confidence interval resulted for the turbulence intensities.

The uncertainty in positioning the IRLV probe volume will also contribute to uncertainty in the IRLV measurements. With the traverse system shown in Fig. 6 the probe volume could be moved along any of three mutually orthogonal axes and positioned to within ± 0.08 cm (± 0.03 in.) by properly accounting for hysteresis. However there is an additional uncertainty in locating the LV measurements due to the finite size of the probe volume. The diameter of the probe volume is taken as the diffraction limit of the focusing lens. For the 0.381-m focal length lens and 1.5 mm beam diameters at the lens a probe volume diameter of 0.17 mm results. The apparent probe volume length was reduced to approximately 0.33 cm by viewing the probe volume through a one-mm-diameter pinhole at 20 deg off-axis in backscatter.

The LV signal processing and recording systems achieved the accuracy required to measure the anticipated statistical bias, while attaining near-maximum IRLV data rates (and minimum $\langle \Delta t \rangle$) for this experiment. Signals from the photomultiplier (PMT) were processed without amplification to eliminate processing the weak, noisy signals from the edges of the probe volume. Also the PMT signals were processed only when the pedestal of the burst was detected by the high-frequency rejection A-gate oscilloscope trigger. Then the fringe-crossing period of each triggered signal was determined by a Model 8 Doppler data processor (DDP) only if the signal passed the processor noise rejection criteria. These criteria required that the fringe-crossing periods based on 4, 5, and 8 cycles agree to within 1.5 percent, and only signals between 8 and 20 MHz (-76 to -122 m/sec) were processed to reduce the possibility of recording noise.

Additional details of the model 8 DDP are given in Refs. 15 and 31. The processor used was modified by interval-counting circuitry triggered by the DDP print command to measure the time, Δt_i , between successive validated signals. The interval-counting resolution was ± 0.5 μ sec. With this modification, approximate time-integrated average velocity moments and the data rates in addition to the arithmetic average moments were determined.

To attain near-maximum IRLV data rates the data were recorded using direct memory access to a minicomputer. This system could typically record over 13,000 fringe periods and time intervals per second. At this rate and a 15-m/sec mean velocity there was a high probability that the LV signals would result from multiple particle traversals of the probe volume, but might not be processed by the DDP. By controlling the seeder pressure, the flow was never seeded heavily enough to exceed mean data rates of 4,000 per second; this lessened the possibility of excluding measurements because of multiple particle traversals.

2.2.2 Supporting Instrumentation

Statistical biasing will not occur in averages of velocities measured by continuously monitoring the jet flow. Such continuous measurements were made using both pressure and hot-wire instrumentation and statistical bias was identified by comparing the average LV measurements with the average pressure and hot-wire measurements. However, such identification is possible only if the uncertainty in the pressure and hot-wire measurements is less than the bias. Furthermore, the pressure and temperature stilling-chamber measurements used to monitor the jet flow must be equally accurate for a meaningful comparison of the independent measurements.

To attain the necessary accuracy in continuous pressure measurements Barocel[®] pressure transducers were used. These transducers maintained an accuracy of ± 0.15 percent of the measured pressure throughout their ± 10 -mm-Hg pressure range, as determined by calibration against a laboratory standard Hook gage which was traceable to the National Bureau of Standards (NBS). The ambient pressure, P_a , was measured with a Bourdon-tube pressure gage, and the air temperature, T , was monitored using a shielded, self-aspirated, copper-constantan thermocouple. Both instruments were calibrated against NBS laboratory standards. The measurements were continuously monitored by the minicomputer data system which continuously displayed the value of each variable as well as the velocity calculated from

$$U^2 = 2g_c J_c c_p T \left[1 - \left(\frac{P_a + P_c}{P_a + \Delta P} \right)^{\frac{\gamma-1}{\gamma}} \right] \quad (36)$$

where g_c and J_c are unit conversion factors, c_p is the fluid specific heat, T is the jet fluid temperature, P_a is the ambient pressure, P_c is the test cell gage pressure, ΔP is the stilling chamber or pitot probe to test cell differential pressure, and γ is the ratio of specific heats. The precision of these velocity measurements was determined by expanding Eq. (36) in a Taylor series in all of the measured variables and evaluating

the expression at the maximum uncertainty of each (see Ref. 42). The analysis yielded an uncertainty in velocity of less than 1.5 percent at the nominal jet exit velocity of 30.5 m/sec.

The hot-wire measurements were made using a Thermo-Systems, Inc. 1050 series, constant-temperature anemometer equipped with a 3.8- μ m-diam, tungsten sensor. The ends of the 1.5-mm-long sensor were plated to reduce end effects, leaving an active sensor length of 1.25 mm. Assuming the sensor would properly respond only to eddies of this size or larger, the frequency response of the sensor was estimated to be 24 kHz when eddies were convected past the sensor at the nominal jet exit velocity. Therefore, signal frequency components greater than 30 kHz were considered noise and filtered out. The hot-wire bridge output was recorded on FM-modulated analog tape maintaining a 30-kHz frequency response.

To attain the needed accuracy in the hot-wire measurements, the recorded bridge output was digitized at a 50-kHz rate and each sample was converted to a velocity using the hot-wire response equation (Refs. 43 and 44),

$$e_1^2 = A + BU_1^h - CU_1 \quad (37)$$

The constants A, B, C, and h were determined by a nonlinear least-squares fit of Eq. (37) to the hot-wire calibration (Ref. 45). Calibrations were performed every 30 minutes in the test apparatus using velocities measured with the pressure instrumentation. The calibration data exhibited excellent agreement during all but one test, and those test data were not used for the comparisons shown. Figure 7 shows two typical calibrations. Because Eq. (37) fit the calibration data so well (Fig. 7) the uncertainties in the hot-wire velocity measurements were only slightly larger than the uncertainties in the pressure-determined calibration velocities. Furthermore, by using approximately 200,000 digital hot-wire samples when averaging the hot-wire data, the 95-percent

statistical confidence intervals were better than 0.1 percent of the mean velocities and approximately 0.2 percent of the turbulence intensities and should not add significantly to the hot-wire measurement uncertainty. The hot-wire and pitot probe position uncertainties were ± 0.5 mm.

2.3 RESULTS

The experimental examination of statistical bias was conducted in three phases. First, the jet flow was evaluated to determine how well the flow conditions that theoretically result in bias were met. Second, the flow was mapped with pitot and hot-wire probes. And, third, the flow was mapped with the IRLV. The second and third phase results were then compared to determine the magnitude of any bias present.

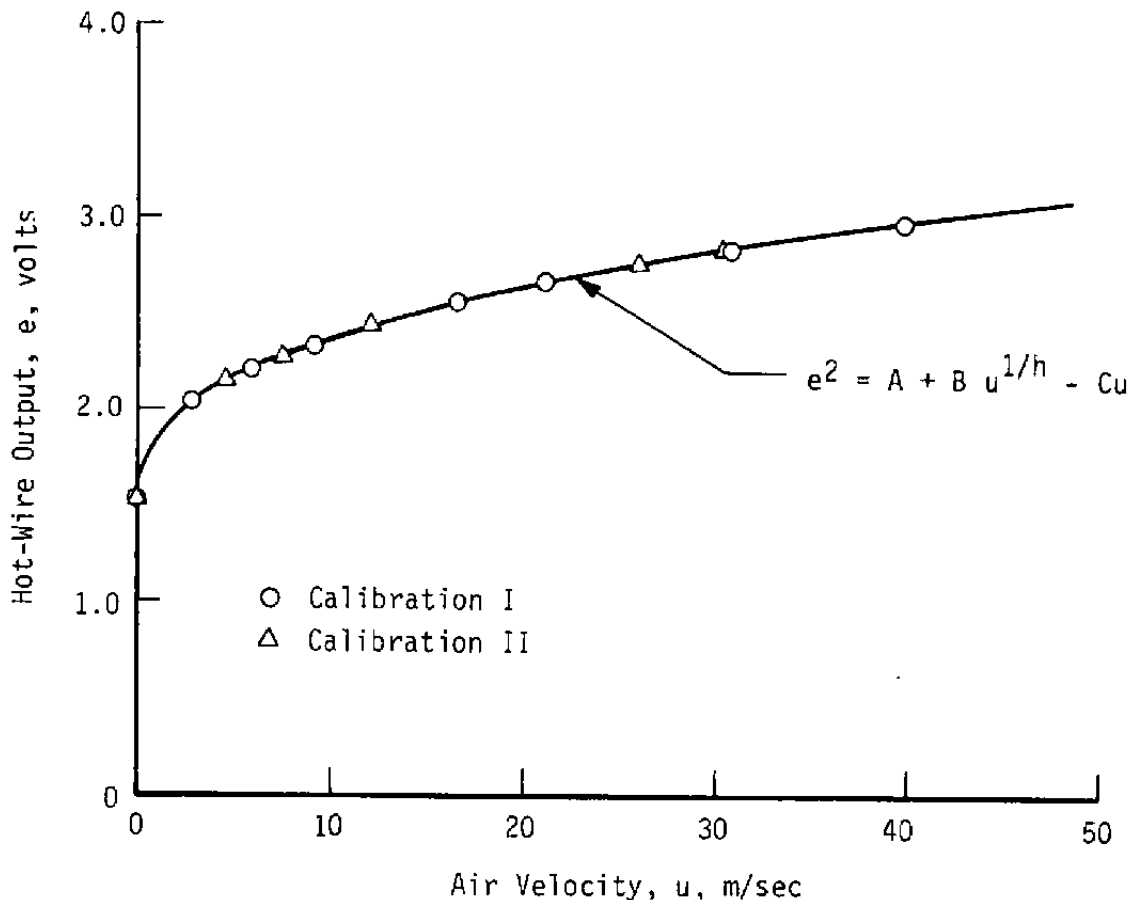
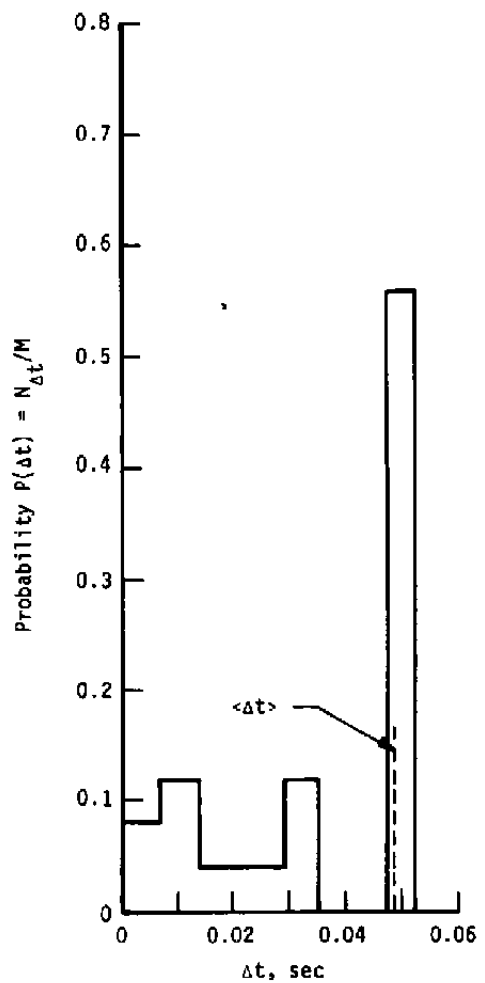


Figure 7. Hot-wire anemometer calibration.

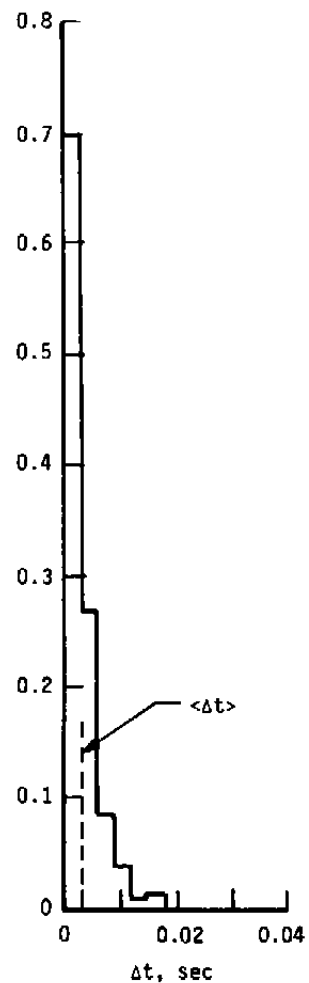
In the first phase the operation of the seeder was examined to determine whether it provided a steady, regular, controllable output. Successive LV detections of particles in the jet core were recorded, and the time between each detection, Δt_1 , was measured by the LV data processor. Histograms of these Δt_1 data, presented in Fig. 8 for several seeder settings, show that nearly equal times separate most particle detections; the standard deviation of the times between detections is less than 0.5 percent of the average time between detections for all cases. In the smooth core flow these nearly equal times indicate nearly equal fluid mass separating each particle, and thus a fairly uniform particle concentration. Note that no particles were detected with the seeder turned off, verifying that only particles from the seeder comprise the LV data sets obtained in the tests.

The distribution of the seed concentration in the test chamber was also examined by timing successive LV detections and evaluating the average time between detections, $\langle \Delta t \rangle$. If the ratio $\langle \Delta t \rangle / \langle \Delta t(r) \rangle$ is distributed as $\bar{U}(r) / \bar{U}_L$ throughout the jet, then it can be concluded from Eq. (9) that the particle concentration is, on the average, uniform throughout the jet. Figure 9 shows that radial distributions of $\langle \Delta t \rangle / \langle \Delta t(r) \rangle$ do correspond to pitot probe measurements of $\bar{u}(r) / \bar{u}_L$, illustrating that the particle concentration is essentially uniform, on the average, throughout the jet.

To examine the size of particles in the test flow, particle samples were collected near the test chamber exit. Photomicrographs taken of these samples using a scanning electron microscope show that some coagulation of the 1- μ m seed occurred. The distribution of particle sizes determined from several photomicrographs is shown in Fig. 10 and indicates that most particles had 1- to 3- μ m diameters. A few larger particles were visible in the photomicrographs, but they were chain-shaped coagulations that most likely were created during the particle collection. Particle dynamic calculations indicated that 3- μ m particles did not appreciably lag the flow, so the departure from the desired 1- μ m size had little effect on the results.



a. Average rate, 25.8 samples/sec



b. Average rate, 343.9 samples/sec

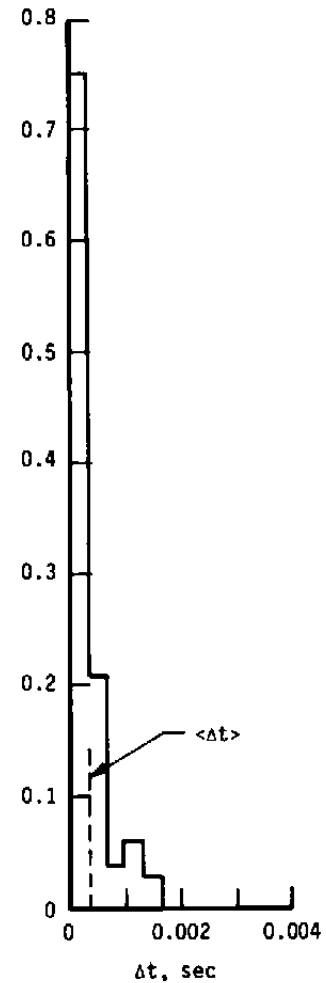
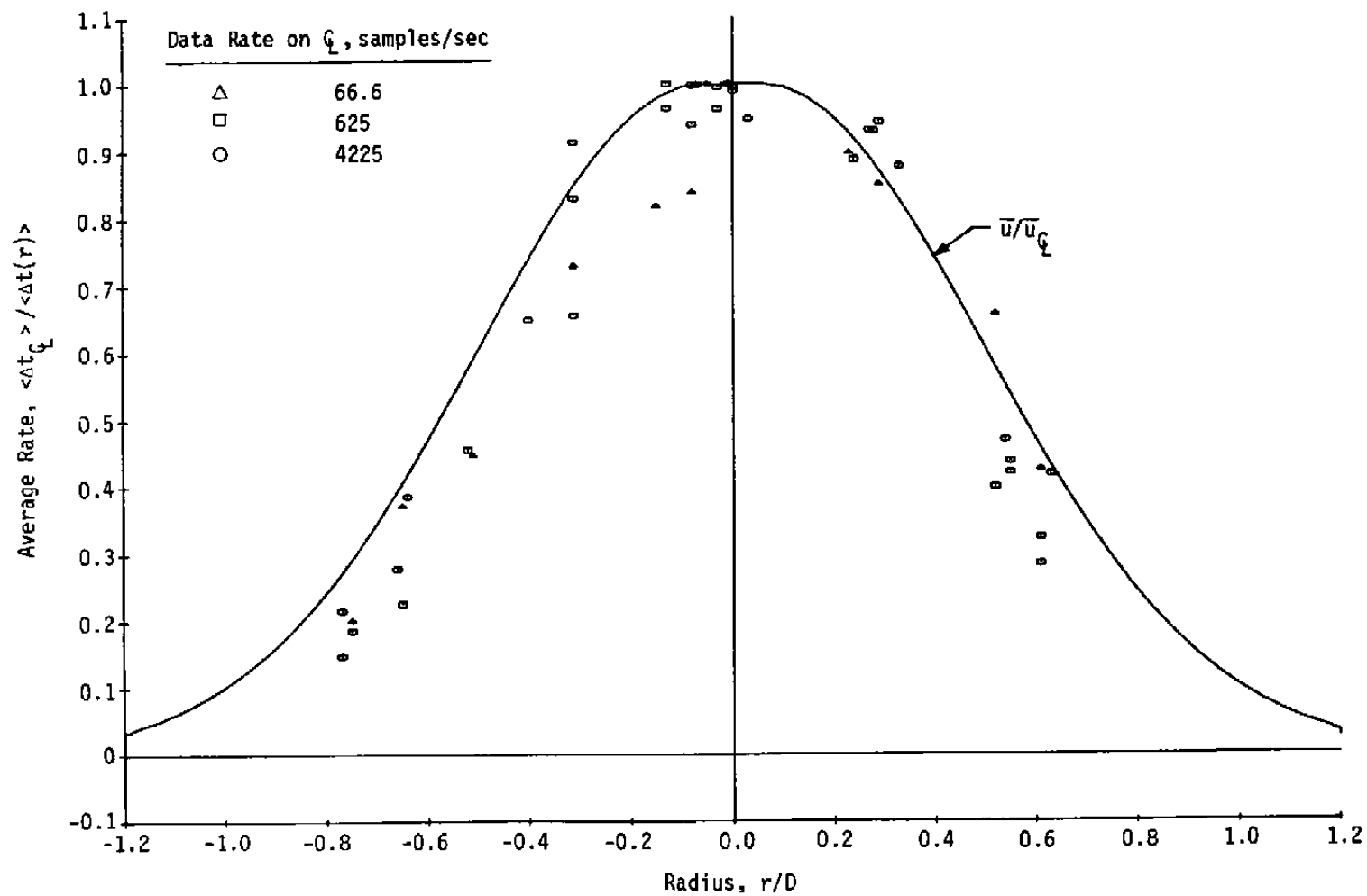
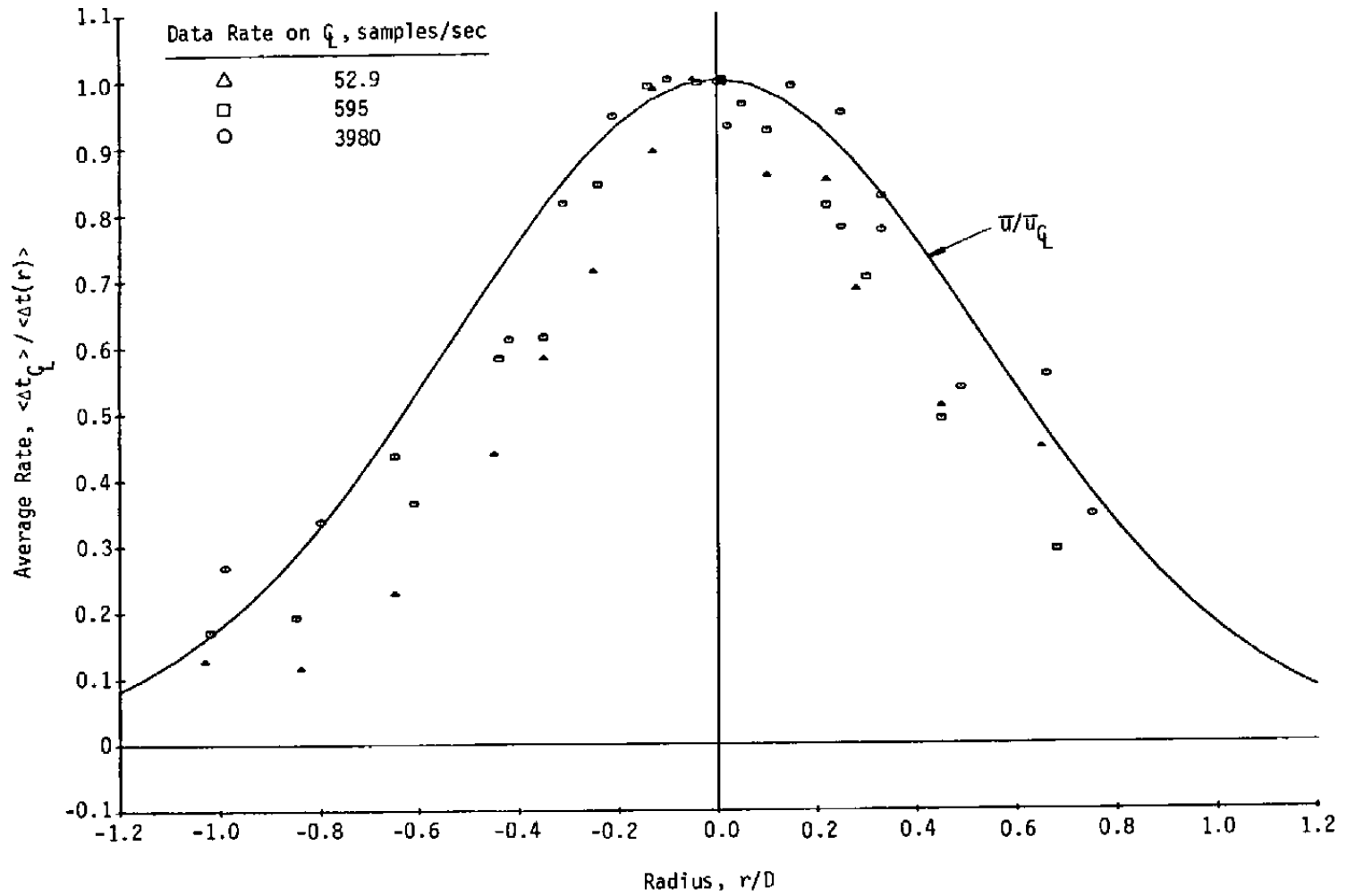
c. Average rate, 3235.8 samples/sec
(note scale change)

Figure 8. Histograms of particle interarrival times.



a. Variation of data rate at $X/D = 4$
 Figure 9. Data rate variation in jet near field.



b. Variation of data rate at $X/D = 6$
Figure 9. Concluded.

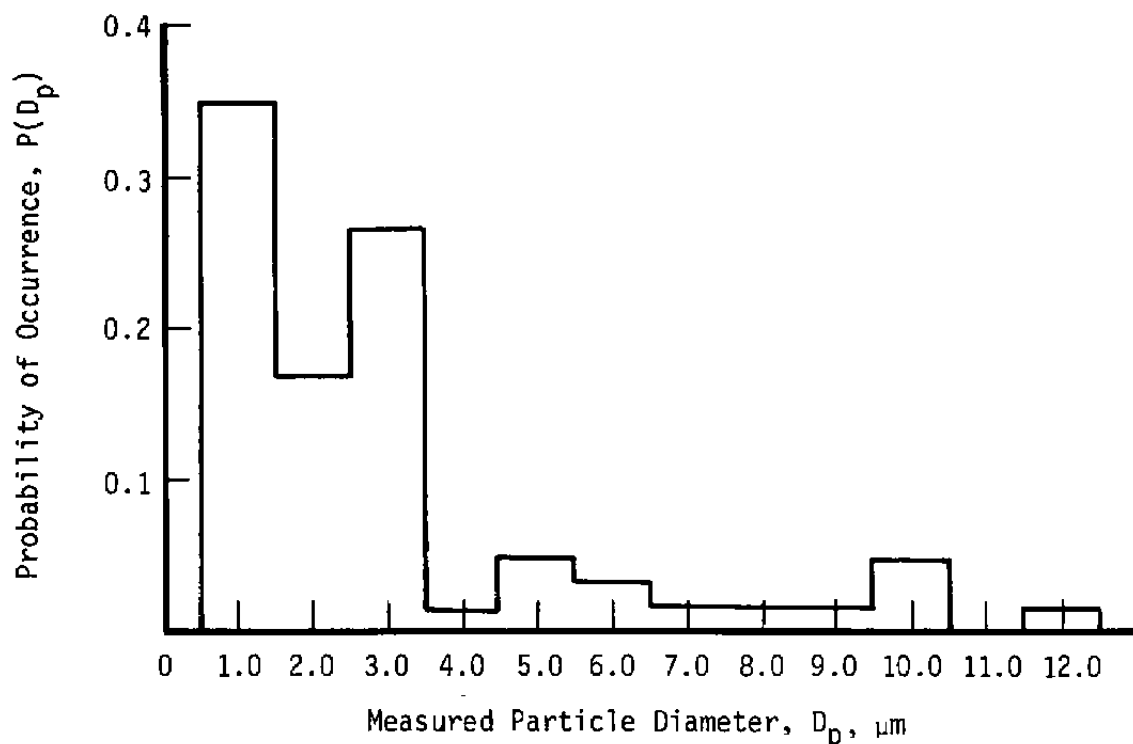


Figure 10. Particle size distribution.

Once the seeding characteristics were determined, the flow field was mapped by conventional instrumentation. Radial surveys were made at axial stations of 2, 4, 6, and 8 nozzle diameters with both pitot and hot-wire probes. A hot-wire radial survey at $X/D = 1/16$ measured the jet core turbulence, which was less than 2 percent of the nominal exit velocity. Figure 11 shows the results of the surveys of the mean axial velocity where the mean velocities were fit with the semi-empirical expression

$$\frac{\bar{U}(X, r)}{\bar{U}_C(X)} = \exp \left[-0.693 \left(\frac{r - r_o(X)}{b(X)} \right)^2 \right] \quad (38)$$

as an aid for comparison to the LV results. The centerline velocity, $\bar{U}_C(X)$, inner radius of the jet shear layer, $r_o(X)$, and the shear layer width to the half-velocity point, $b(X)$, were determined using the curve-fitting method of Ref. 45 and are given in Table 2. Even though only hot-

wire data points are indicated in Fig. 11, both hot-wire and pitot measurements were used in deriving the curve fits.

Although measurements were made across the entire jet, only data from the jet region, where the local turbulence intensity was less than 0.33, will be used for bias identification. Data aliasing attributable to negative velocities and hot-wire response variations can be significant in pitot and hot-wire measurements at higher intensities (Ref. 37 and 46). Note that hot-wire measurements were only made in unseeded flows. The hot-wire calibration tended to drift more in seeded flows, and particle-wire impingements can cause pseudo-velocity signals that alter the hot-wire accuracy. However, pitot measurements made in the seeded flow verify that the mean velocity characteristics of the jet at high particle concentrations were identical to those of the unseeded flow.

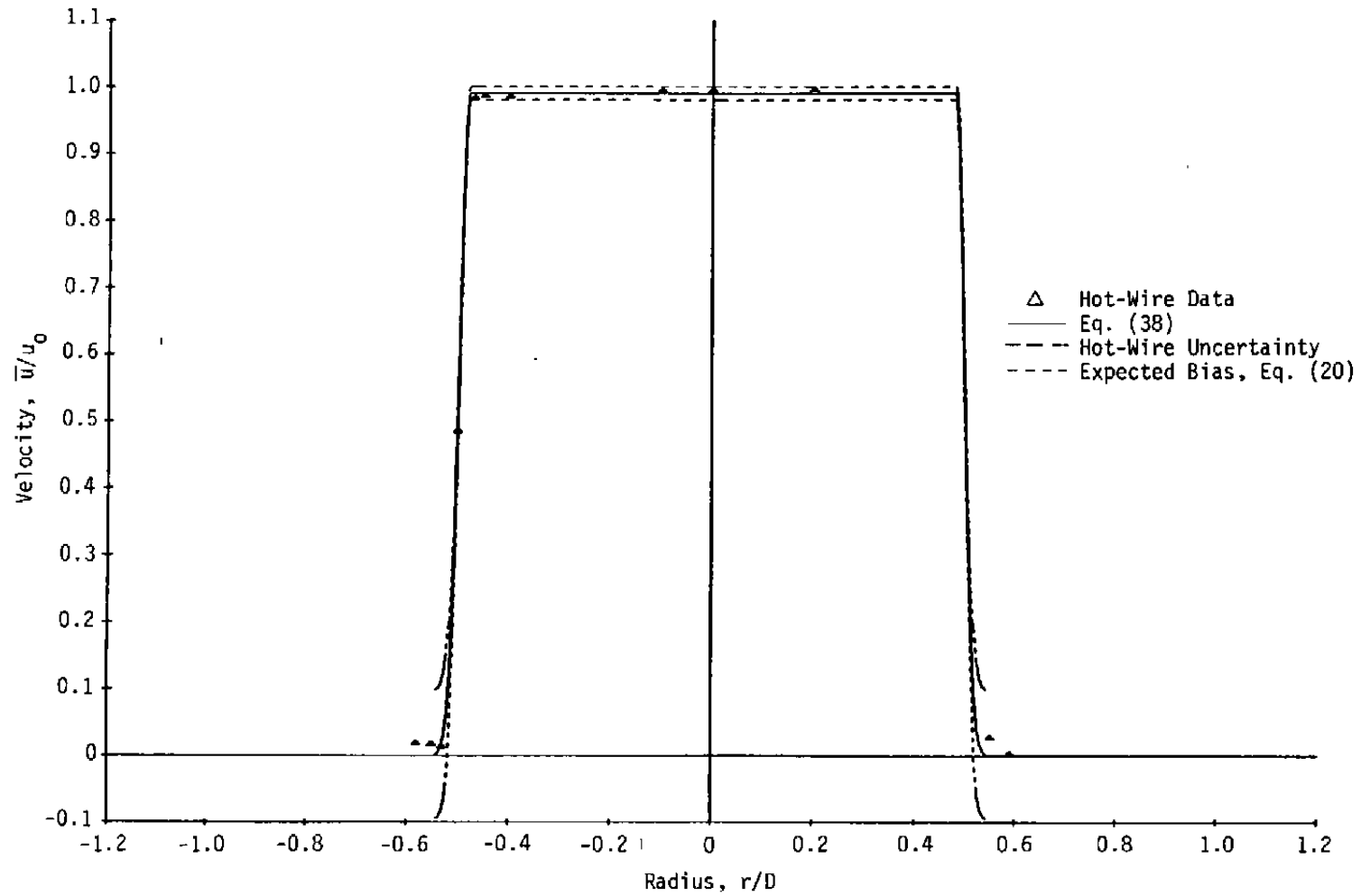
The turbulence intensities measured with the hot wire at axial stations of 2, 4, 6, and 8 nozzle diameters are shown in Fig. 12. The data inside the $\sigma_u = 0.33$ limits were least squares fitted to a second order polynomial:

$$= \begin{cases} A(x) + B(x)r_\sigma + C(x)r_\sigma^2, & \text{for } r \leq r_\sigma \\ A(x) + B(x)r + C(x)r^2, & \text{for } r > r_\sigma \end{cases} \quad (39)$$

The polynomial parameters $A(x)$, $B(x)$, $C(x)$, and r_σ are given in Table 2. The polynomial data fits, along with Eqs. (20) and (38), predicted the maximum mean velocity bias that could be anticipated in the IRLV measurements. The anticipated bias is shown in Fig. 11 along with the hot-wire uncertainty. In determining the hot-wire uncertainty, the hot-wire pressure calibration uncertainty, derived from Eq. (36), was doubled to account for any other hot-wire measurement uncertainties. Even with the broad uncertainty assumption it is obvious from Fig. 11 that the IRLV statistical bias should be identifiable in these tests.

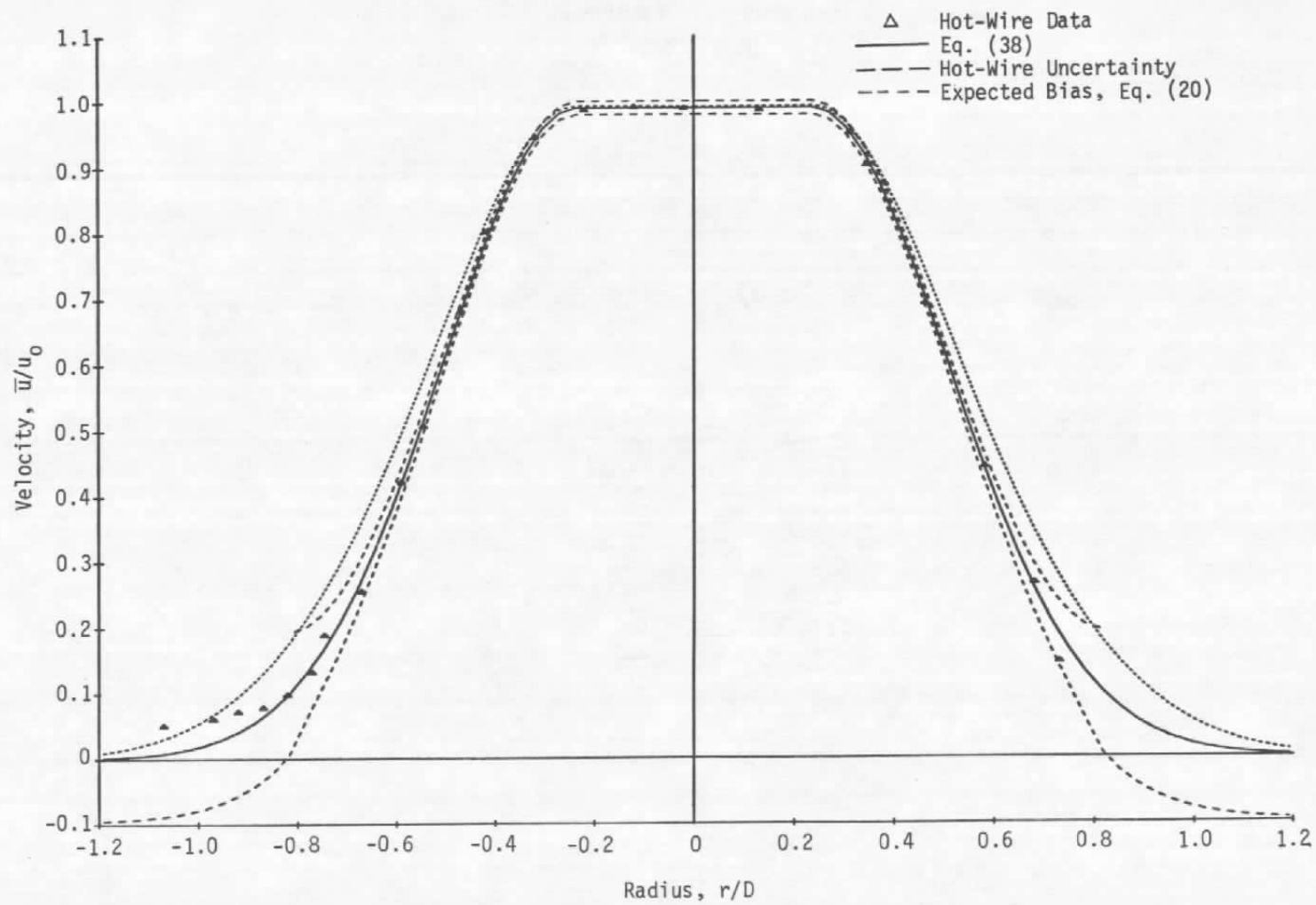
Table 2. Jet Flow-Field Data

X/D	Mean Velocity Fit Eq. (38)			Turbulence Intensity Fit Eq. (39)			
	$\bar{U}_{CL}(x)$	$r_o(x)$	$b(x)$	$A(x)$	$B(x)$	$C(x)$	r_σ
0.06	99.14	0.479	0.021				
2.0	98.97	0.235	0.319	0.0558	-0.3976	1.7308	1.1831
4.0	96.07	0	0.563	0.0896	0.1644	0.6238	0
6.0	83.57	0	0.632	0.1606	0.2072	0.2865	0
8.0	66.98	0	0.737	0.2332	0.1418	0.2385	0

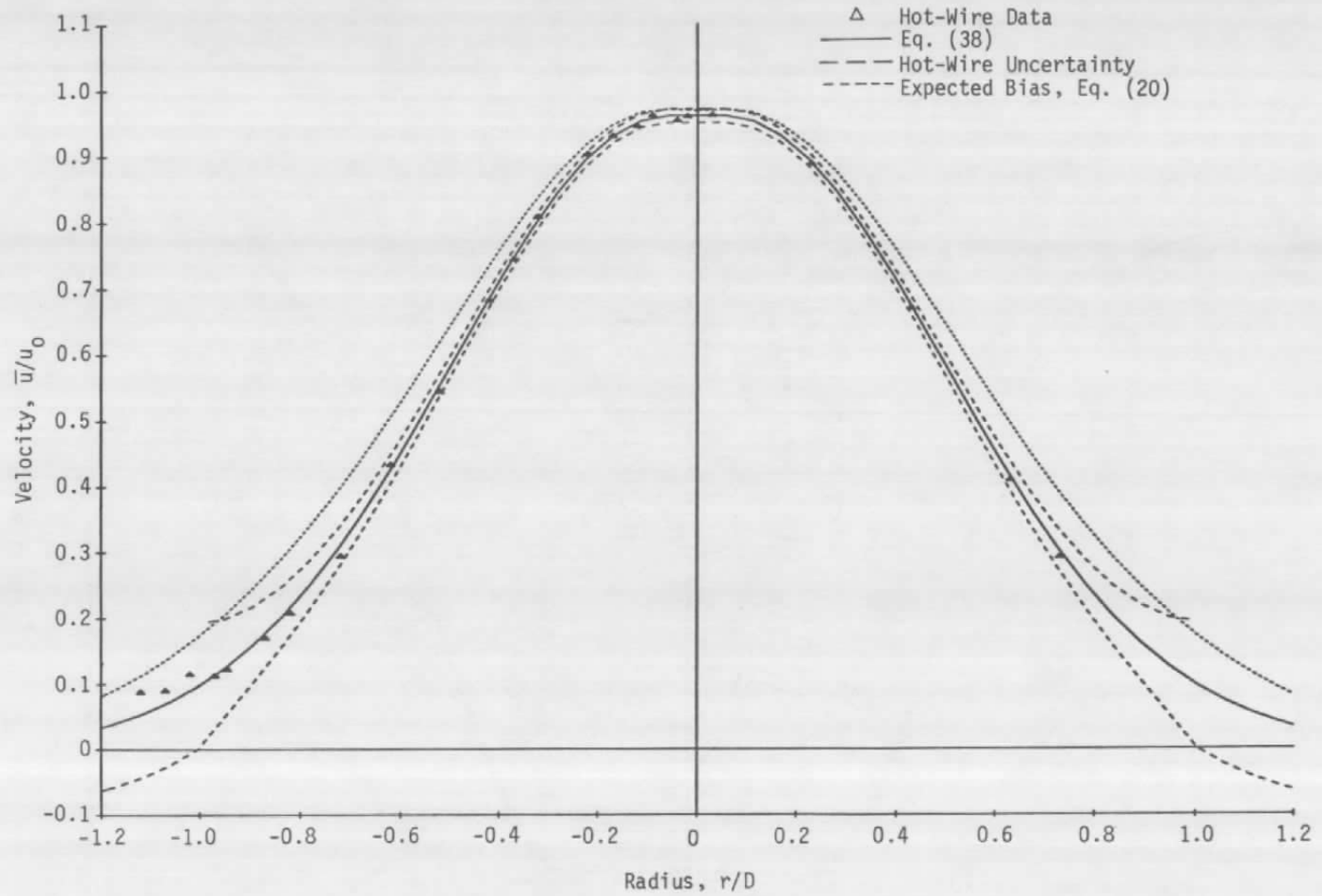


a. $X/D = 1/16$

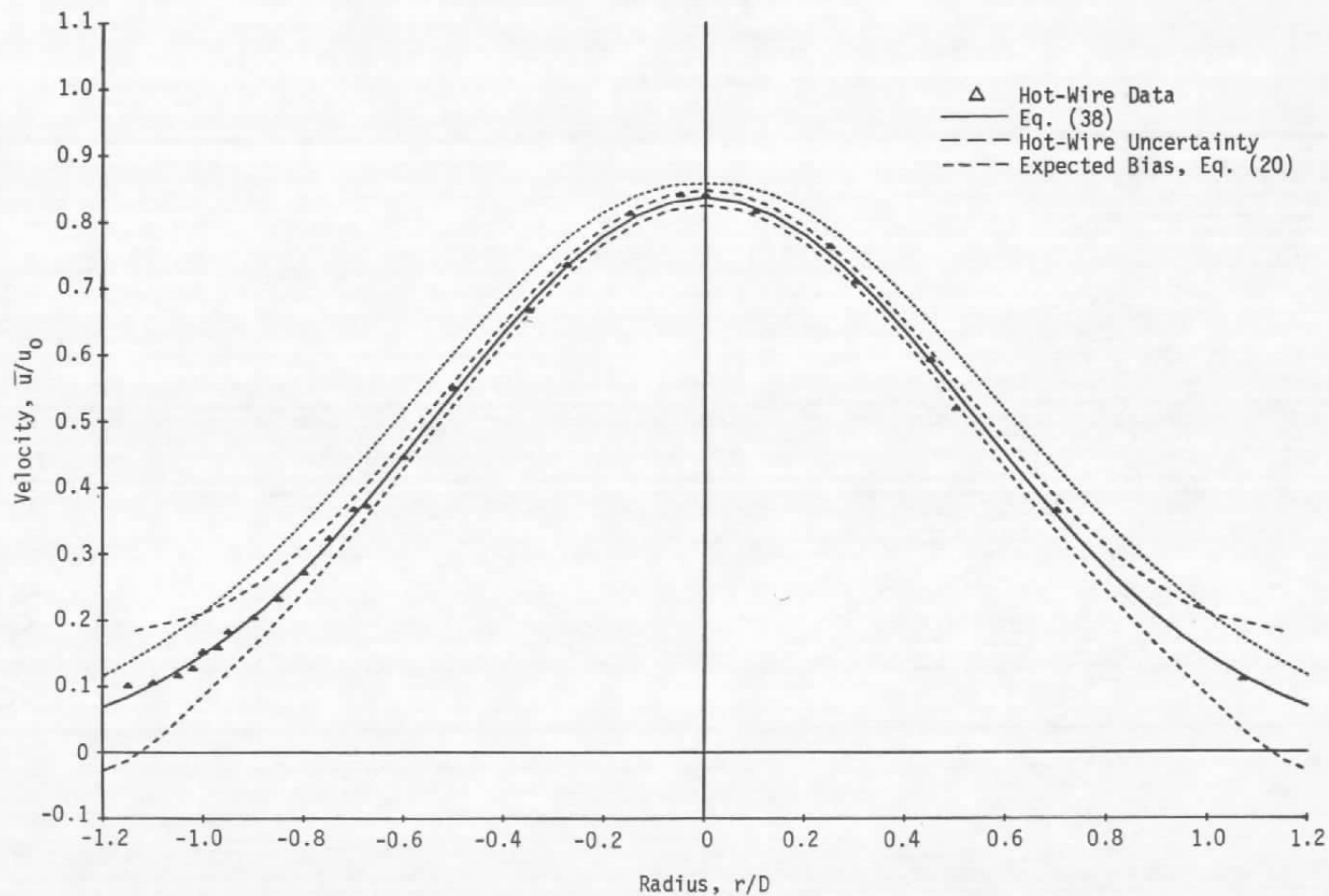
Figure 11. Hot-wire measurements of axial velocity distributions.



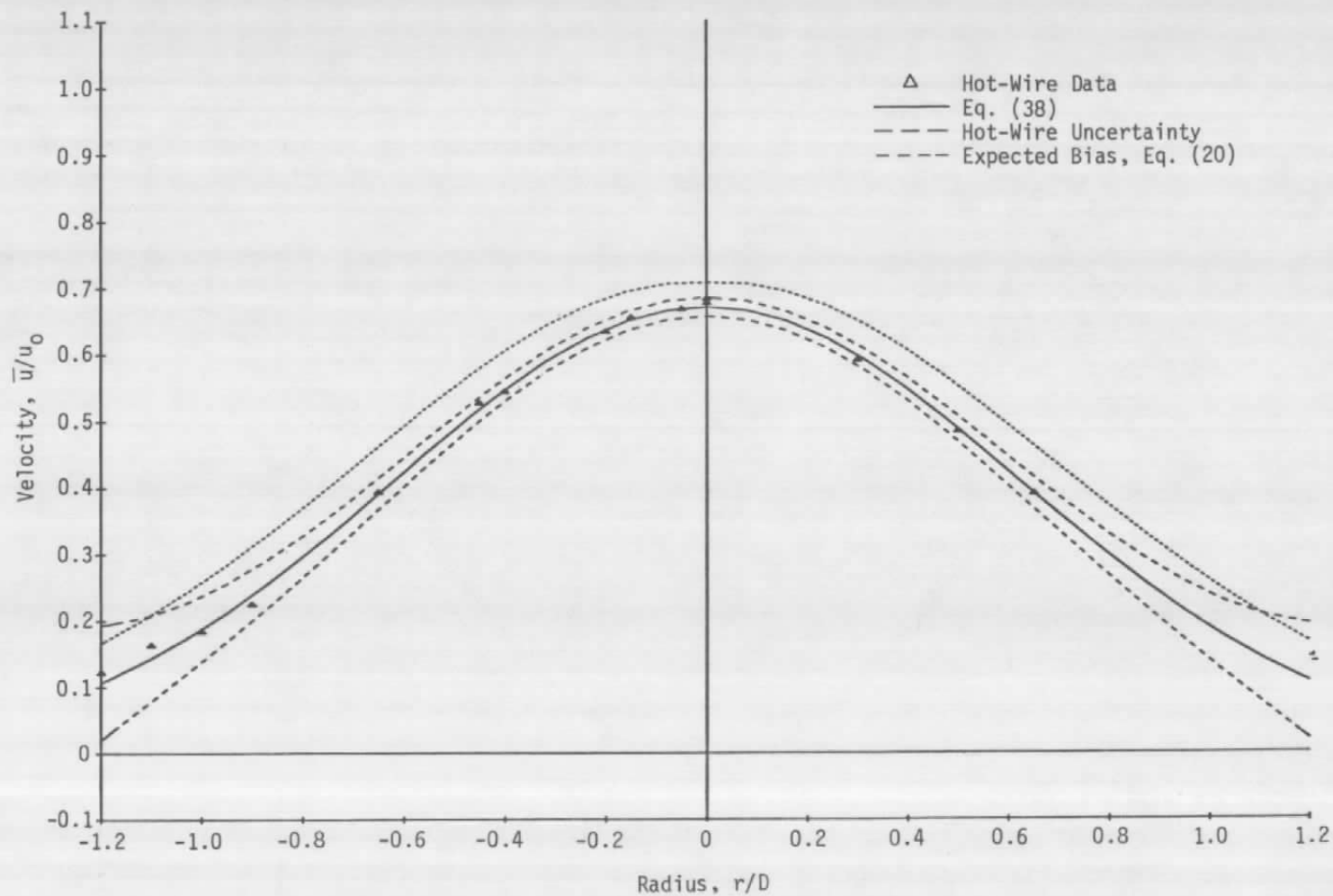
b. $X/D = 2$
 Figure 11. Continued.



c. $X/D = 4$
 Figure 11. Continued.



d. $X/D = 6$
Figure 11. Continued.



e. $X/D = 8$
Figure 11. Concluded.

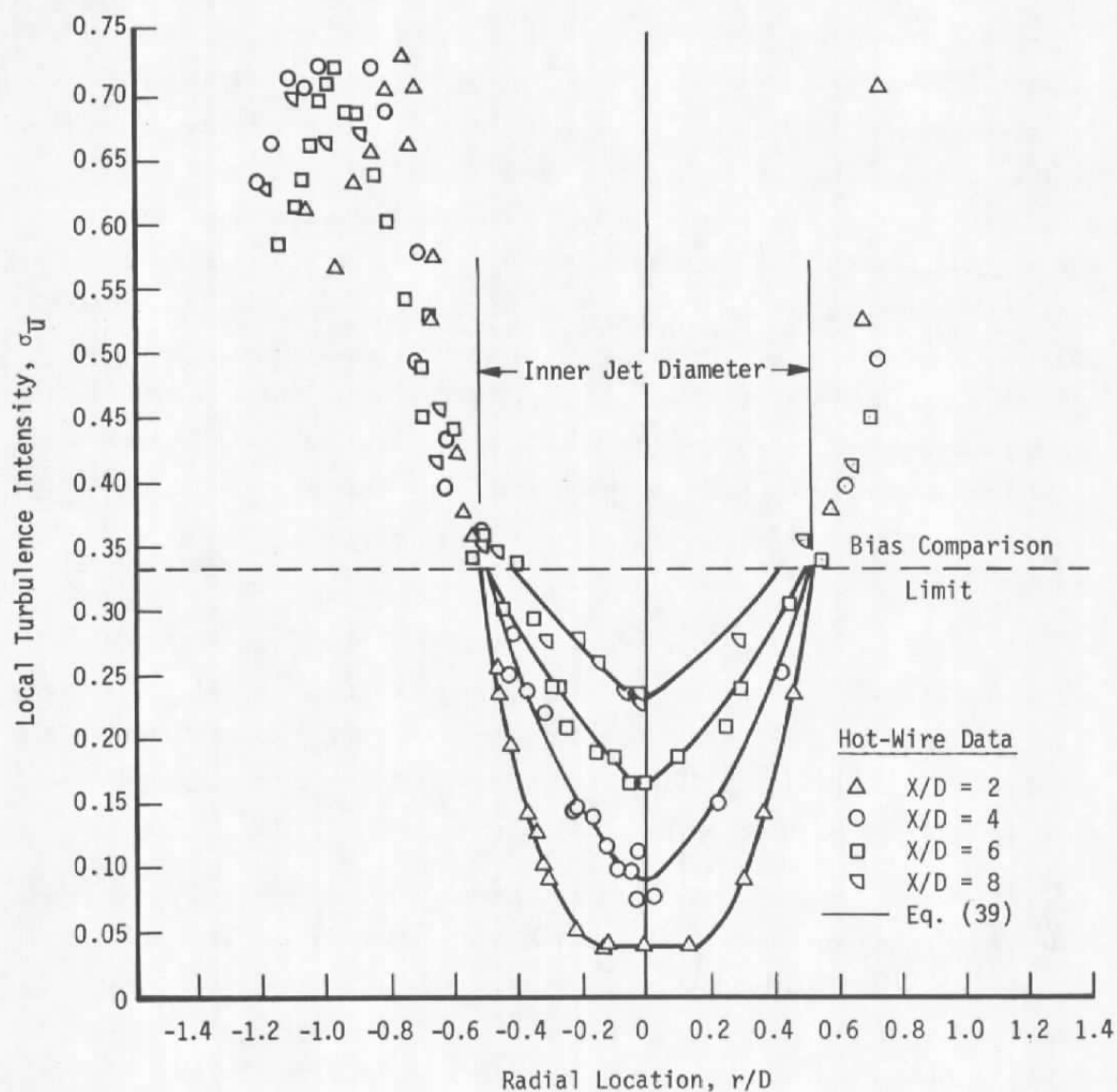


Figure 12. Hot-wire measurements of local turbulence intensities.

In the theoretical discussion of statistical bias, requiring $\hat{V}_i = V_i$ was equivalent to assuming that an IRLV would detect several particles per integral time scale; bias might be reduced if detection rates are not this high. To examine this assumption, integral time scales were determined from the digital hot-wire data using a fast Fourier transform technique (Ref. 47). To reduce computer storage requirements, hot-wire measurements acquired over a 15-second interval were segmented into small digital data records of about 0.17 second duration and transformed record by record. The resulting power spectra were averaged and transformed to determine the autocorrelations from which the integral time scales were determined by numerical integration. Integral time scales obtained in this manner are compared to values interpolated from the data of Sami (Ref. 38) in Fig. 13. Data rates of 1,500 to 5,000 samples per sec were necessary to ensure one particle per integral length scale at axial stations between $X/D = 4$ and 8 where the bias was to be identified. Thus, to test for bias-data-rate dependence, data were recorded at rates ranging from 10 to 4,800 samples/sec.

In addition, the hot-wire data were used to determine the radial variation of the skew and the kurtosis shown in Figs. 14 and 15, respectively. These higher order central moments were used for predicting the statistical bias in IRLV averages of the turbulence intensity and skew coefficient as indicated by Eq. (22).

After the "unbiased" flow-field characteristics were established, IRLV radial surveys were made at axial stations of 2, 4, 6, and 8 nozzle diameters. Identification of statistical bias primarily involved examination of the $X/D = 4$ and 6 data. At $X/D = 2$ the shear layer had enough curvature to produce mean velocity gradients in the LV probe volume, making those measurements questionable. At $X/D = 8$ the mean velocity was low, and the pitot and hot-wire accuracies were not sufficient for bias identification throughout the flow.

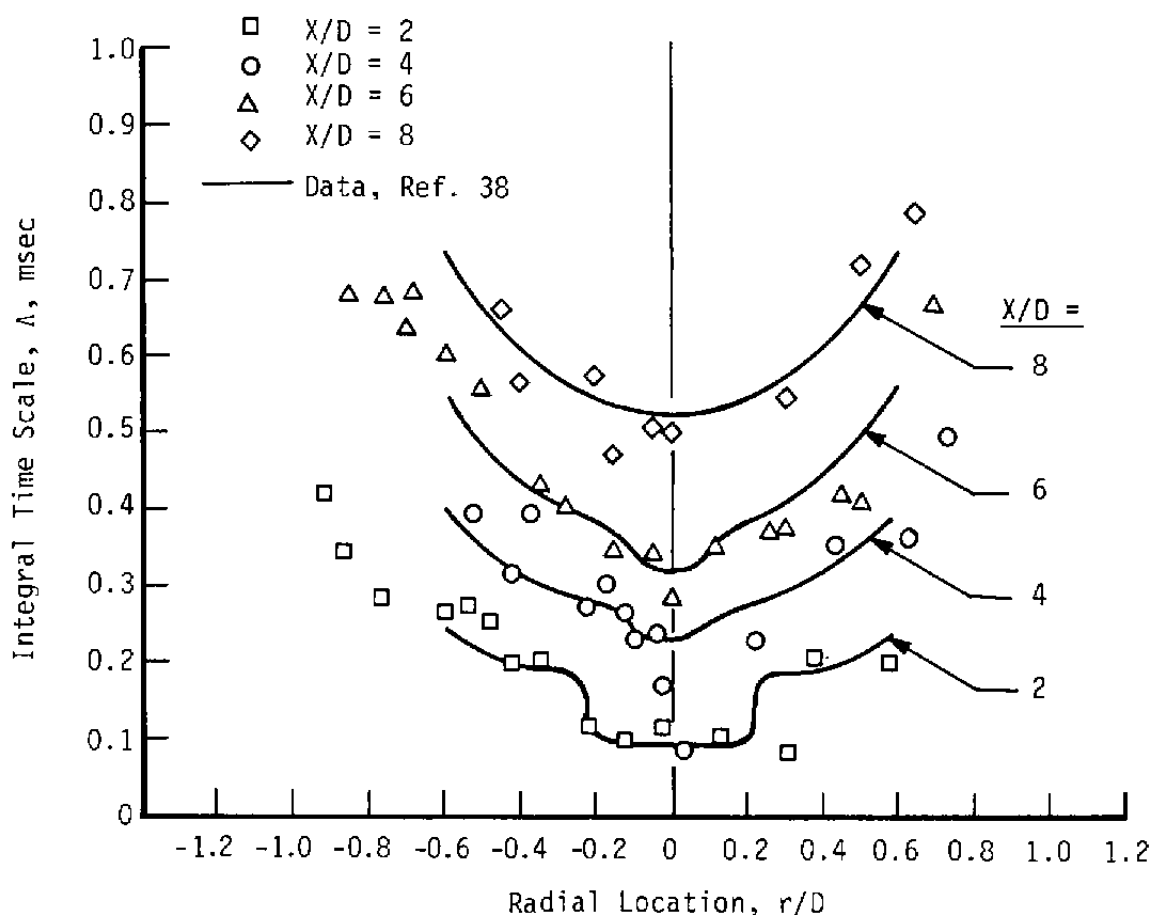


Figure 13. Radial variation of integral time scales.

The IRLV radial surveys were repeated at several seeder settings to define any bias variation with seed density. These mean velocity surveys are compared in Fig. 16 with the "unbiased" velocity curves. Note that the IRLV data more closely approximate the unbiased velocity curves than the theoretical bias curves, regardless of the seeding rate. The IRLV measurements of turbulence intensity (Fig. 17) also agree well with the unbiased velocity curves, indicating that statistical biasing was not nearly as significant as predicted for these tests. No significant bias dependence on data rate was discerned.

To date the only AEDC tests that show differences in IRLV and hot-wire measurements that might be attributable to bias were reported

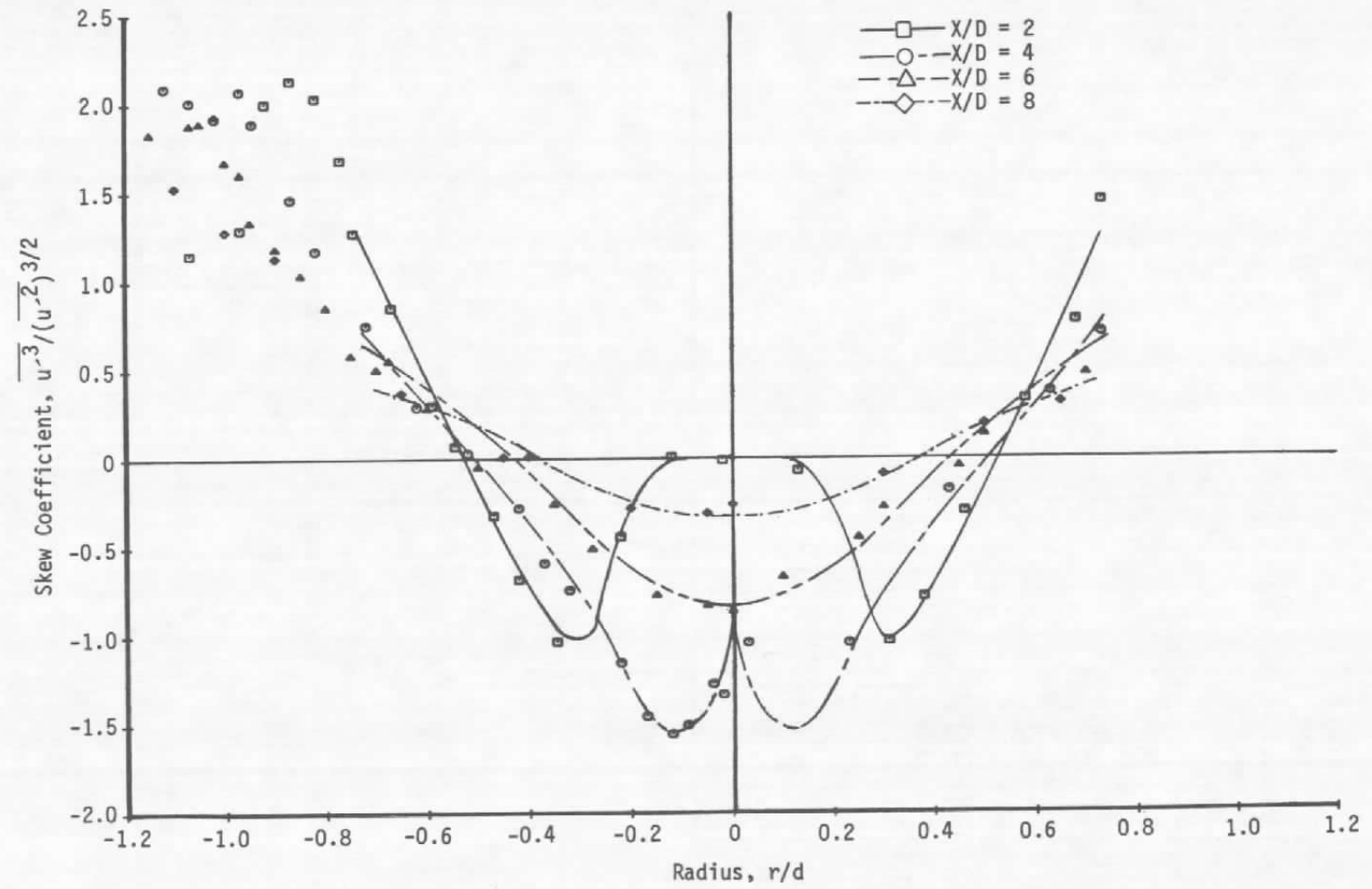


Figure 14. Radial distribution of skew coefficient.

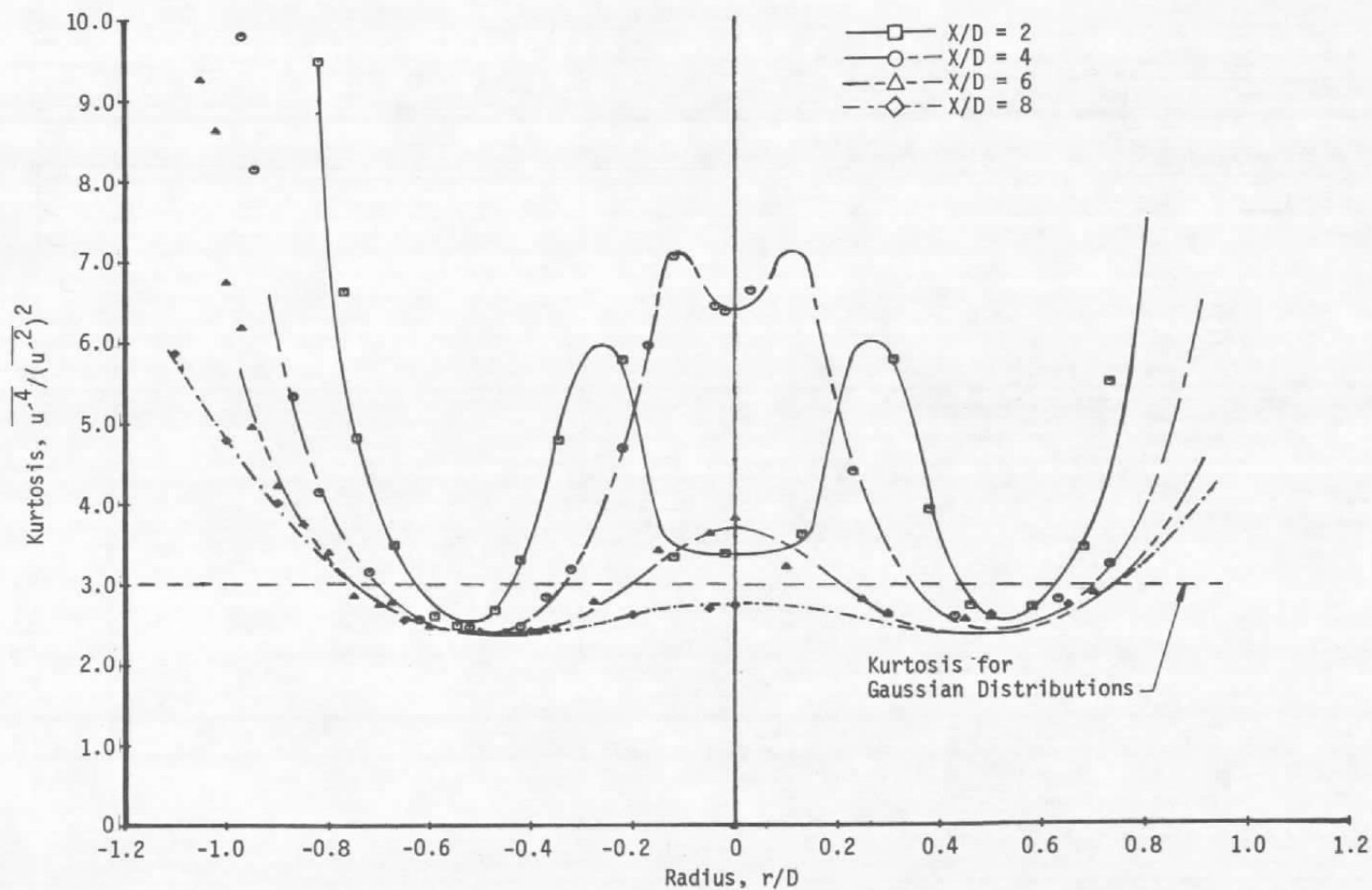
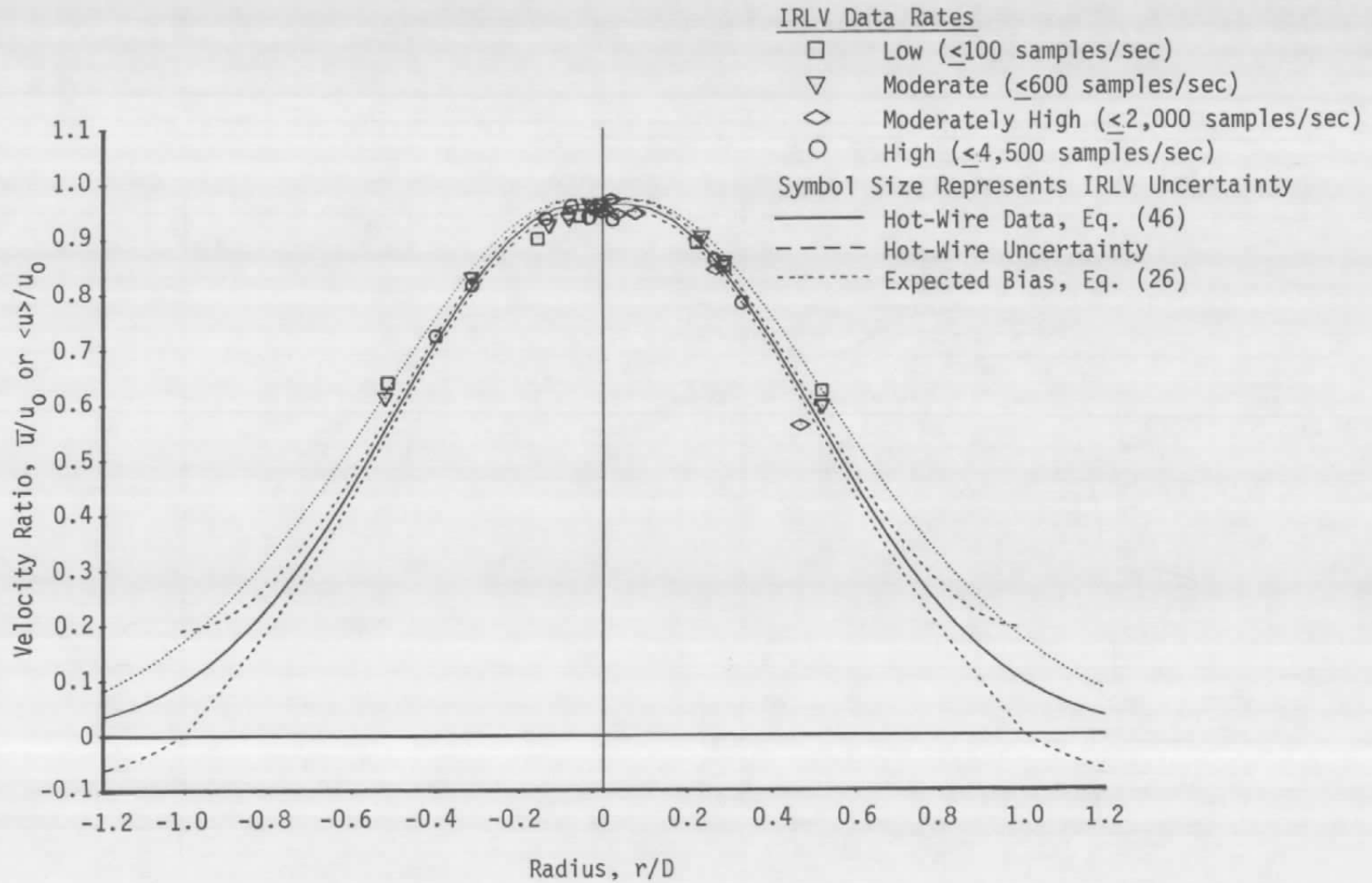
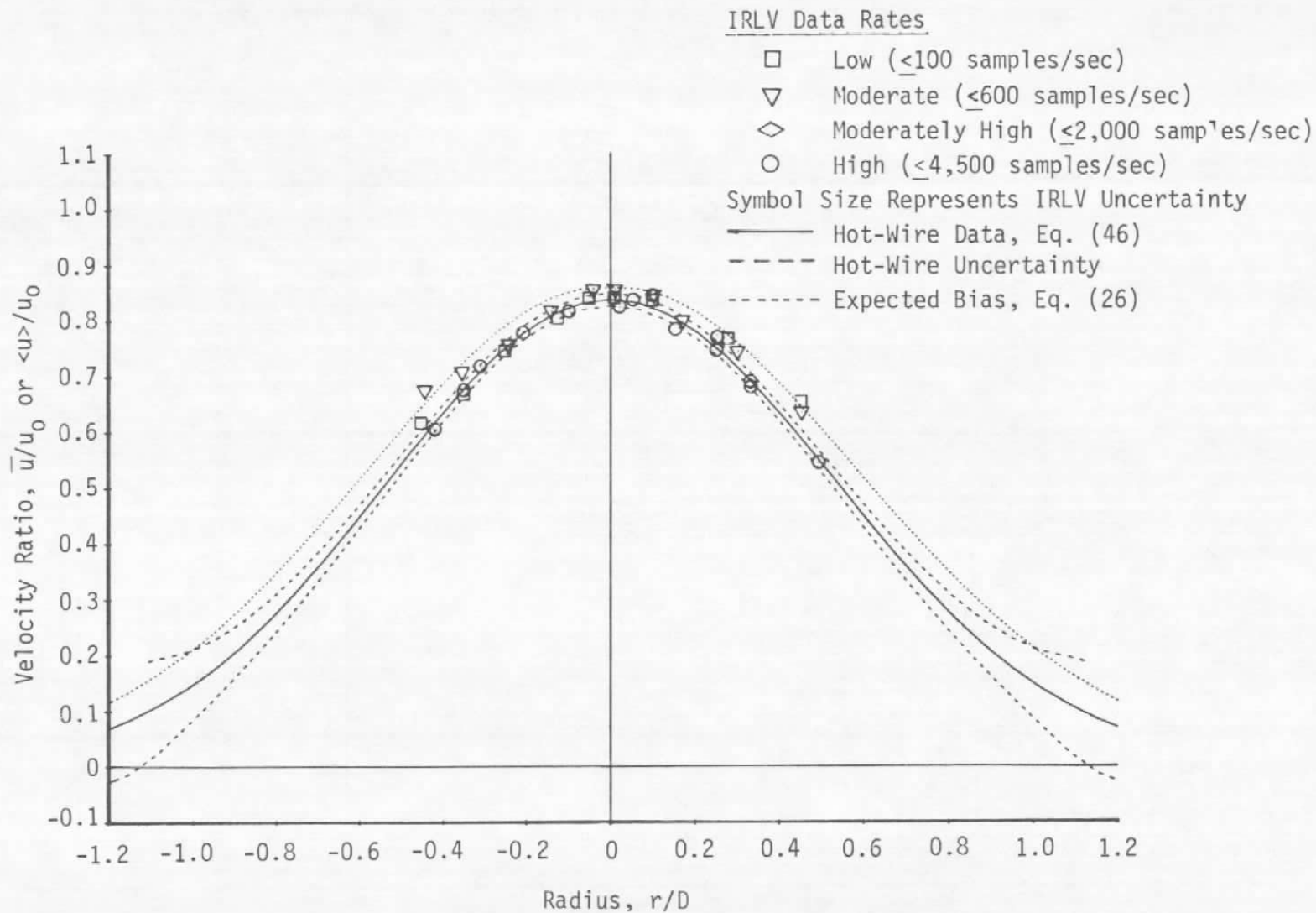


Figure 15. Radial distribution of axial kurtosis coefficient.



a. $X/D = 4$

Figure 16. Comparison of IRLV mean velocity with "biased" predictions.



b. $X/D = 6$
Figure 16. Concluded.

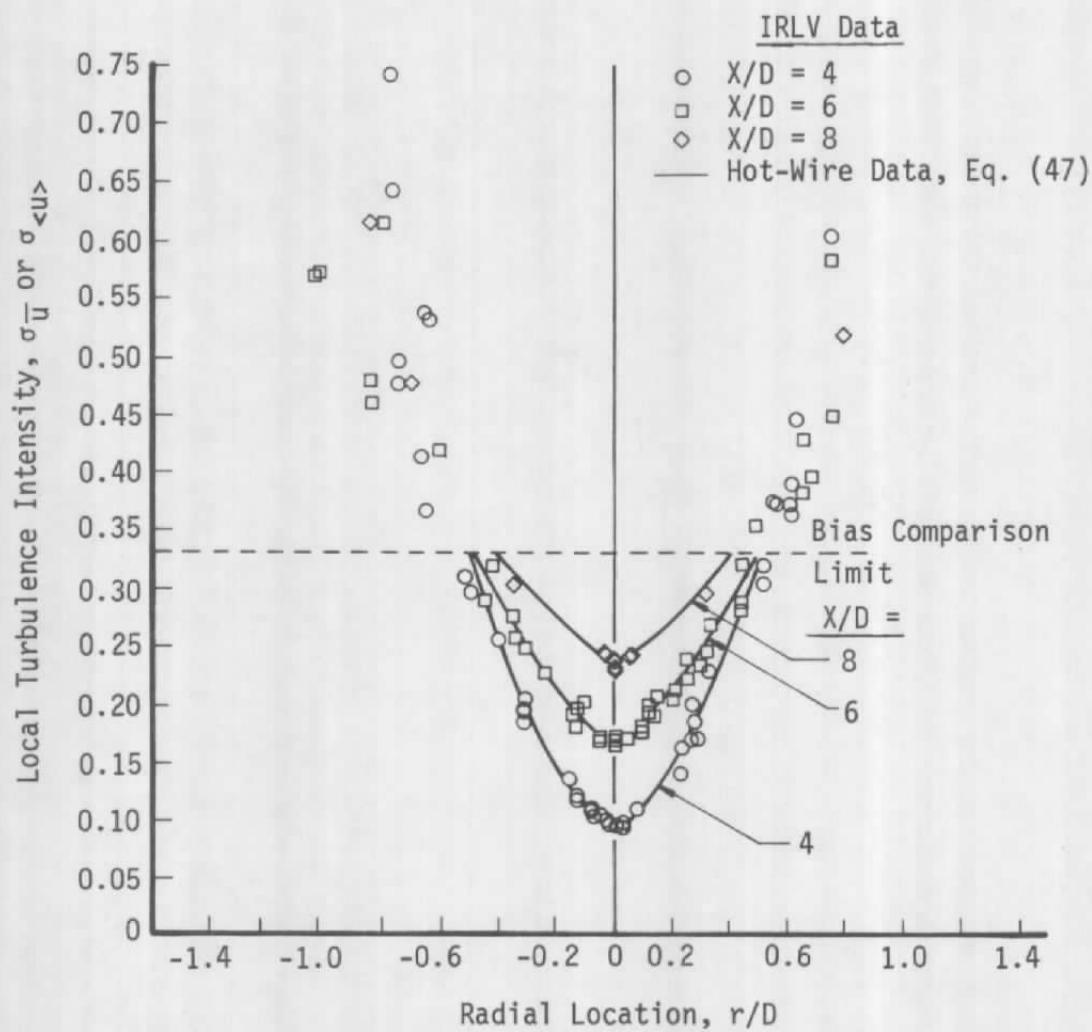


Figure 17. Comparison of IRLV and hot-wire local turbulence intensities.

in Ref. 11. In that experiment, the difference in the two measurements was most obvious in the centerline axial velocity decay. Accordingly, the centerline axial velocity decay and turbulence intensity distribution as determined by pitot, hot-wire, and IRLV data averages in the present experiment are plotted in Fig. 18. These data show no evidence of either statistical bias or a bias-data-rate dependence.

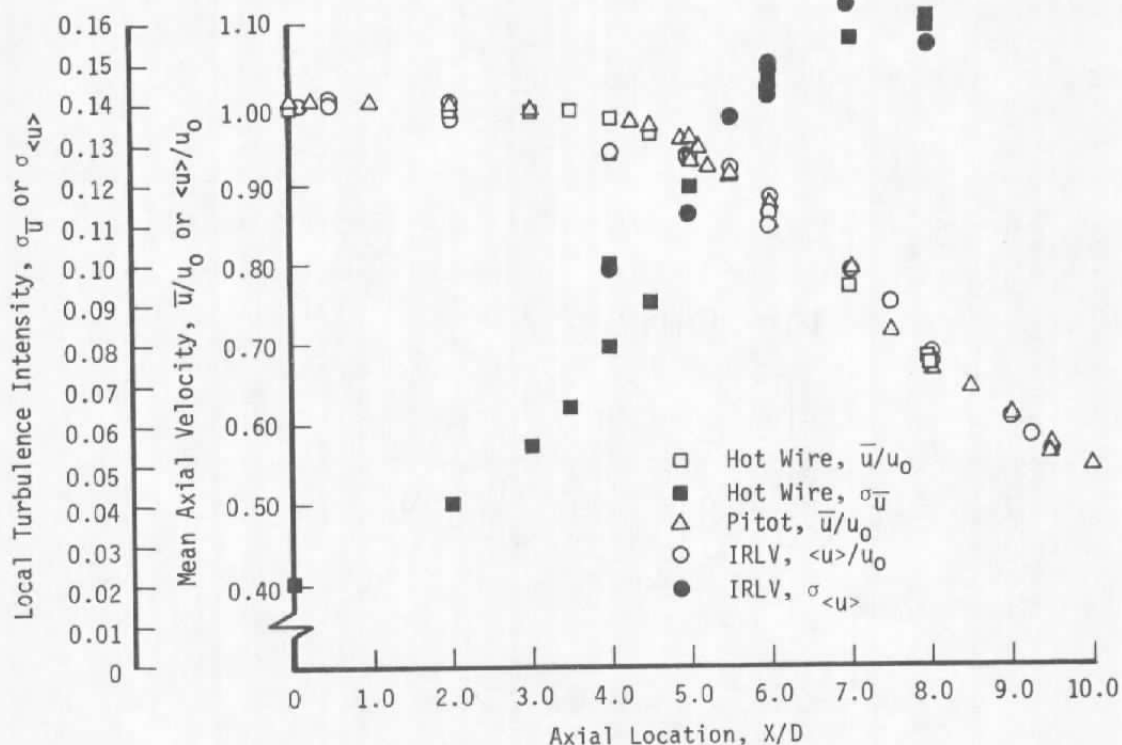


Figure 18. Centerline distribution of axial velocities and turbulence intensities.

In this study bias was identified by comparing averages of IRLV data with unbiased measurements. It is clear from Eq. (6) and stated in Ref. 20 that if the particle interarrival times are random no bias will result. Reference 25 suggests further that random selection of samples from an IRLV data set will lead to unbiased averages of the velocity moments. Therefore, in a final attempt to identify statistical bias, the IRLV averaged mean velocities and turbulence intensities were

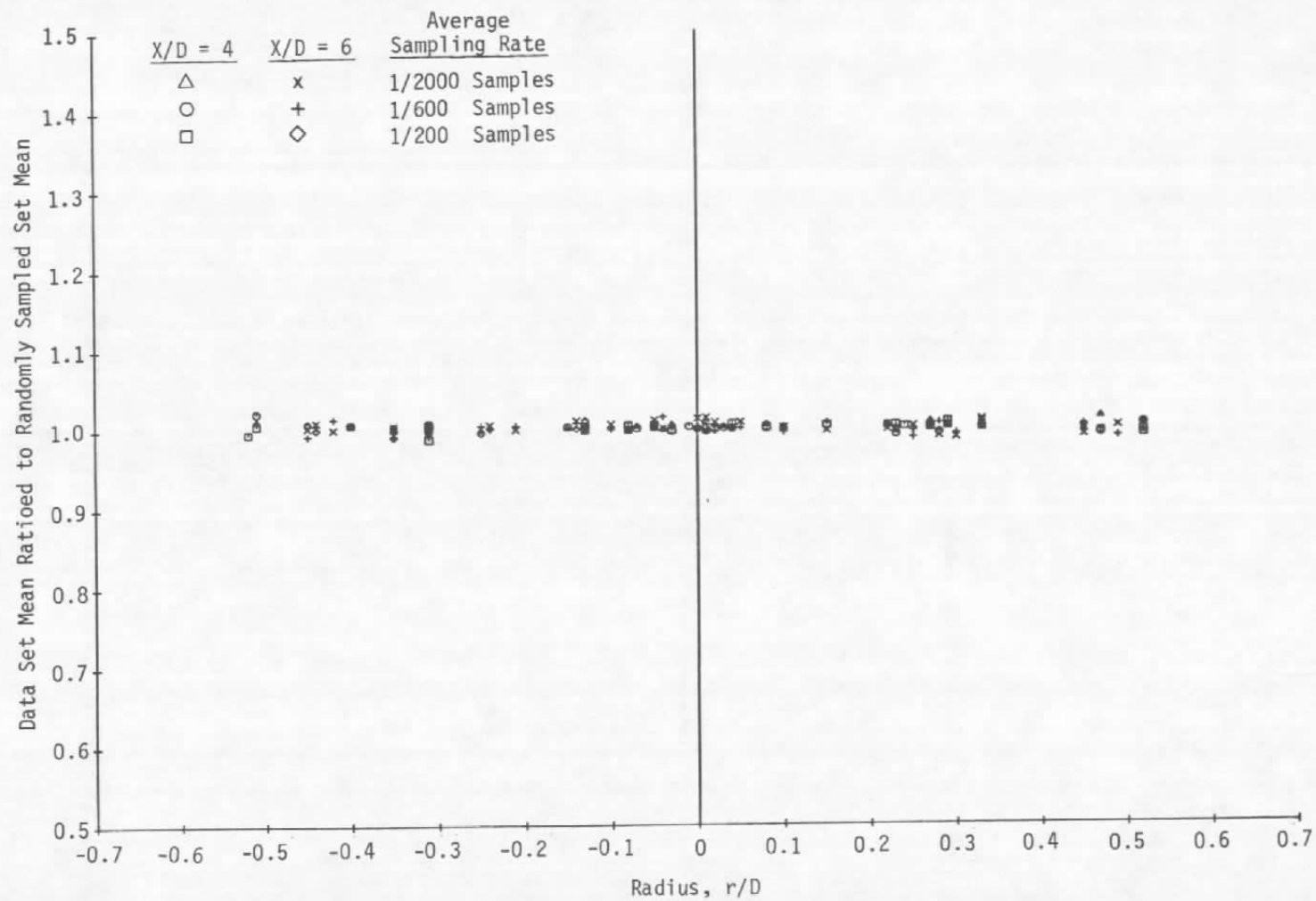
compared with averages of randomly selected data. The selection was done several times, first selecting one sample at random from each 200 recorded samples, then one from each 600, and finally one from each 2,000 recorded samples. The ratio of the original IRLV data average to the randomly selected data average for various radial locations at X/D of 4 and 6 is shown in Fig. 19a. The ratio of the original IRLV data root-mean-square average to the randomly selected root-mean-square for the same X/D locations is shown in Fig. 19b. There is no evidence of statistical bias in either data set.

2.4 ANALYSIS OF INFLUENTIAL FACTORS

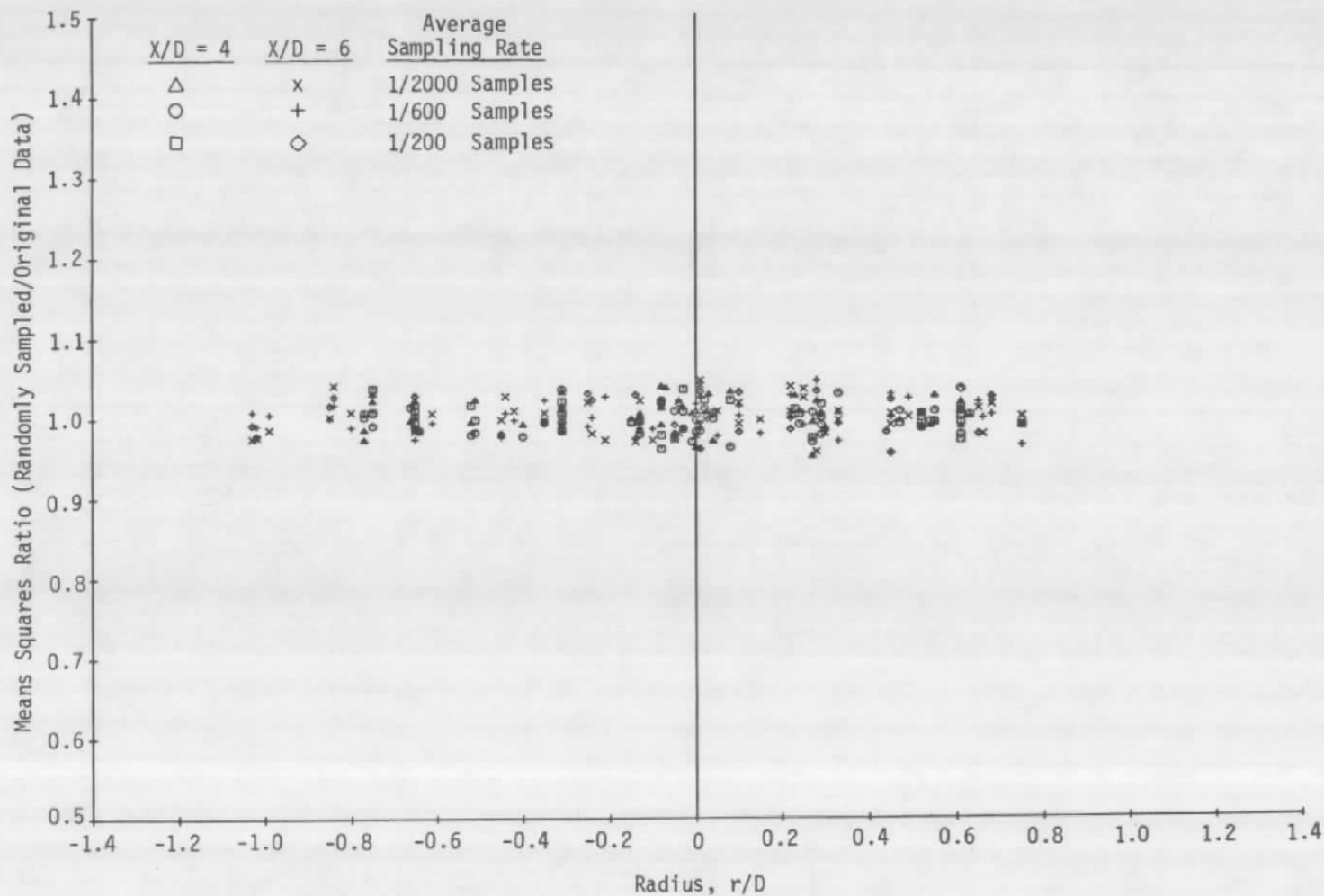
Based on the preceding results, the magnitude of IRLV statistical bias can be much less than predicted by the theory outlined previously. Several factors, which could have reduced the bias magnitude in the preceding results, will be examined to determine if the lack of bias might be unique to these results. The factors examined include (1) the relationship between sampling rate and turbulence structure, (2) processing rates possible with a given data acquisition system, and (3) fluctuations in the local particle concentration.

2.4.1 Sampling Rate

In Ref. 20, Barnett and Bentley concluded that the bias between arithmetic and time-integrated averages of IRLV data will decrease as the sampling rate per primary flow frequency goes down. This conclusion can be supported using the previously presented theory by evaluating the case when the time interval between detections, Δt_i , is large compared to the flow integral time scale, L_T . In this limiting case, as the average interval time to integral scale ratio, $\langle \Delta t \rangle / L_T$, becomes large, the velocity average between detections, \hat{V}_i , will approach the temporal mean velocity, \hat{V} , and, from Eq. (3) arithmetic averages will approach approximate temporal averages. As a result, if the approximate temporal averages are still good approximations of the true temporal averages as



a. Ratio of velocity means
Figure 19. Effect of data randomization.



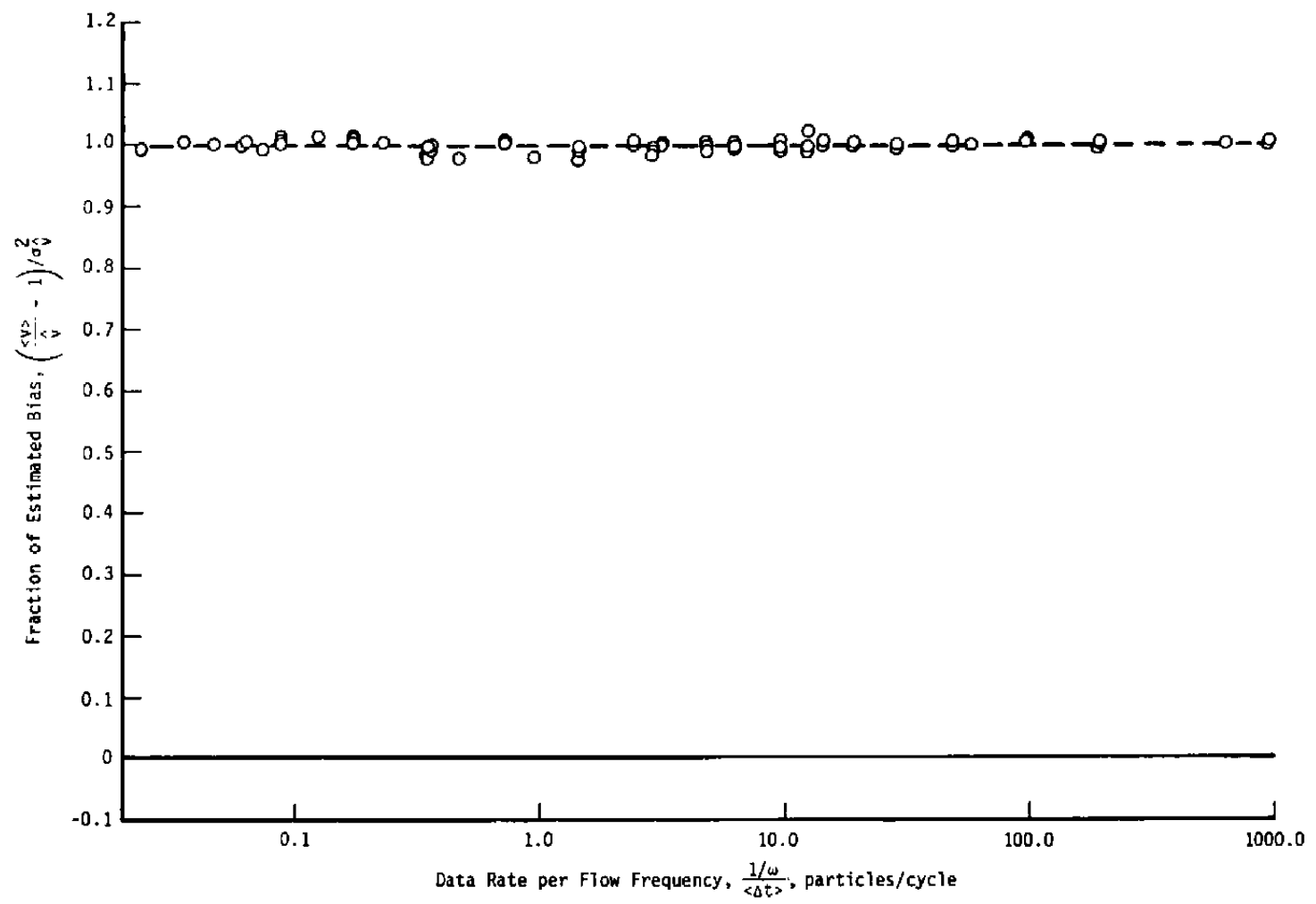
b. Ratio of velocity variance
Figure 19. Concluded.

the time between detections becomes much larger than the integral time, L_T , then statistical biasing must eventually decrease with increasing time between detections and finally disappear.

To examine the possible dependence of statistical bias on data rate, IRLV signals were simulated in a numerical experiment. In this simulation a function was generated to represent the flow velocity in the probe volume at time t . Velocities were then recorded as particle realizations every time a specified amount of fluid entered the probe volume. For consistency with the bias theory, negative velocities were not allowed to recirculate particles through the probe volume. Initially, a sinusoidal velocity $V = V_0 + V_1 \sin(\omega t + \phi)$ was assumed for comparison with the particle-per-main-flow frequency criteria of Ref. 20. The quantity $\overline{\Delta t}/L_T$, given in this case as $\overline{\Delta t}/(1/\omega)$, was varied by changing either ω or the specified fluid mass separating particles. Both the arithmetic average velocity and the approximate-time-integrated average velocity were compared with the true time-averaged velocity.

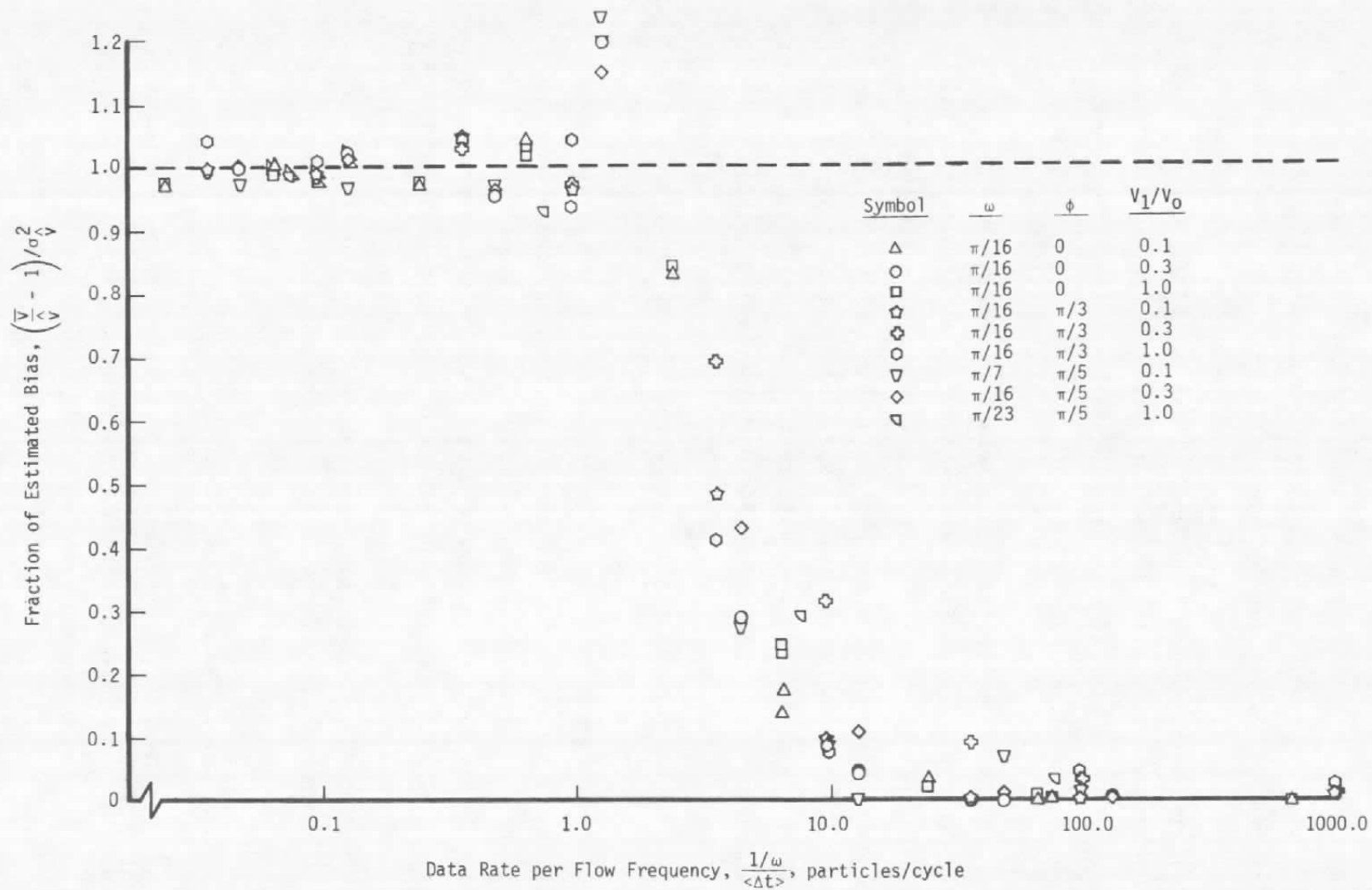
The results of the simulation are shown in Fig. 20. Since all theorized statistical bias conditions are met perfectly in this simulation, the quantity $(\langle V \rangle / \hat{V} - 1) / \sigma_V^2$ should vary between unity for completely biased cases and zero for unbiased cases. Excursions beyond these limits result when the sampling occurs as a multiple of the flow frequency.

As indicated in Fig. 20a, the bias in arithmetic averages is not reduced when the average time between detections is large (i.e., the data rate per flow frequency is small) as suggested above. However, in the above analysis bias will be eliminated only when the time between detections is large enough to drive the product $\frac{2L_T}{\langle \Delta t \rangle} \overline{(V_1 - \hat{V})^2}$ in Eq. (12) toward zero. For the data shown in Fig. 20a, the lowest value of the product $\frac{2/\omega}{\langle \Delta t \rangle} \overline{(V_1 - \hat{V})^2}$ is greater than $18 \text{ ft}^2/\text{sec}^2$. To decrease this product to near zero (three orders of magnitude) requires a corresponding



a. Arithmetically averaged data, $\langle v \rangle$

Figure 20. Simulation program predictions of sampling rate effect on the velocity bias of a sinusoidal flow.



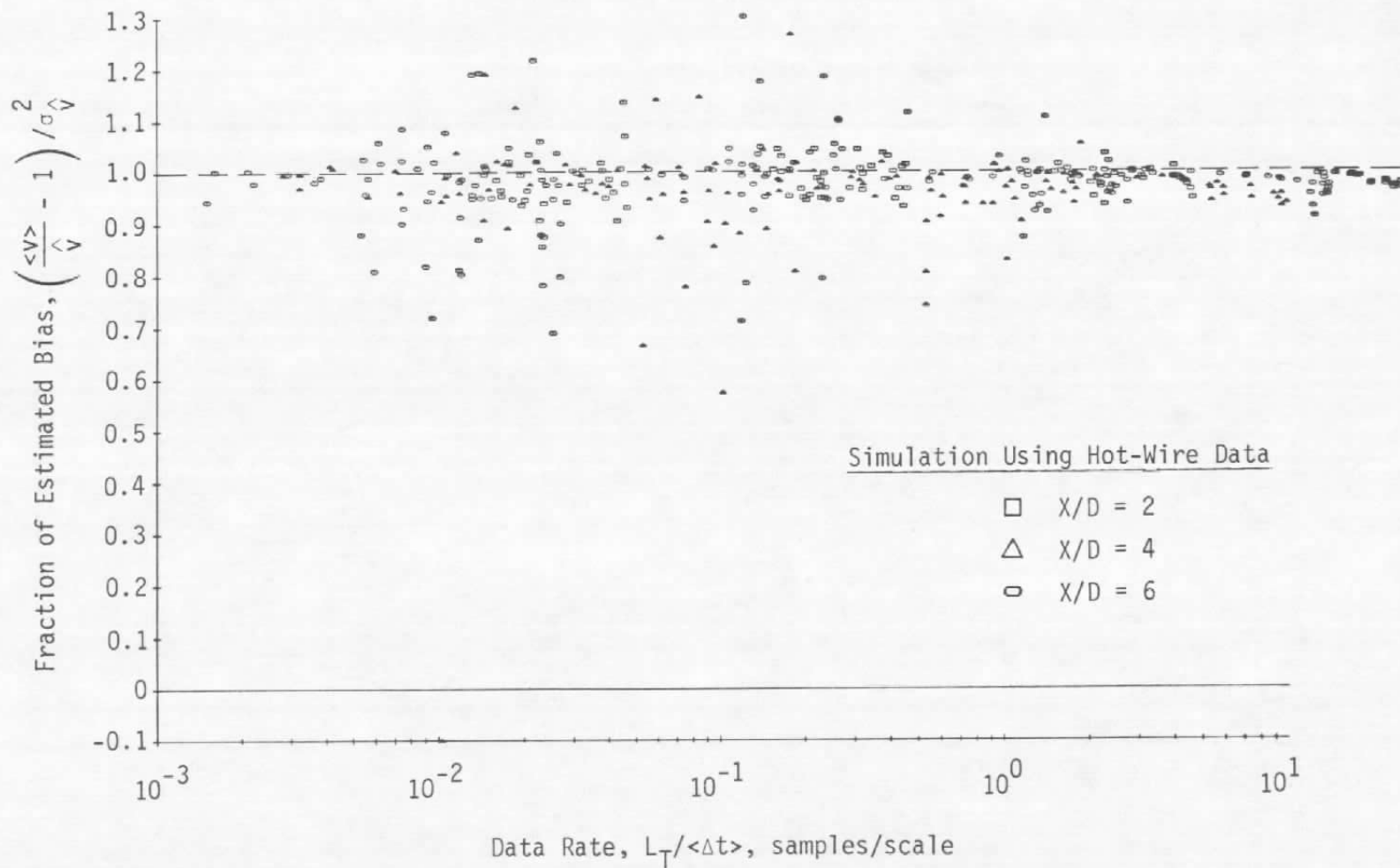
b. Approximate time — integrated data, \bar{v}
Figure 20. Concluded.

decrease in the data rate to about 20 samples per hour. In the simulation the bias quantity $(\langle V \rangle / \hat{V} - 1) / \sigma_V^2$ is reduced to only about 0.8 at data rates approaching 20 samples per hour, and even lower data rates are required for completely unbiased arithmetic averages. These lower data rates will be much too low for practical use of a laser velocimeter. Simulation of the impractical lower data rates is not expedient because the large values of the average time interval require correspondingly long computer run times.

Figure 20b shows that at values less than one sample per flow frequency the approximate time-integrated velocity is biased. This verifies Barnett and Bentley's hypothesis that arithmetic averaging and approximate temporal averaging are equivalent when the particle interarrival time becomes long; this also indicates that approximate temporal averaging does not approximate true temporal averaging when the interarrival time is long. The different symbols in Fig. 20b represent simulations for different ω , ϕ , and V_1/V_0 values to illustrate that this conclusion is not limited to just one velocity-time history.

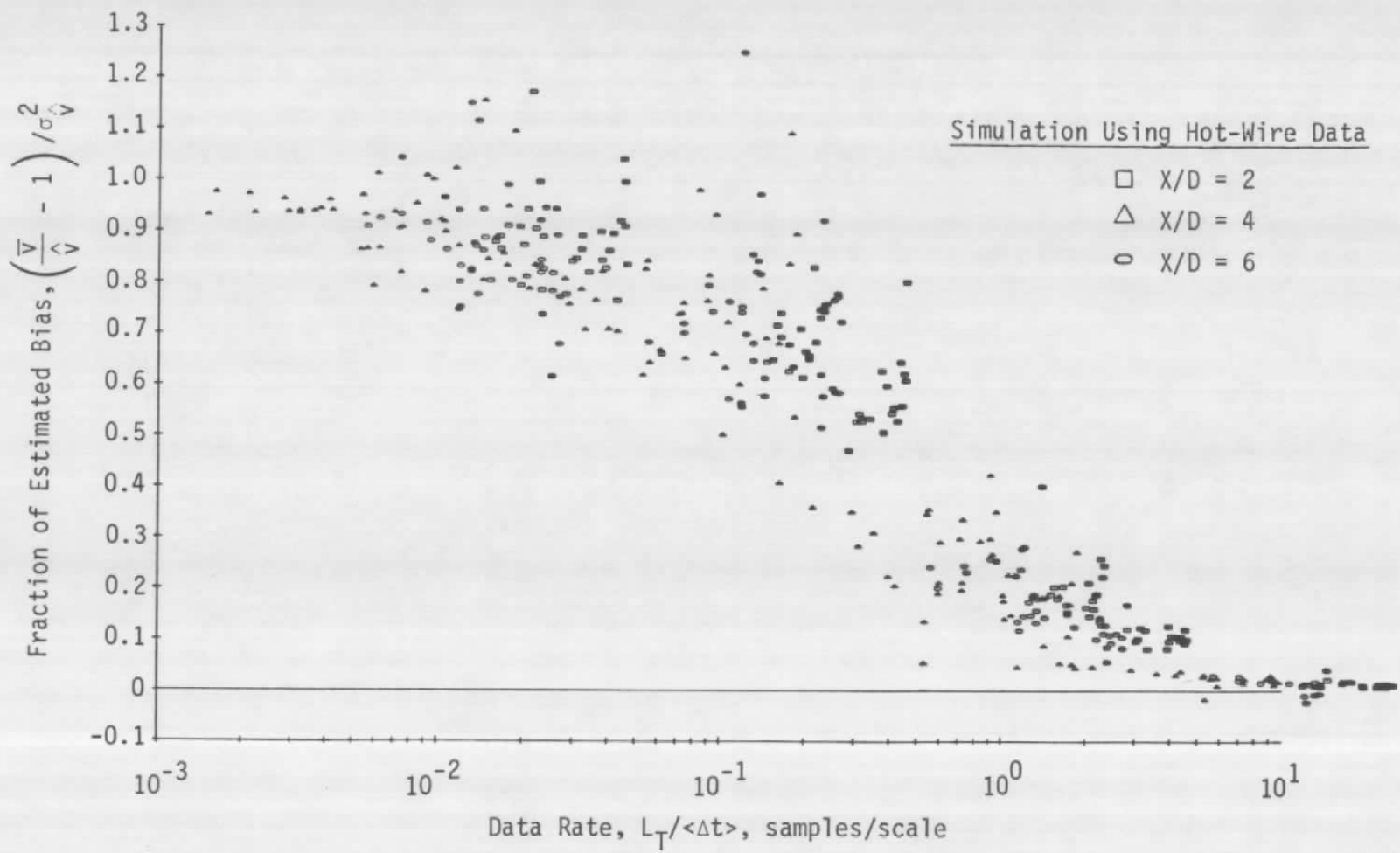
To examine the arithmetic and approximate time-integrated mean velocity for turbulent flow, the simulation was repeated using turbulent jet hot-wire measurements as the velocity-time function. The results, presented in Fig. 21, again show no bias reduction for arithmetic averages of theoretical IRLV data and show a biasing of the approximate time-integrated means at large interarrival times corresponding to low $L_T/\Delta t$. As in the sinusoidal simulation, a significant bias reduction of arithmetic averages could only be effected with impractically low data rates, i.e., less than two samples per hour.

The predicted biasing of approximate time-integrated averages of IRLV data is particularly important if approximate time-integration is used to avoid statistical biasing, as suggested in Refs. 20 and 48. As Fig. 21 illustrates, approximate time-integration will produce



a. Arithmetic average, $\langle v \rangle$

Figure 21. Simulation program predictions of the velocity bias of a turbulent flow.



b. Approximate time-integrated average, \bar{v}
Figure 21. Concluded.

averages that can be guaranteed unbiased only if the data rates are high enough that several samples are recorded per integral time scale. This would require data rates of 4,000 to 10,000 samples/sec in the experiments conducted in this investigation. Most IRLV data systems are not able to process and record data at such rates. Also, it is often not feasible to seed flows heavily enough to attain the necessary data rates without possibly altering the fluid velocity field.

2.4.2 Data Processing Rate

Statistical bias should result when the time between successive IRLV samples, Δt_i , is inversely proportional to \hat{V}_i , the fluid velocity average evaluated over Δt_i . However, the time between successively recorded IRLV realizations, Δt_j , may not be inversely proportional to \hat{V}_j even though the time separating each particle entrance into the probe volume obeys Eq. (9). This can happen simply if the time between some particles is less than the time needed to evaluate and record LV realizations. For example, if the IRLV instrumentation can only record 10 samples per second but an average of 1,000 particles enters the probe volume each second, then a particle will probably be in the volume when the LV is ready to process another sample. Hence the time, Δt_j , between recorded realizations will be nearly constant at 0.1 second and from the discussion following Eq. (2) arithmetic averages will be unbiased.

To analyze the effect that processing time, k_t , can have on statistical bias, the time between recorded samples is expressed as

$$\Delta t_j = k_t + \Delta t_j^* \quad (40)$$

where Δt_j^* is the delay time after the completion of a data acquisition cycle until the next particle arrival. From Eq. (2) the mean velocity can be expressed as

$$\bar{V} = \frac{\sum_{j=1}^N V_j (k_t + \Delta t_j^*)}{\sum_{j=1}^M (k_t + \Delta t_j^*)} = \langle V \rangle \left(1 + \frac{\frac{\langle \Delta t^* \rangle}{k_t} R_V \Delta t^*}{1 + \frac{\langle \Delta t^* \rangle}{k_t}} \right) \quad (41)$$

If the processing time is short then $\langle \Delta t^* \rangle / k_t$ is much greater than unity and Δt_j^* will approach Δt_i so that $\bar{V} \approx \langle V \rangle [1 + R_{V\Delta t}]$ as given by Eq. (6) for the mean velocity. The bias will, accordingly, approach that previously predicted. However, if $\Delta t^* / k_t$ is much less than one, as when the processing time is long compared to the particle interarrival times, the approximate integral mean velocity will approach the arithmetic mean and no bias should occur.

To estimate the relationship between the temporal and arithmetic averages of the data for intermediate values of processing time, it is necessary to estimate the form of the correlation coefficient $R_{V\Delta t^*}$. From Eq. (6),

$$\bar{V} = \langle V \rangle \left\{ 1 + R_{V\Delta t} \right\} \quad (42)$$

where, by evaluating Eq. (7) for the mean velocity,

$$R_{V\Delta t} = \langle V' \Delta t' \rangle / \langle V \rangle \langle \Delta t \rangle \quad (43)$$

Equation (20) requires further that

$$\bar{V} = \langle V \rangle \left\{ 1 + \sigma_v^2 \right\}^{-1} \quad (44)$$

Equating Eq. (42) and Eq. (44) shows explicitly that the velocity and time interval fluctuations are anticorrelated since

$$R_{V\Delta t} = -\frac{\sigma_v^2}{1 + \sigma_v^2} \quad (45)$$

If the processing time, k_t , is short compared to the interval between particle arrivals then, from Eq. (40), $\Delta t_i \approx \Delta t_j^*$ and $R_{V\Delta t^*} \approx R_{V\Delta t}$. This approximation will be made for all values of $\langle \Delta t^* \rangle / k_t$. Substituting Eq. (45) in (41) leads directly to

$$\bar{V} = \langle V \rangle \left[\frac{1 + \sigma_v^2 + \frac{\langle \Delta t^* \rangle}{k_t}}{(1 + \sigma_v^2) \left(1 + \frac{\langle \Delta t^* \rangle}{k_t} \right)} \right] \quad (46)$$

The bias parameter corresponding to this expression is shown in Fig. 22 as a function the dimensionless processing delay, $k_t / \langle \Delta t \rangle$. As the delay becomes large, the arithmetic and temporal averages converge; the net effect of a relatively slow data acquisition system is, then, to reduce bias. Processing delay times are not absolutely constant as assumed in the preceding analysis. For example, the delay may be regarded as the sum of processor recycle time, signal processing time, and data recording time. The processor recycle time is approximately 0.04 μ sec for the Model 8 DDP used in this study. The data acquisition system can record data at rates over 13,000 samples per second, so the time associated with recording was at most 77 μ sec. The signal frequency range in the experiment was 12.5 to 17 MHz so that, when the pulse stretching and required number of signal cycles associated with the DDP were considered, signal processing times ranged from 60 to 80 μ sec. Consequently, the total delay between successive samples was, at most, 160 μ sec. The maximum average data rates encountered were approximately 4,000 samples/sec, making $k_t / \langle \Delta t \rangle \approx 0.7$ in the worst case. Figure 22 shows, therefore, that the bias magnitudes associated with the present system should always be greater than 60 percent of the maximum possible in the experiments. Even when multidimensional effects and instrumentation uncertainties were also considered, the present experiments should have detected any consistent biasing of the IRLV results, but none was found.

The random-sampling algorithm (Ref. 25) should affect bias in much the same way as a constant processing delay, except that the algorithm introduces random rather than constant delays between velocity realizations. Thus, since constant delays are effective only when the delay time is long, random sampling will be effective only if the random delays are, on the average, long and only a few samples are selected from a large data set, as shown by Durao and Whitelaw (Ref. 25). To verify the effectiveness of the procedures used to randomize the experimental data, the same procedures were used to randomize data generated by the

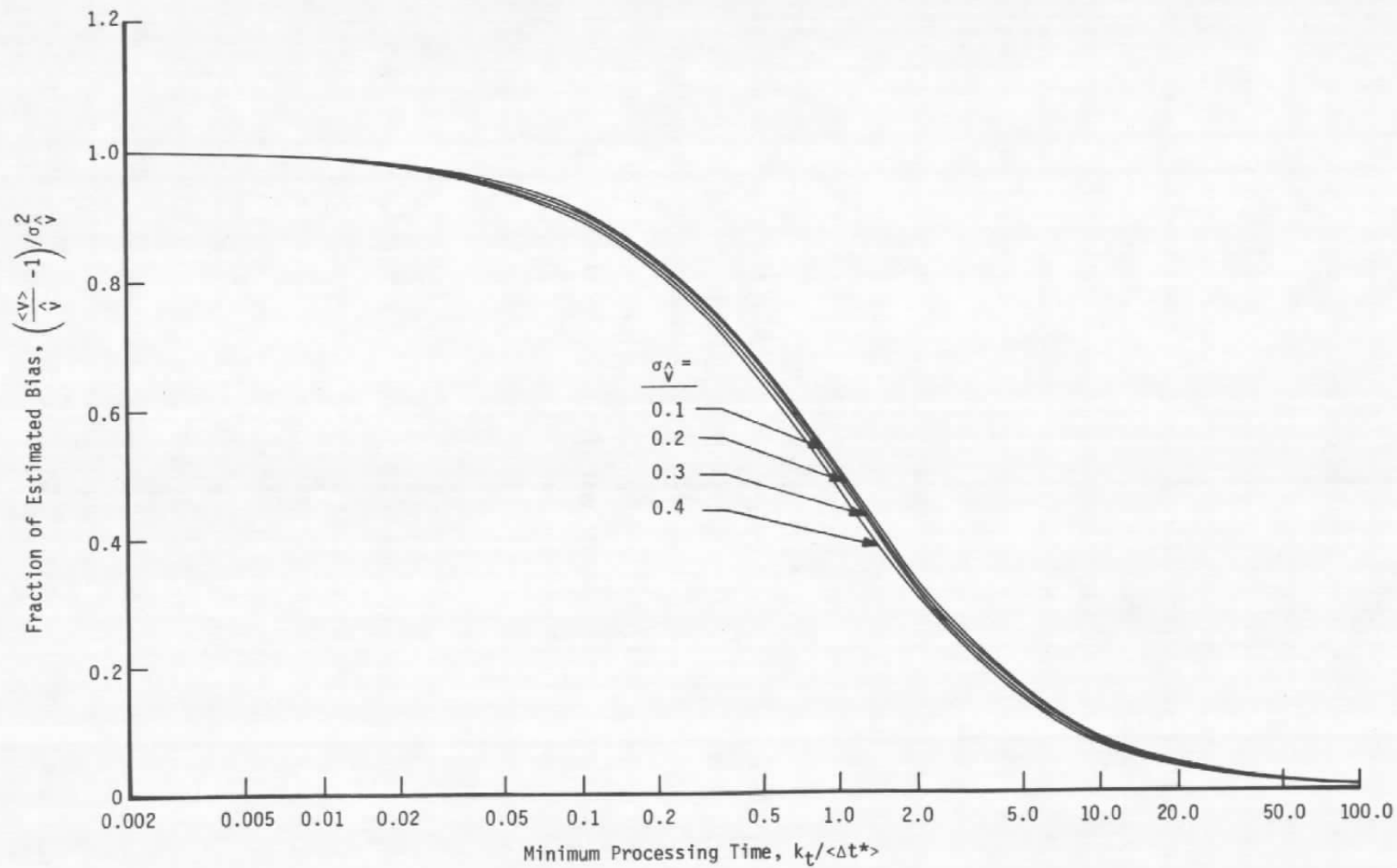


Figure 22. Bias reduction resulting from minimum processing time.

numerical simulation with the hot-wire velocity-time function. Random selection of 500 samples from sets of 2,000 often effected a significant bias reduction, regardless of the selection rate, but only when the data rate in the numerical simulation was high. For low simulated data rates random selection was often ineffective. Thus, digital randomization is not as effective as the random time processor on-off circuit described in Ref. 25 because digital randomization cannot be expected to be equivalent to a random time-sampling procedure. However, since the digital randomization was occasionally effective, it should provide evidence of significant bias of IRLV measurements not made using a random time sampling circuit.

2.4.3 Particle Concentration Fluctuations

The correlation between velocity and interarrival time fluctuations, which forms the basis for statistical bias theories, assumes that particle concentration at a point is invariant. This condition is extremely hard to obtain in practice, as was noted in Ref. 39 and observed in the present experiments. As an aid in understanding the experimental results, a theory can be developed for those cases where the particle concentration as well as fluid velocity is time dependent.

For this purpose a formal averaging procedure first reported by Cline and Bentley (Ref. 41) can be used. The fluid velocity at a point is accordingly, defined by

$$\bar{f} = \sum_{k=1}^M P(f_k) f_k \quad (47)$$

where $P(f_k)$ is the probability that the variable f will have the particular value f_k . Likewise, the arithmetic averages of the individual realizations of velocity are

$$\langle f \rangle = \frac{1}{S_M} \sum_{k=1}^M S_k f_k \quad (48)$$

where S_k is the number of realizations that occur in some interval $f_k \pm \Delta f$ and S_M is the total number of samples. The ratio S_k/S_M is the probability that the particular value f_k occurs in the IRLV data. Now S_k is the product of the total sampling time, T_t , and λ_k , the sampling rate for the occurrence of the f_k events. Thus,

$$S_k = T_t \lambda_k = T_t N_k A V_k P(V_k) \quad (49)$$

and Eq. (48) becomes

$$\langle f \rangle = \frac{\sum_{k=1}^M N_k V_k f_k P(V_k)}{\sum_{k=1}^M N_k V_k P(V_k)} \quad (50)$$

The particle concentrations and velocities corresponding to the k^{th} interval are, respectively,

$$\begin{aligned} N_k &= \bar{N}_k + N'_k \\ V_k &= \bar{V}_k + V'_k \end{aligned} \quad (51)$$

so that Eq. (50) may be rewritten for the mean velocity as

$$\langle V \rangle = \bar{V} \left(\frac{1 + \sigma_v^2 + 2R_{NV} + R_{NV}^2}{1 + R_{NV}} \right) \quad (52)$$

in which the correlations between the concentration and velocity fluctuations are

$$R_{NV} = \frac{\overline{N'(V')^n}}{\bar{N} \bar{V}} \quad (53)$$

Similarly, if $f = (V - \bar{V})^2$, Eq. (50) may be evaluated for the turbulence intensity in a flow characterized by particle concentration fluctuations:

$$\sigma_{\langle v \rangle} = \frac{\sigma_v}{1 + \sigma_v^2 + 2R_{NV}} \sqrt{1 - \sigma_v^2 - R_{NV} + S\sigma_v (1 - R_{NV}) - \frac{R_{NV}^2}{\sigma_v^2}} \quad (54)$$

In Eq. (54) third order or higher number-density velocity correlations have been neglected. Note further that when all correlations, $R_{NV} = 0$ Eqs. (52) and (54) reduce to Eqs. (20) and (22), respectively, thus establishing the equivalence of the two averaging techniques.

The predicted mean velocity and turbulence intensity bias for various number density-velocity correlations are shown in Figs. 23 and 24. As shown, even a small number density-velocity correlation can significantly alter the bias. No definitive conclusions can be reached as to the sign of the R_{NV} correlations in the present experiment. However, the R_{NV} correlation can be expected to be similar to the species-velocity correlation in flows in which several gases are mixing; these correlations are generally positive (Ref. 49) and should increase the bias.

Other mechanisms, such as particle lag effects, may reduce the bias in IRLV experiments. However, on the basis of the preceding analyses, where none of the postulated bias-reducing mechanisms alone was adequate to eliminate bias from the present data, it is unlikely that another mechanism will eliminate the bias. A possible explanation for the lack of bias in the present data may be simply that the cumulative effect of several mechanisms reduced the bias below measurable levels.

3.0 SIGNAL AMPLITUDE STUDY

Laser velocimeters can provide detailed information on the characteristics of a flow field from measurements of the velocity of light-scattering particles contained in a fluid. In most applications, however, the fluid velocity and not the particle velocity is of prime importance. Therefore, measurements must be taken to ensure that particle response to fluid transients meets a desired accuracy criterion. A satisfactory approach, where feasible, has been to perform particle dynamic calculations to estimate the largest particle size that adequately responds to the flow and then seed the flow with particles of that size or smaller.

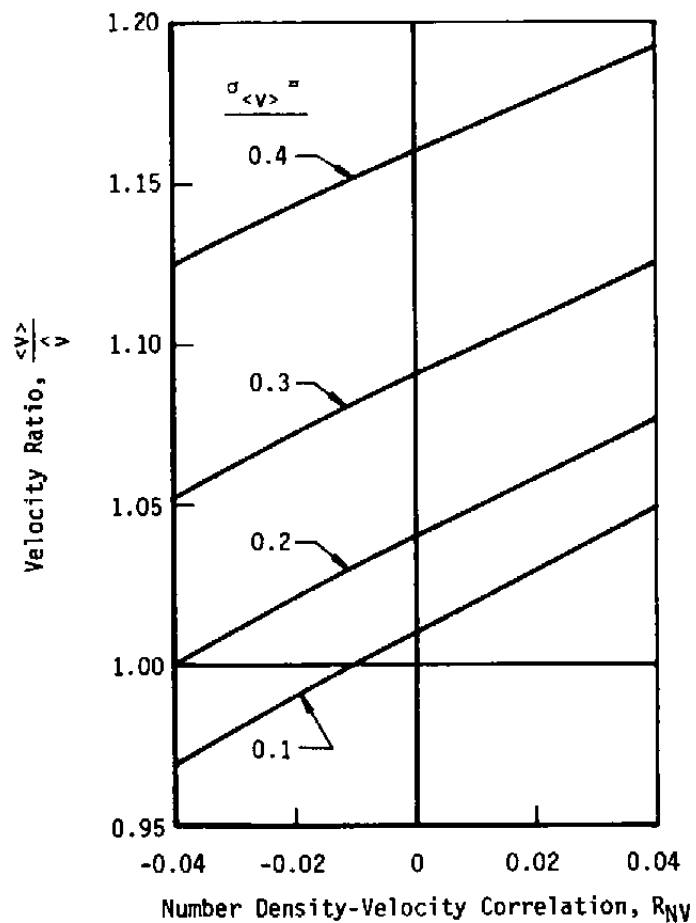


Figure 23. Magnitude of mean velocity bias for particle concentration fluctuations.

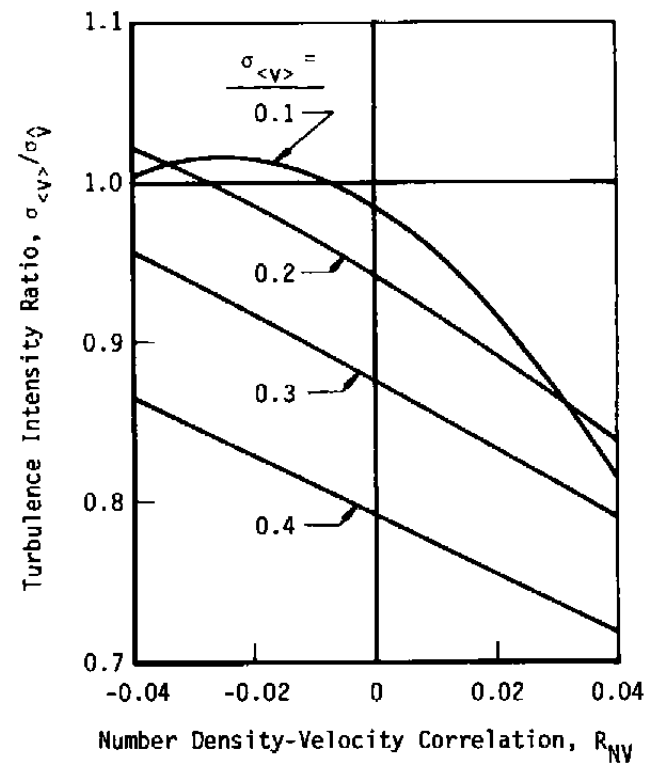


Figure 24. Magnitude of turbulent intensity bias for fluctuations in particle concentration.

Several difficulties are associated with the seeding approach. For example, particle response calculations require, *a priori*, an estimate of the fluid velocity and, in many cases, knowledge of the turbulent structure of the flow. Lacking this basic information, one can only try to obtain data from the smallest particles detectable by the LV used. Seeding the flow with small particles, moreover, does not guarantee that all of the data obtained arise from these particles. Agglomeration (see Section 2.3) or the presence of large detectable particles in the air supply may introduce measurements that make up a significant portion of the data set. Furthermore, seeding is not practical or desirable in many applications (Refs. 5 and 50); reliance then must be on intrinsic particulates whose sizes may range over one or two orders of magnitude.

Many of these difficulties could be avoided if an LV could be constrained to accept only data from particles whose sizes are less than some predetermined value. Prompted by these considerations, Pfeiffer and von Stein (Ref. 36) suggested that the amplitude of a Doppler burst could be used to discriminate against large particles. Data obtained downstream of an oblique shock substantiated this claim. On the other hand, Andrews and Seifert (Ref. 35) had only modest success in sizing particles on the basis of LV signal amplitudes. Holve and Self (Ref. 51), moreover, observed that the light-scattering amplitude characteristics of particles traversing a nonuniformly illuminated region (such as the probe volume of an LV) are trajectory dependent so that particles of widely varying sizes may generate bursts of similar amplitudes. In view of these considerations, the concept of discriminating against particles on the basis of Doppler burst signal amplitude presents interpretation problems that require further study before adoption into LV systems.

3.1 MIE SCATTERING CHARACTERISTICS

When an electromagnetic wave traverses a local inhomogeneity in refractive index, a portion of the wave energy is redirected (scattered)

as the result of reflection, refraction, and diffraction occurring at the wave-inhomogeneity interface. The analysis of such scattering phenomena can be considerably simplified if the dimension of the local disturbance is considerably less than the wavelength of the electromagnetic radiation (Rayleigh scattering) or, conversely, if it is much greater (geometric optics theory). Unfortunately disturbances comparable in size to particles of practical interest in LV measurements of fluid velocity are generally of the same order of magnitude as the wavelength. Therefore, the full Mie theory must be considered to estimate accurately the magnitude of the scattered radiation. Details of the solution of the boundary value problem solved by Mie (Ref. 52) and simplifications to the theory for particles have diameters much different from the illuminating wavelength are discussed at length in Refs. 53, 54, and 55. The theory, consequently, will only be summarized here to give sufficient background for understanding the various results reported below.

Consider a plane electromagnetic wave travelling in an infinite, homogeneous, isotropic, dielectric medium. If the electric field, \vec{E} , and magnetic field, \vec{H} , vectors are oriented in the (x,y) plane of the Cartesian coordinate system shown in Fig. 25, then the direction of propagation given by the Poynting flux vector, $\vec{S} = \vec{E} \times \vec{H}$ is directed along the z axis. The intensity of light at a point $P = P(r, \theta, \phi)$ attributable to scattering from a small homogeneous isotropic sphere located at the origin of the coordinate system is

$$J = \left(\frac{\lambda}{2\pi r} \right)^2 I \cdot F(\theta, \phi) \quad (55)$$

where J has the dimensions of (energy time⁻¹ area⁻¹), λ is the wavelength of the illuminating wave, I is the intensity of the illuminating wave, and $F(\theta, \phi)$ is an amplitude function describing the angular distribution of scattering. For computational convenience the electric field vector can be resolved into components perpendicular and parallel to the

"polarization" plane which is formed by the incident wave and the radius directed through the observation point. Accordingly, the intensity attributable to the component of the electric field vector perpendicular to the scattering plane is (Ref. 55)

$$J_{\perp} = \left(\frac{\lambda}{2\pi r} \right)^2 I |S_{\perp}|^2 \sin^2 \phi \quad (56)$$

whereas that parallel to the plane is

$$J_{\parallel} = \left(\frac{\lambda}{2\pi r} \right)^2 I |S_{\parallel}|^2 \cos^2 \phi \quad (57)$$

The amplitude functions required for evaluating Eqs. (56) and (57) are given by the series

$$S_{\perp} = \sum_{n=1}^{\infty} \frac{2n+1}{n(n+1)} \left\{ A_n \pi_n(\cos \theta) + B_n \tau_n(\cos \theta) \right\} \quad (58)$$

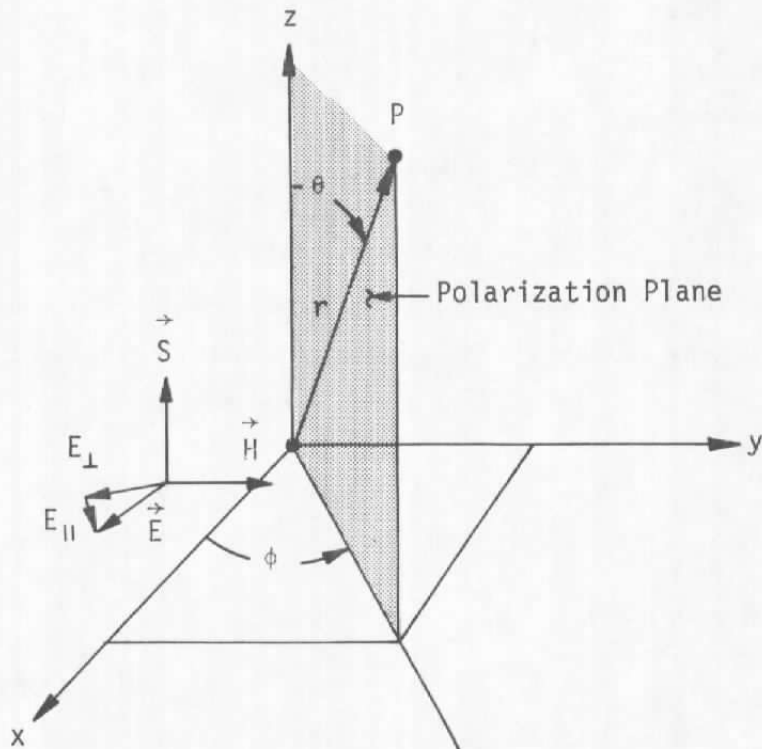


Figure 25. Mie scattering coordinate system.

and

$$S_{\theta} = \sum_{n=1}^{\infty} \frac{2n+1}{n(n-1)} \left\{ A_n \tau_n(\cos \theta) - B_n \pi_n(\cos \theta) \right\} \quad (59)$$

The functions τ_n and π_n are only dependent on the scattering angle, θ , and are defined in terms of the Legendre polynomials of a function x^* by the relations

$$\pi_n(x^*) = \frac{d P_n(x^*)}{d x^*} \quad (60)$$

$$\tau_n(x^*) = x^* \pi_n(x^*) - (1 - x^{*2})^2 \frac{d \pi_n(x^*)}{d x^*} \quad (61)$$

In evaluating the coefficients of the amplitude functions, however, the size parameter, $\alpha = \pi d_p / \lambda$, the ratio of the particle refractive index relative to that of the medium, $m = m_1 / m_2$, and the product $\beta = m \alpha$ must be introduced. The coefficients may then be expressed as

$$A_n = (-1)^{n+\frac{1}{2}} \left[\frac{Q_n(\alpha) Q_n'(\beta) - m Q_n'(\alpha) Q_n(\beta)}{\Phi_n(\alpha) Q_n'(\beta) - m \Phi_n'(\alpha) Q_n(\beta)} \right] \quad (62)$$

$$B_n = (-1)^{n+\frac{1}{2}} \left[\frac{Q_n'(\alpha) Q_n(\beta) - m Q_n(\alpha) Q_n'(\beta)}{\Phi_n'(\alpha) Q_n(\beta) - m \Phi_n(\alpha) Q_n'(\beta)} \right] \quad (63)$$

where primes denote differentiation of a function with respect to its argument. The Riccati-Bessel functions, $Q_n(x^*)$ and $\Phi_n(x^*)$, are defined in terms of the Bessel functions of the first kind of half-odd-integral order through

$$Q_n(x^*) = \left(\frac{\pi x^*}{2} \right)^{\frac{1}{2}} J_{n-\frac{1}{2}}(x^*) \quad (64)$$

and

$$\Phi_n(x^*) = Q_n(x^*) + (-1)^{n+\frac{1}{2}} \left(\frac{\pi x^*}{2} \right)^{\frac{1}{2}} J_{-n-\frac{1}{2}}(x^*) \quad (65)$$

With the above relations, local values can be computed for the intensity and phase of light scattered by spherical particles. For large particles, the series given by Eqs. (58) and (59) converge slowly so that many terms must be computed to minimize truncation errors. The coefficients A_n and B_n , moreover, are sensitive to precision errors in calculation so that evaluation of the scattering intensity for a wide range of parameters is practical only by computer. In recent years, several programs having the versatility needed for LV studies have been documented (Refs. 56, 57, and 58). These programs employ recurrence relations for the Bessel functions, double precision accuracy, and can evaluate the light-scattering amplitude for $\beta \leq 1,000$. The program by Dave (Ref. 58), as modified in Ref. 59 to account for media with complex refractive indices, was used for the Mie scattering calculations for the program MIELV described in Appendix B.

Several definitions are useful in presenting the Mie scattering calculations. The intensity functions are defined as

$$i_{\perp}(\theta) = |S_{\perp}(\theta)|^2 \quad (66)$$

$$i_{\parallel}(\theta) = |S_{\parallel}(\theta)|^2 \quad (67)$$

For either $\theta = 0$ deg or 180 deg, $i_{\perp}(\theta) = i_{\parallel}(\theta) \equiv i(\theta)$ so that there is no distinction between perpendicular or parallel polarization of the light wave at these scattering angles. It is convenient, therefore, to nondimensionalize the intensity function with $i(0)$. The resulting normalized intensity functions are labeled $i^*(\theta)$.

The influence of particle size on the on-axis forward ($\theta = 0$) and backscatter ($\theta = 180$ deg) intensity functions is shown in Fig. 26 for particles scattering light in a nonabsorbing medium for a relative refractive index of $m = 1.33$. For wavelengths on the order of $0.5 \mu\text{m}$, such as those used in the LV described in Section 2.2, the particle size range corresponding to Fig. 26 is $0.3 < d_p < 16 \mu\text{m}$. The relative

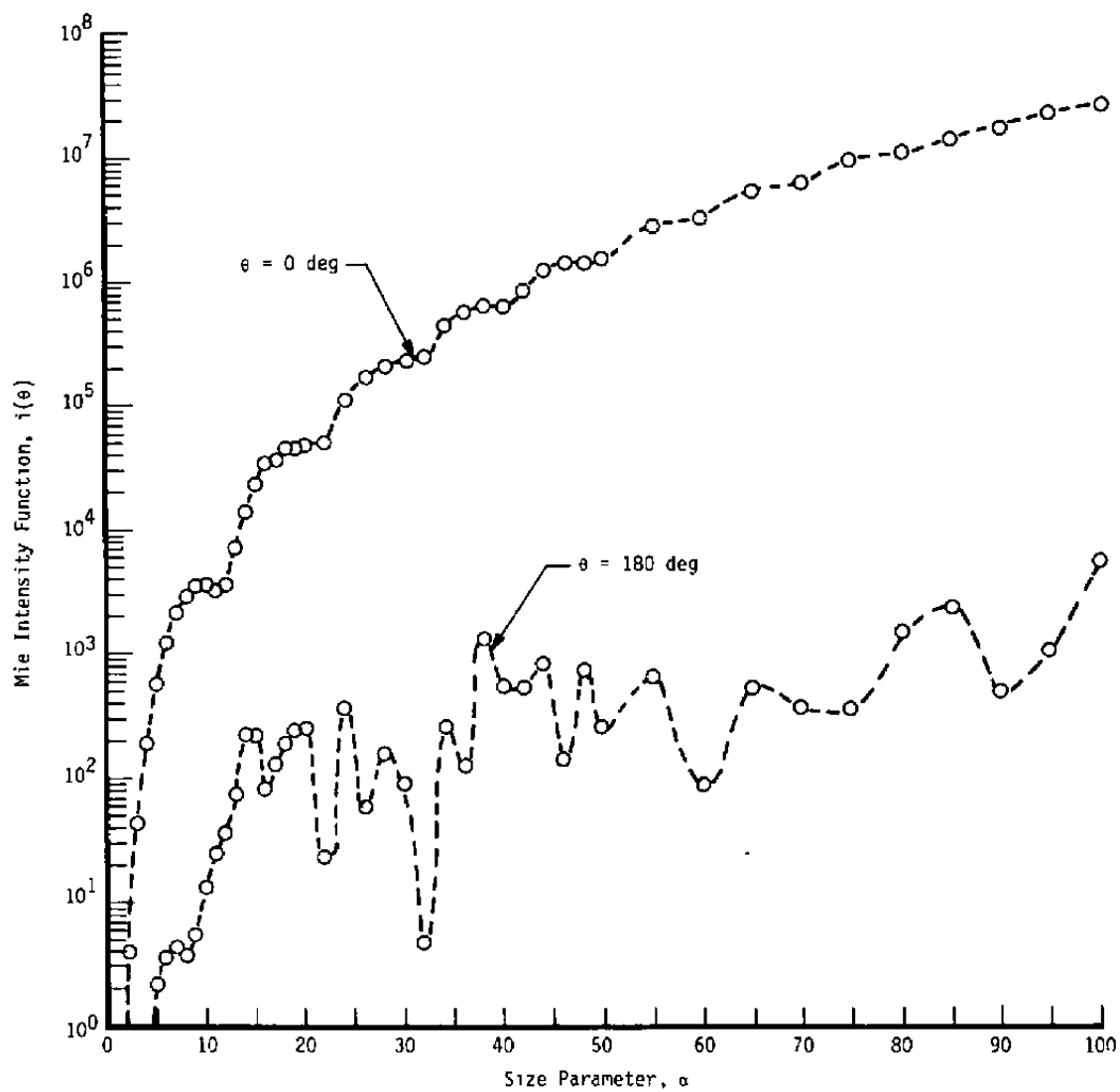


Figure 26. Variation of Mie intensity with particle size parameter for water droplets ($m = 1.33$).

refractive index corresponds to water droplets in air. The forward-scatter intensity increases nearly monotonically with the size parameter, but the functions for backscatter vary in an irregular manner for $\alpha > 15$. Generally, the intensity functions are extremely variable in any of the primary variables (θ , m , or α), and interpolation between computed values is subject to error.

To assess the influence of refractive index on the results, the forward-scatter intensity function for several particle sizes and refractive indices up to $m = 2.0$ is shown in Fig. 27. Refractive index clearly has a pronounced effect on the intensity function for small particles where $i(\theta)$ varies over two orders of magnitude, but the influence diminishes with increasing particle size. Small changes in refractive index, however, may result in greater variations in the intensity function for large particles because of the increased variability in $i(\theta)$. Representation of the intensity function in backscatter is more complex, as would be expected from Fig. 26 where it is shown that small changes in α lead to wide variations in $i(180 \text{ deg})$. For convenience, the normalized intensity, $i^*(180 \text{ deg})$, is plotted versus the parameter $\beta = m\alpha$ to minimize overlapping of the results with increasing refractive index. Typical results in Fig. 28 show that small changes in refractive index as well as particle size can lead to significant variations in the backscatter intensity function.

The effect of scattering angle on the normalized intensity functions, $i_{\perp}^*(\theta)$ and $i_{\parallel}^*(\theta)$, for various relative refractive indices is shown in Figs. 29 and 30 for particle size parameters of $\alpha = 3.053$ and 12.212, respectively. The value $m = 1.46$ is typical of oleic acid (Ref. 60), and $m = 1.72$ is representative of the Al_2O_3 particles (Ref. 61) used as seed material in the bias study. For $\lambda = 0.5 \text{ }\mu\text{m}$, the particle sizes represented by the figures are nominally $d_p = 0.5$ and $2.0 \text{ }\mu\text{m}$. For the smaller particle (Fig. 29), significant decreases in scattering intensity are noted near 60 and 150 deg for the perpendicularly polarized

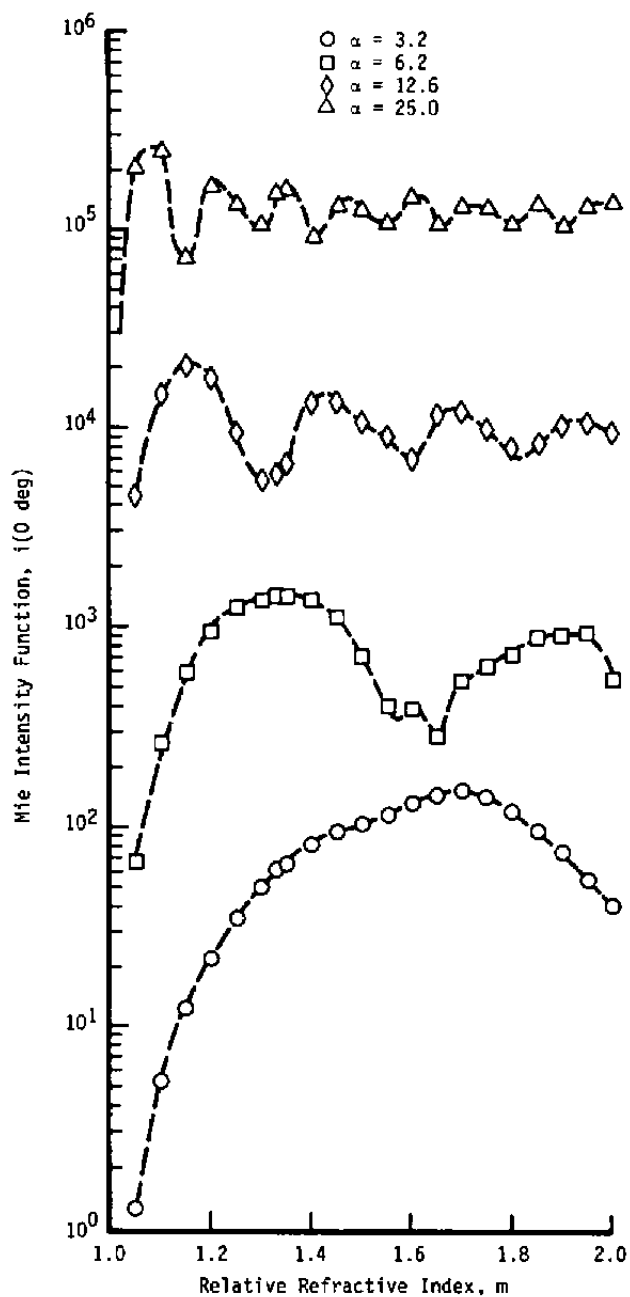


Figure 27. Effect of refractive index on Mie intensity function in forward scatter ($\theta = 0 \text{ deg}$).

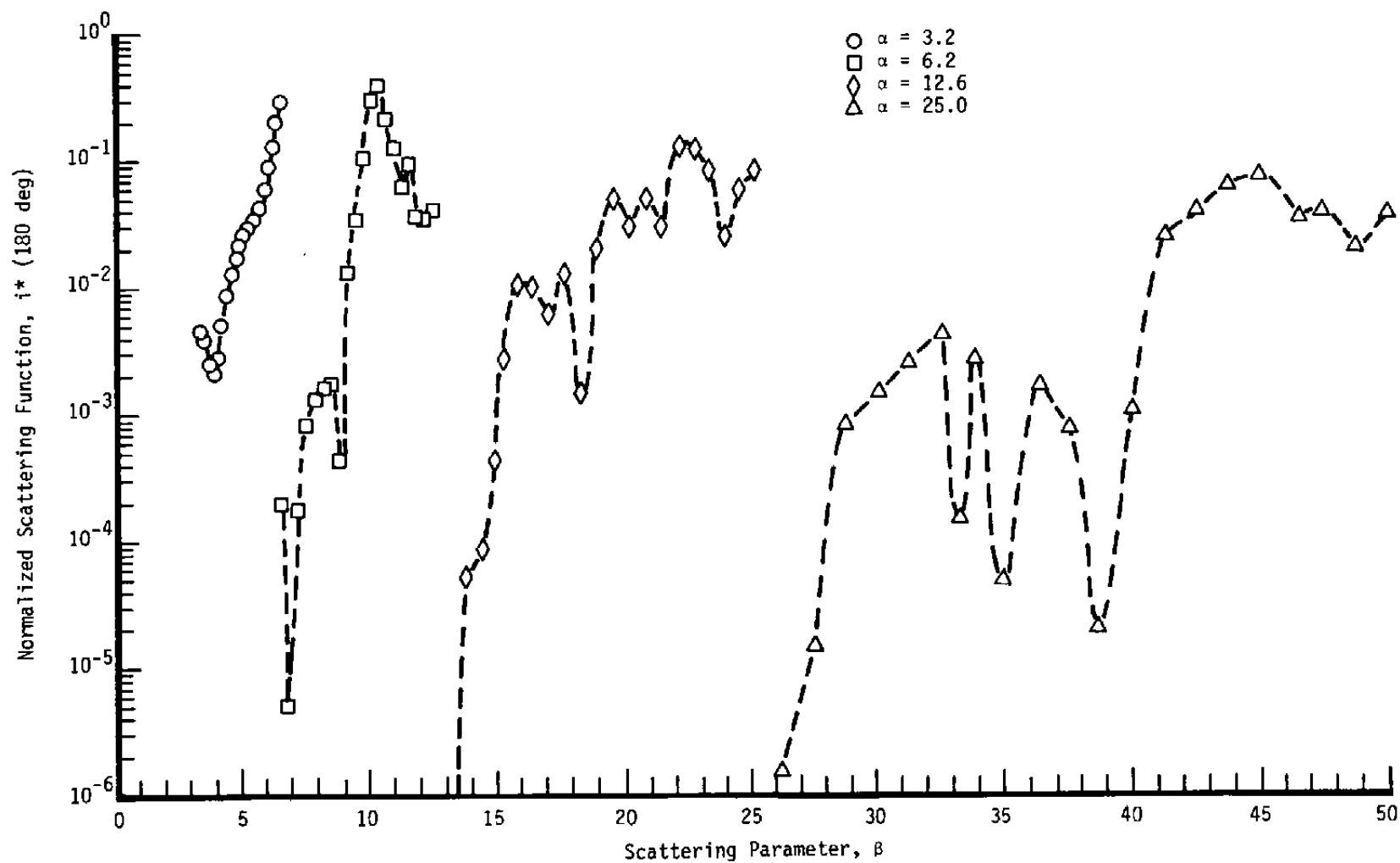
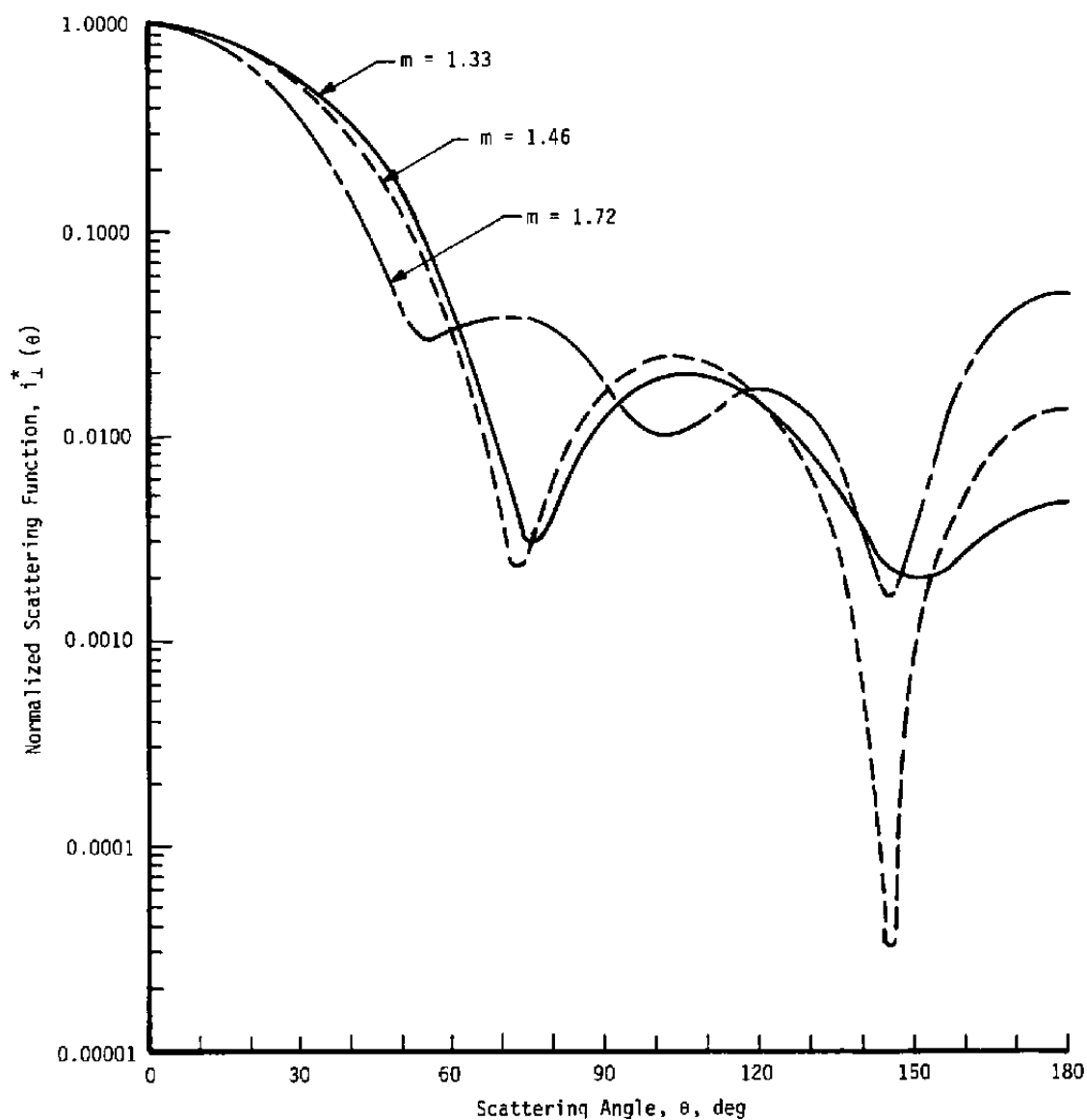
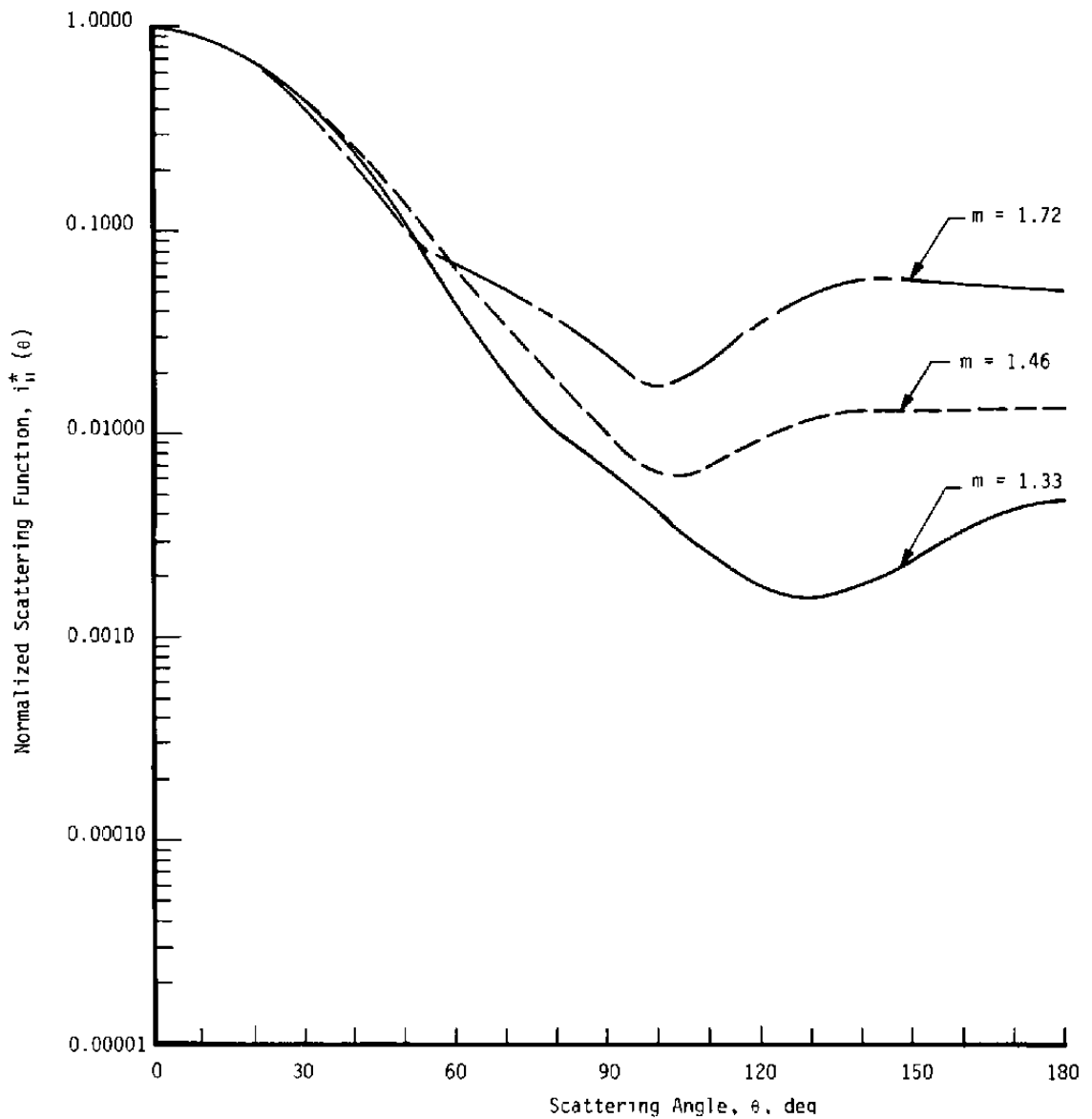


Figure 28. Effect of refractive index on normalized Mie intensity in backscatter ($\theta = 180$ deg).



a. Perpendicular polarization

Figure 29. Effect of scattering angle on intensity functions ($a = 3.05$).



b. Parallel polarization
Figure 29. Concluded.

results, but these effects are less pronounced for parallel polarization. The results for the larger particle (Fig. 30) show that the situation is decidedly more complex at large values of α . This suggests that an LV with the polarization component perpendicular to the scattering plane could have greatly decreased signal amplitudes for some particle sizes and refractive indices. Note that the normalized intensity function for on-axis backscatter detection is considerably greater ($i^* \approx 10^{-1}$ to 10^{-2}) than the $i^* = 10^{-3}$ value frequently quoted in general discussions (e.g., Ref. 62) of LV signal amplitudes.

3.1.1 Collector Optics

The preceding results show that the signal amplitudes to be expected from particles traversing the probe volume will vary significantly with changes in particle size, refractive index, or scattering angle. In practice, however, the collector optics of an LV will integrate the scattered signals over a region in space which will tend to damp the extreme variations noted, especially in backscatter. The rate at which energy is received by the collector lens is

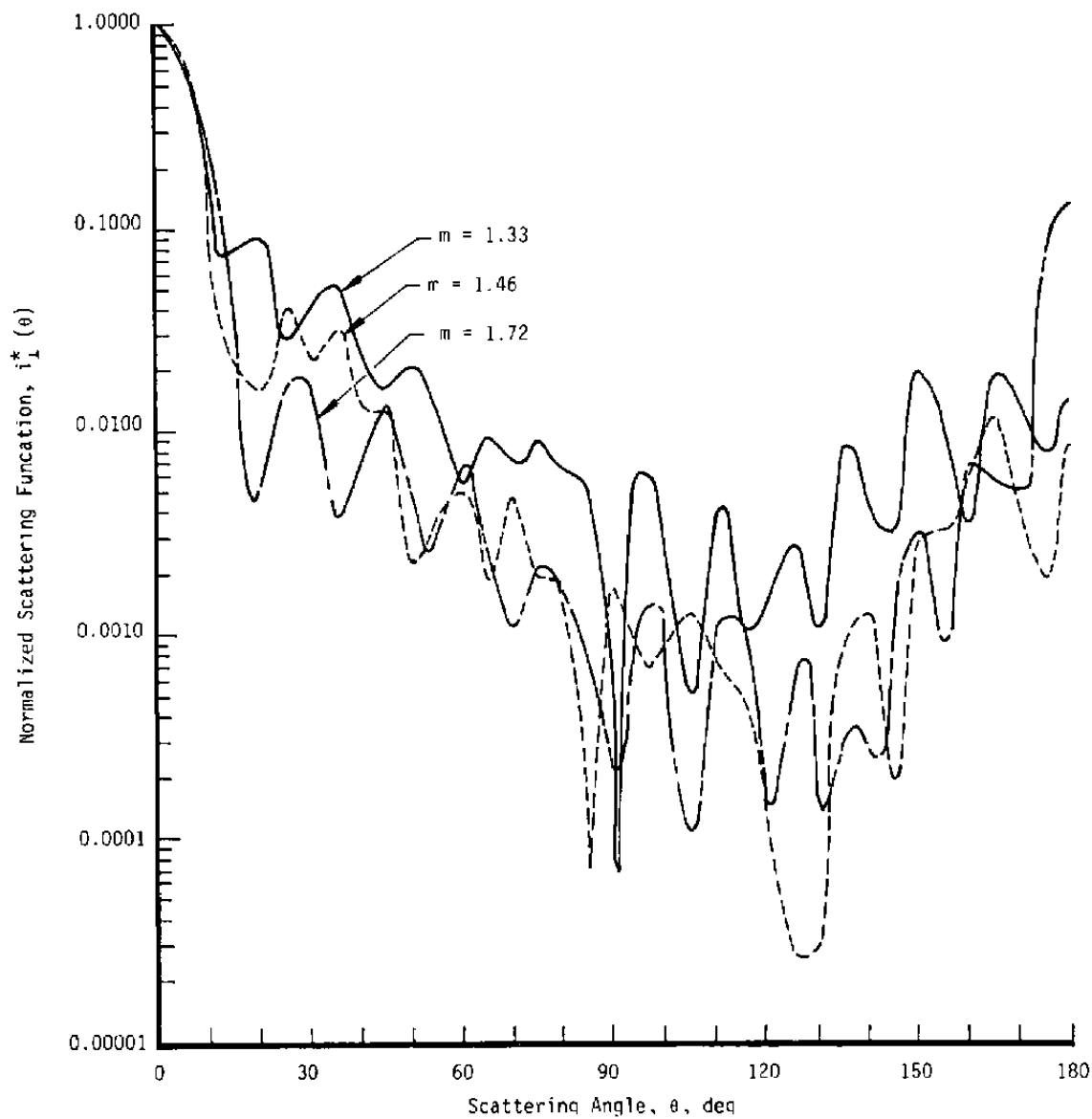
$$E_c = \iint_{S_c} J dS_c \quad (68)$$

where S_c is the collector lens surface area. Working with the polarization components described by Eqs. (56) and (57) suggests introducing the definitions

$$E_{c_{\perp}} = \left(\frac{\lambda}{2\pi} \right)^2 I \iint_{S_c} r^{-2} i_{\perp}(\theta) \sin^2 \phi dS_c \quad (69)$$

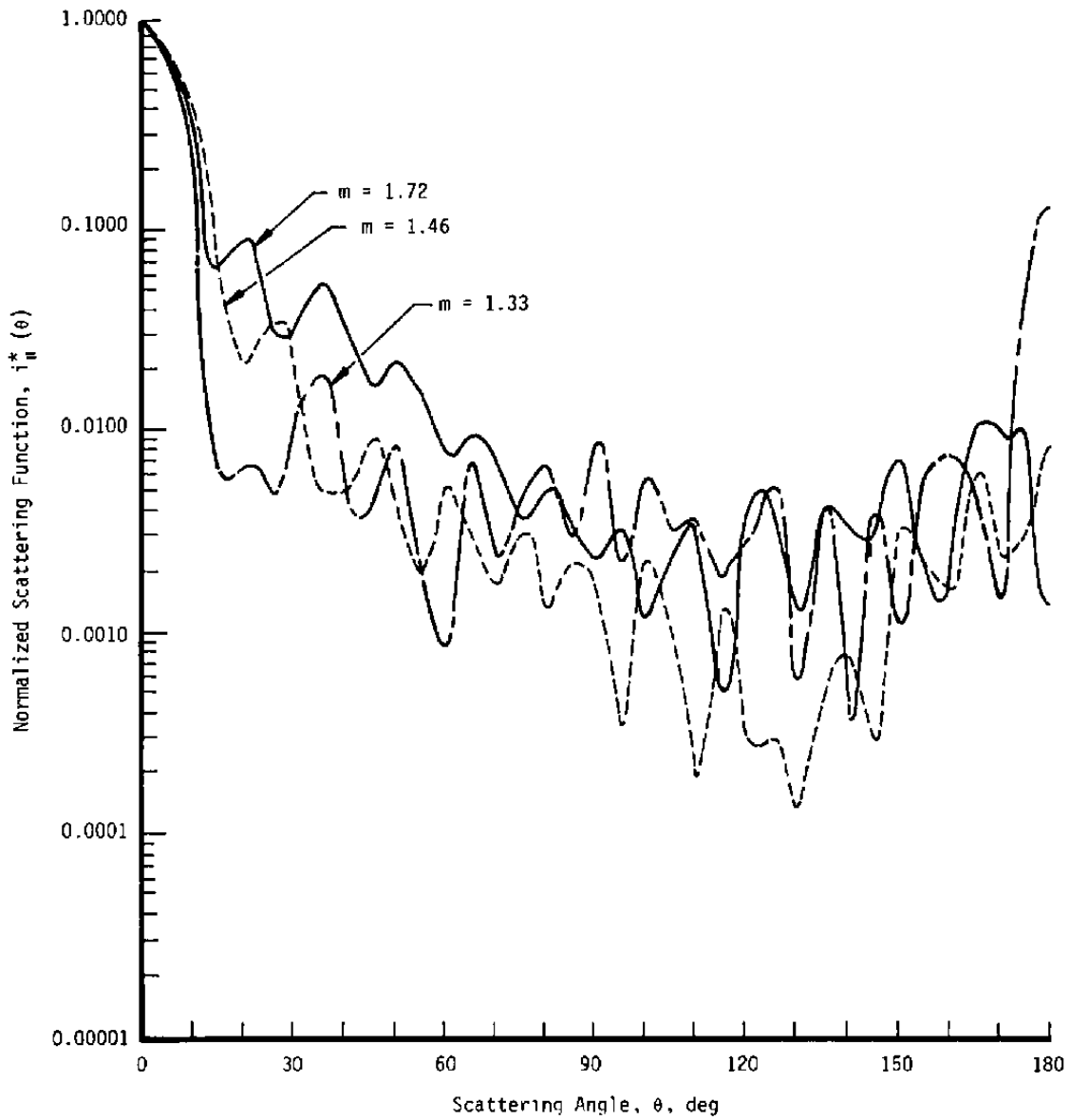
$$E_{c_{\parallel}} = \left(\frac{\lambda}{2\pi} \right)^2 I \iint_{S_c} r^{-2} i_{\parallel}(\theta) \cos^2 \phi dS_c \quad (70)$$

Although the integrations indicated in Eqs. (68) through (70) are amenable to closed-form solution for certain collector lens geometries, more general results can be obtained by numerical techniques. In MIELV (Appendix B), the integration is performed for a lens of radius R of



a. Perpendicular polarization

Figure 30. Effect of scattering angle on intensity functions ($a = 12.21$).



b. Parallel polarization
Figure 30. Concluded.

focal length L located at $L = r$ in the scattering coordinate system of Fig. 25. The solid angle of the collector is then $\Omega_c = \pi R^2/L^2$ and the lens f-number is $f = L/2R$. In Figs. 31 and 32, the variation of the dimensionless captured energy with scattering angle is shown for a range of f-numbers. For these calculations both circular (i.e., random) polarization

$$i(\theta) = \frac{i_{\perp} + i_{\parallel}}{2} \quad (71)$$

and a refractive index of $n = 1.54$ corresponding to natural particulates in air (Ref. 63) have been used. The indicated scattering angle corresponds to the midpoint of the lens. For the small-particle ($\alpha = 3.05$) and large-particle ($\alpha = 12.2$) calculations a decrease in lens f-number, and a corresponding increase in the lens solid angle, Ω_c , smooths local variations in the detected energy. Consequently, the scattering detected by the LV collector optics can be made less erratic by simply increasing the collector lens solid angle. This trend will obviously enhance the ability of an LV system to discriminate against large particles in backscatter systems because severe decreases in signal amplitude could cause the signal amplitude of a large particle to approach or be less than the signal level of a smaller particle at some scattering angles.

3.1.2 Illuminating Intensity

Because of the nonuniform illuminating intensity in the LV probe volume, signal amplitudes perceived by the Doppler data processor depend upon the trajectory of a particle as it sweeps through the fringe system. To examine the trajectory dependence both the geometry and apparent variation of intensity in the probe volume must be considered. Both matters have been discussed in detail in Refs. 29, 62, and 64, and the model proposed by Brayton (Ref. 64) will be used in the following development.

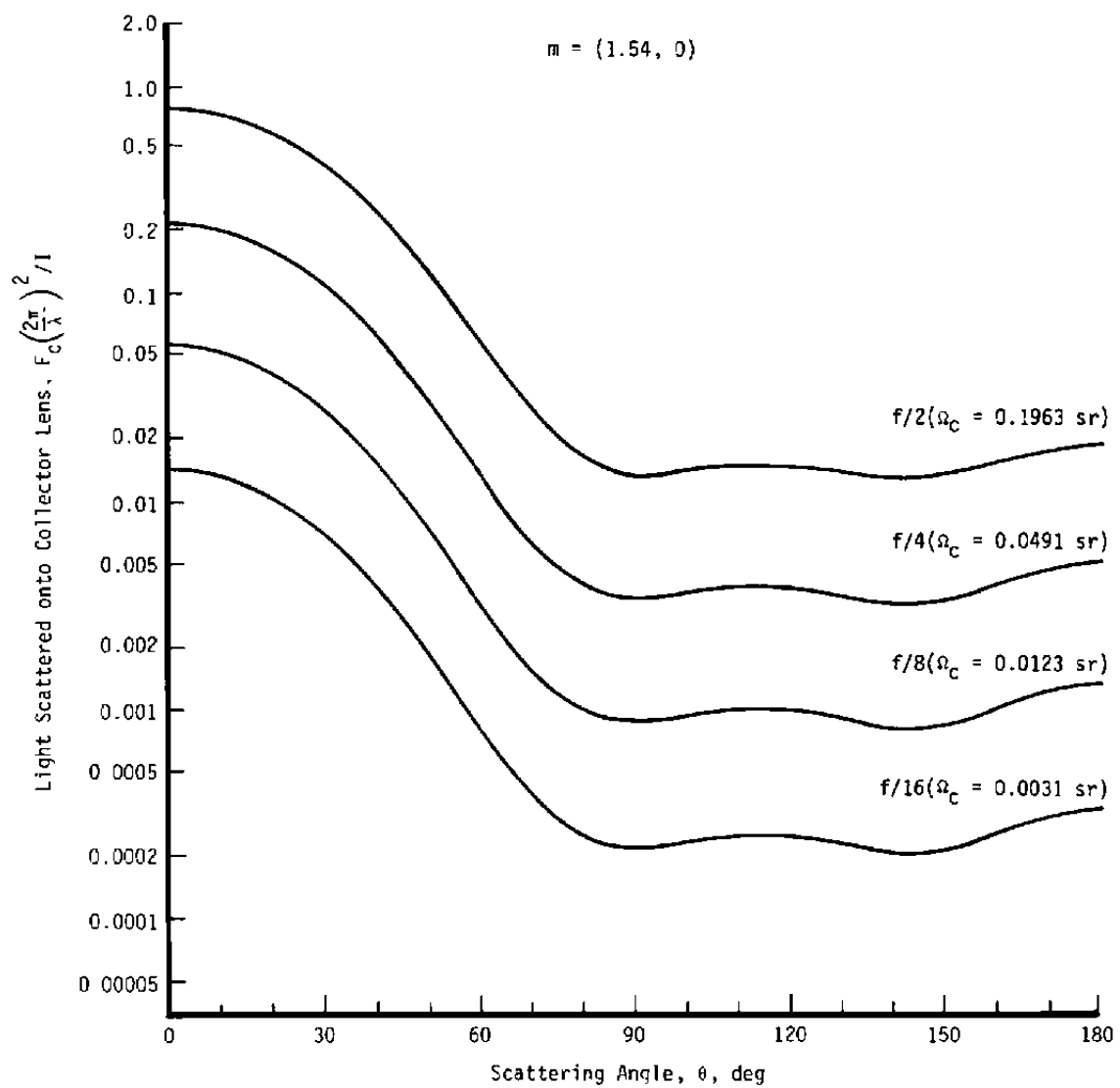


Figure 31. Effect of lens f-number on scattering functions ($\alpha = 3.05$).

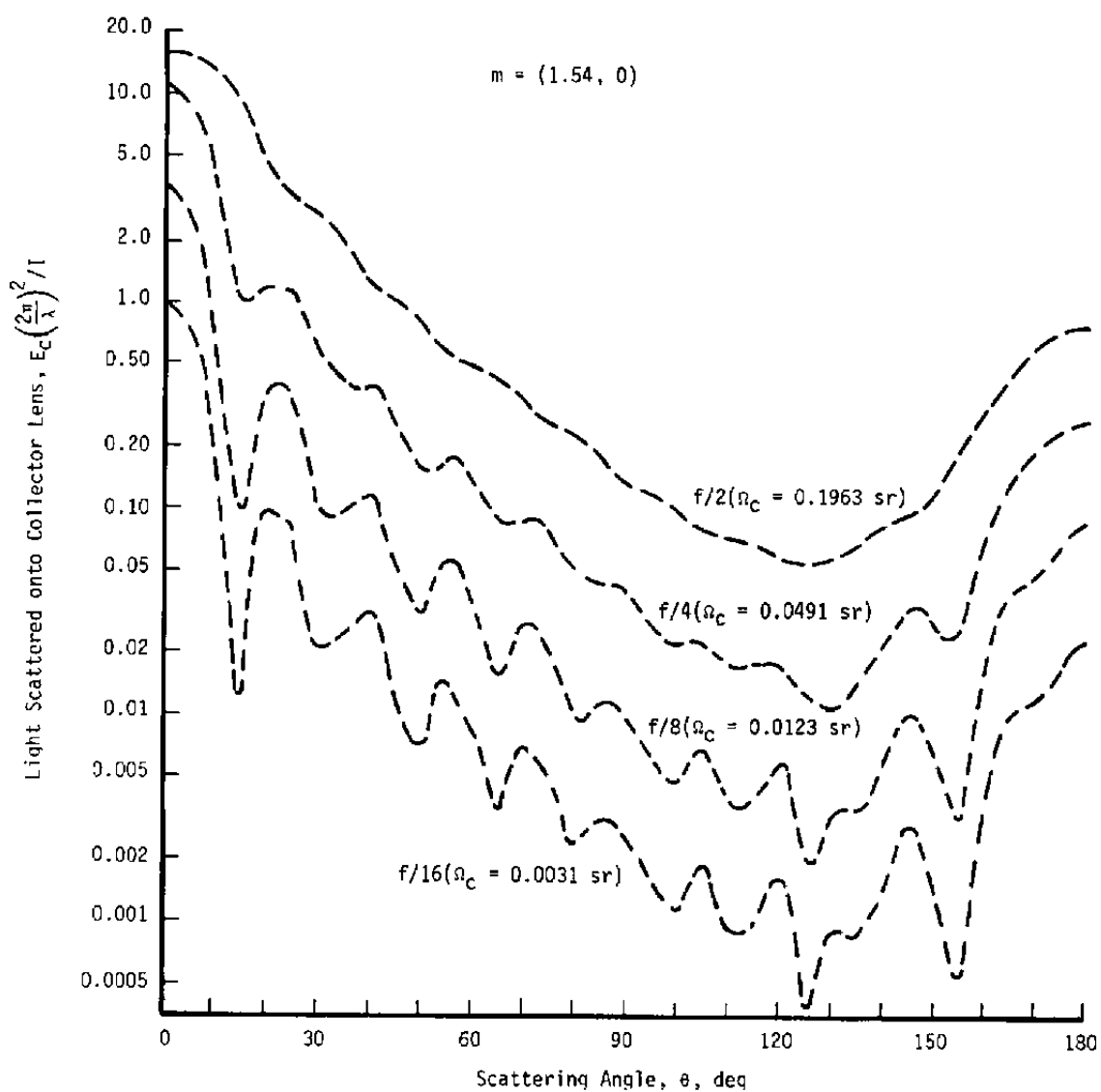


Figure 32. Effect of lens f-number on scattering functions ($a = 12.21$).

The probe volume of a dual-scatter LV system is formed by the intersection of two laser beams which, ideally, are of equal intensity, Gaussian, and similarly polarized. A Cartesian reference frame (X_1 , Y_1 , Z_1) whose origin coincides with the center of the crossover region is depicted in Fig. 33. The bisector of the illuminating beams, which defines the light propagation axis of the LV, is directed along Z_1 , the Y_1 axis is coincident with the detected velocity component, and X_1 is normal to the Y_1 - Z_1 plane. If the angle between the beams, θ , is small, the spatial intensity variation is given by (Ref. 64)

$$\frac{I}{I_0} = \exp \left\{ -\frac{2}{b^2} \left[X_1^2 + Y_1^2 + \left(\frac{Z_1 \theta}{2} \right)^2 \right] \right\} \left\{ \cosh \frac{2Y_1 Z_1 \theta}{b^2} + \cos \frac{2\pi Y_1}{K\delta} \right\} \quad (72)$$

where I_0 is the peak intensity in each of the Gaussian beams of waist radius, b , which form the probe volume. Since only a fraction, η , of the laser power, P_L , actually reaches the probe volume, the peak intensity for a one-component, dual-scatter LV is

$$I_0 = \frac{\eta P_L}{\pi b^2} \quad (73)$$

Although the effective probe volume is limited by the characteristics of the collector optics and data processor, it is useful to define a geometric probe volume bounded by the surface where the signal has exponentially decayed to $1/e^2$ of its most intense value. From Eq. (72), this surface is described by the ellipsoid

$$\left(\frac{X_1}{b} \right)^2 + \left(\frac{Y_1}{b} \right)^2 + \left(\frac{Z_1 \theta}{2b} \right)^2 = 1 \quad (74)$$

Thus b is the semiminor axis of the ellipsoid and

$$a = \frac{2b}{\theta} \quad (75)$$

is its semimajor axis. A set of nondimensional coordinates, ($X_1^* = X_1/b$, $Y_1^* = Y_1/b$, $Z_1^* = Z_1/a$) may be introduced which transform the geometric probe volume to a sphere and allow Eq. (72) to be rewritten as

$$I = \exp \left[-2 (X_1^{*2} + Y_1^{*2} + Z_1^{*2}) \right] \left\{ \cosh 4 Y_1^* Z_1^* + \cos \pi N_1 Y_1^* \right\} \quad (76)$$

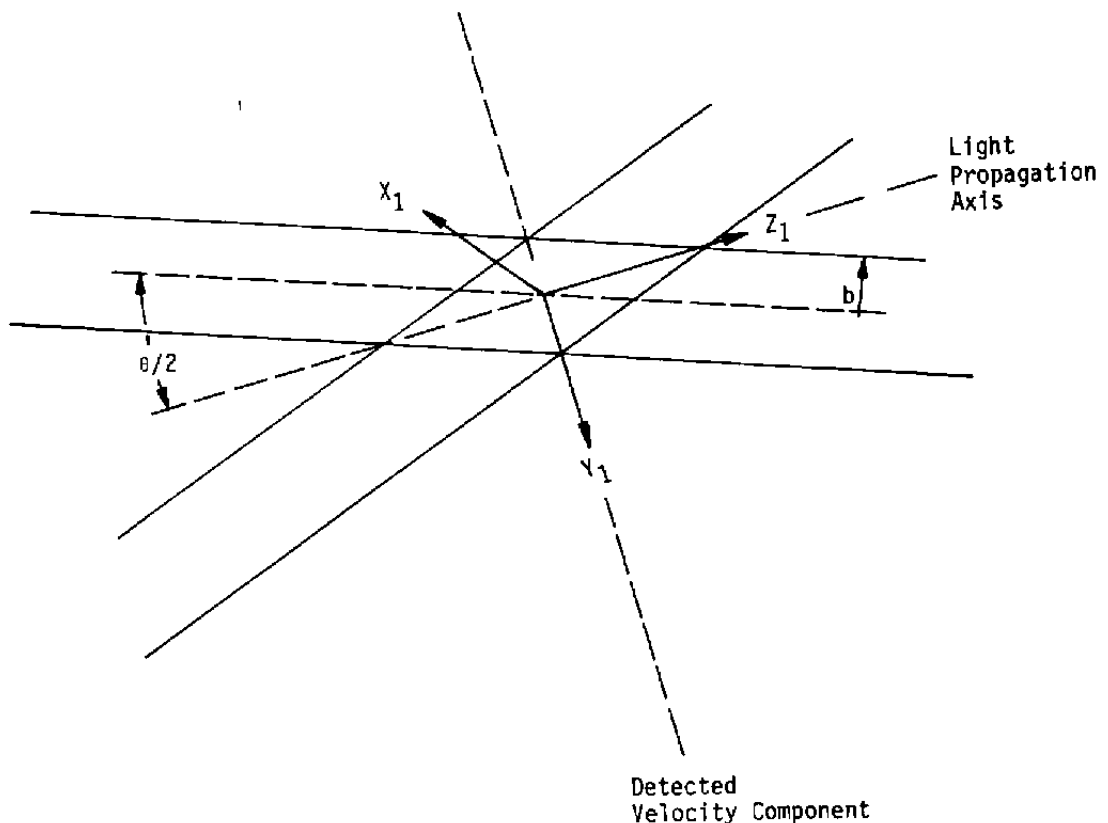
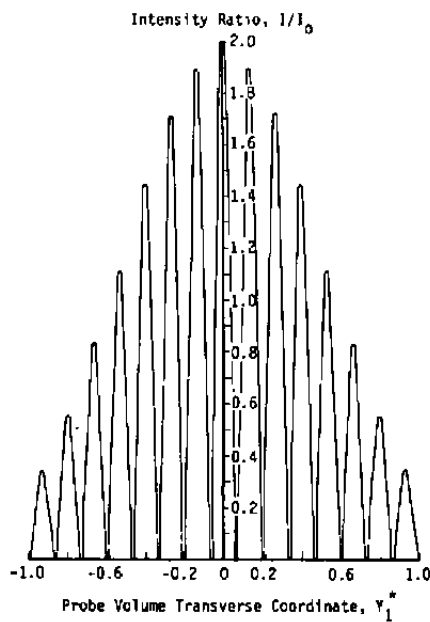
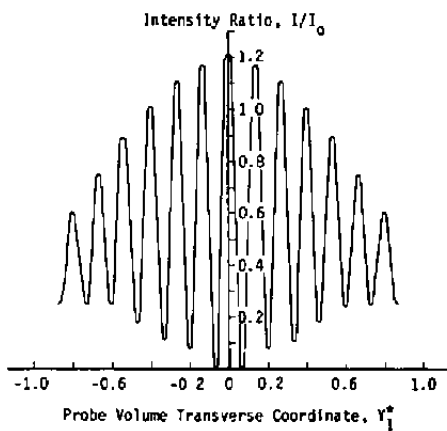


Figure 33. Probe volume coordinate system.

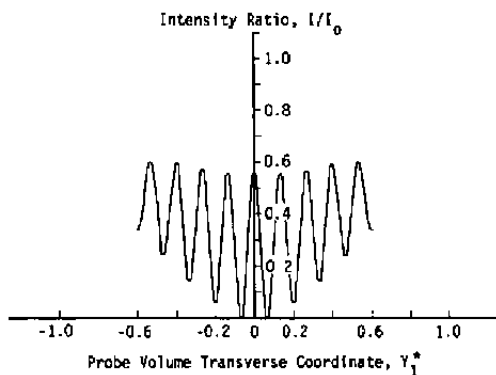
where $I^* = I/I_0$ and $N_f = 2b/K_\delta$ is the number of fringes in the plane $Z_1^* = 0$. The maximum probe volume intensity occurs at the origin of the coordinate system where $I = 2I_0$. The fringe model [Eq. (76)] of the probe volume, however, requires the intensity to approach zero in an alternating fashion as depicted in Fig. 34, where the intensity distribution expected for the LV of Section 2.2.1 is shown at $X_1^* = 0$ for three values of Z_1^* . The maximum Mie scattering amplitude in a dual-scatter system is highly dependent upon the trajectory of the particle as it traverses the probe volume. Even though this dependence does not absolutely preclude discriminating against large particles on the basis of their signal amplitudes, such discrimination can only be accomplished statistically and some large-particle data will generally be present in any data set obtained.



a. $Z_1^* = 0, N_f = 15$



b. $Z_1^* = 0.5, N_f = 15$



c. $Z_1^* = 0.8, N_f = 15$

Figure 34. Intensity variation in the probe volume ($X_1^* = 0$).

To characterize the illuminating intensity without treating the details of the interference pattern along the particle trajectory, several representative illuminating intensities can be defined. The maximum intensity, $I_{\max} = 2I_0$, is clearly one possibility. A second is the average intensity in the probe volume

$$\hat{I} = \frac{3I_0}{4\pi} \iiint_{V_p} I^* dX_1^* dY_1^* dZ_1^* \quad (77)$$

where I^* is defined by Eq. (76). Note, however, that a processable signal will likely result from particles which cross the central portion of the probe volume. For the assumptions that (1) the flow is one-dimensional and (2) the probe volume is small enough that velocity and particle concentration are uniform across it, the probability density function for a particle trajectory along any plane $Z_1^* = \text{constant}$ is

$$f(Z_1^*) = \frac{2}{\pi} \sqrt{1 - Z_1^{*2}} \quad (78)$$

A most probable intensity can then be defined by

$$\langle I \rangle = \frac{2I_0}{\pi} \int_{Z_1^*} \bar{I}^*(Z_1^*) \cdot f(Z_1^*) dZ_1^* \quad (79)$$

where $\bar{I}^*(Z_1^*)$ is the average intensity along the constant Z_1^* planes.

That is,

$$\bar{I}^*(Z_1^*) = \frac{1}{\pi(1 - Z_1^{*2})} \iint_{X_1^* Y_1^*} I^* dX_1^* dY_1^* \quad (80)$$

The above integrations are performed numerically by the subroutine PVIP described in Appendix C. Typical results are presented in Fig. 35, where the variation of \bar{I}^* with the probe volume axial coordinate is shown along with the most probable and average intensities. $\langle I \rangle$ will be approximated as $2I_0/5$. Although $\langle I \rangle$ should provide representative intensities for a dual-scatter LV, in discriminating against large particles the maximum signal amplitude is of primary concern. By assuming each particle

will cross $X_1^* = Y_1^* = 0$ while traversing the probe volume, Eq. (76) reduces to $I_{\max}^* = 2 \exp(-2 Z_1^{*2})$ and a most probable maximum intensity can be defined as

$$\langle I_{\max} \rangle = \frac{4I_o}{\pi} \int_0^1 \exp(-2Z_1^{*2}) \sqrt{1 - Z_1^{*2}} dZ_1^* \quad (81)$$

A numerical integration of Eq. (81) gives $\langle I_{\max} \rangle \approx 2I_o/3$.

The adequacy of these representative illuminating intensities will be discussed in the data comparisons later in this section. By using a single representative intensity, the Mie scattering analysis is simplified and results obtained for one intensity value, I_1 , are readily scaled to another value, I_2 , since, from Eqs. (69) or (70), $E_{c2} = E_{c1} I_2/I_1$. The representative intensities make it possible, moreover, to assess whether the LV used in the bias study can be unambiguously adapted for particle size discrimination. Using $\langle I_{\max} \rangle$, the effect of viewing angle on the scattered light levels is shown for several forward-scatter collection angles in Fig. 36, and backscatter results are given in Fig. 37. For particle diameters up to 10 μm , the theoretical signal amplitudes increase nearly monotonically at several angles in both forward- and backscatter (particularly $\Theta = 40, 60$, and 170 deg). Fortunately, a $\Theta = 170$ deg collector configuration approaches the design condition for the LV and traverse system of Fig. 6.

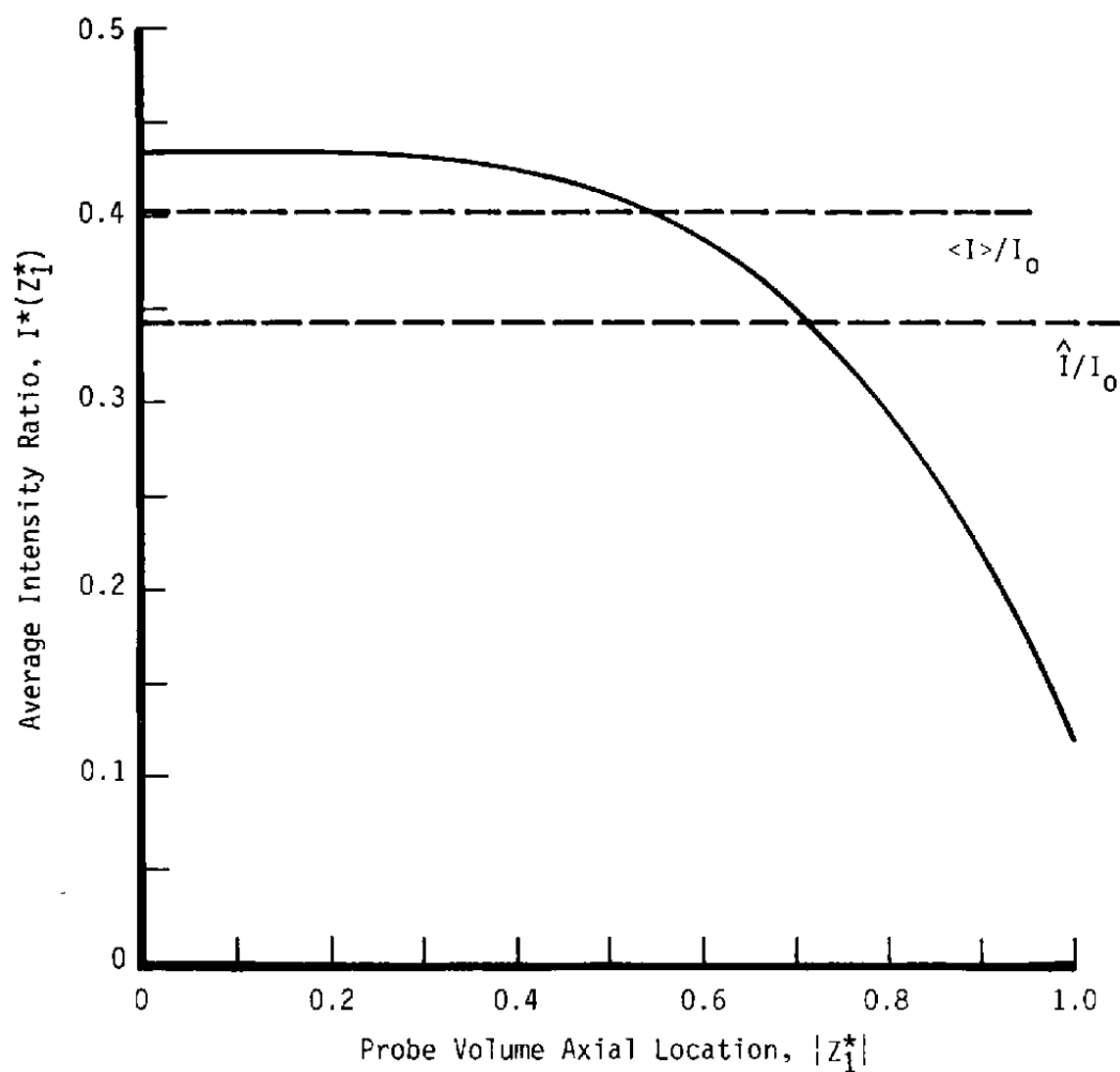


Figure 35. Variation of average illuminating intensity with probe volume location.

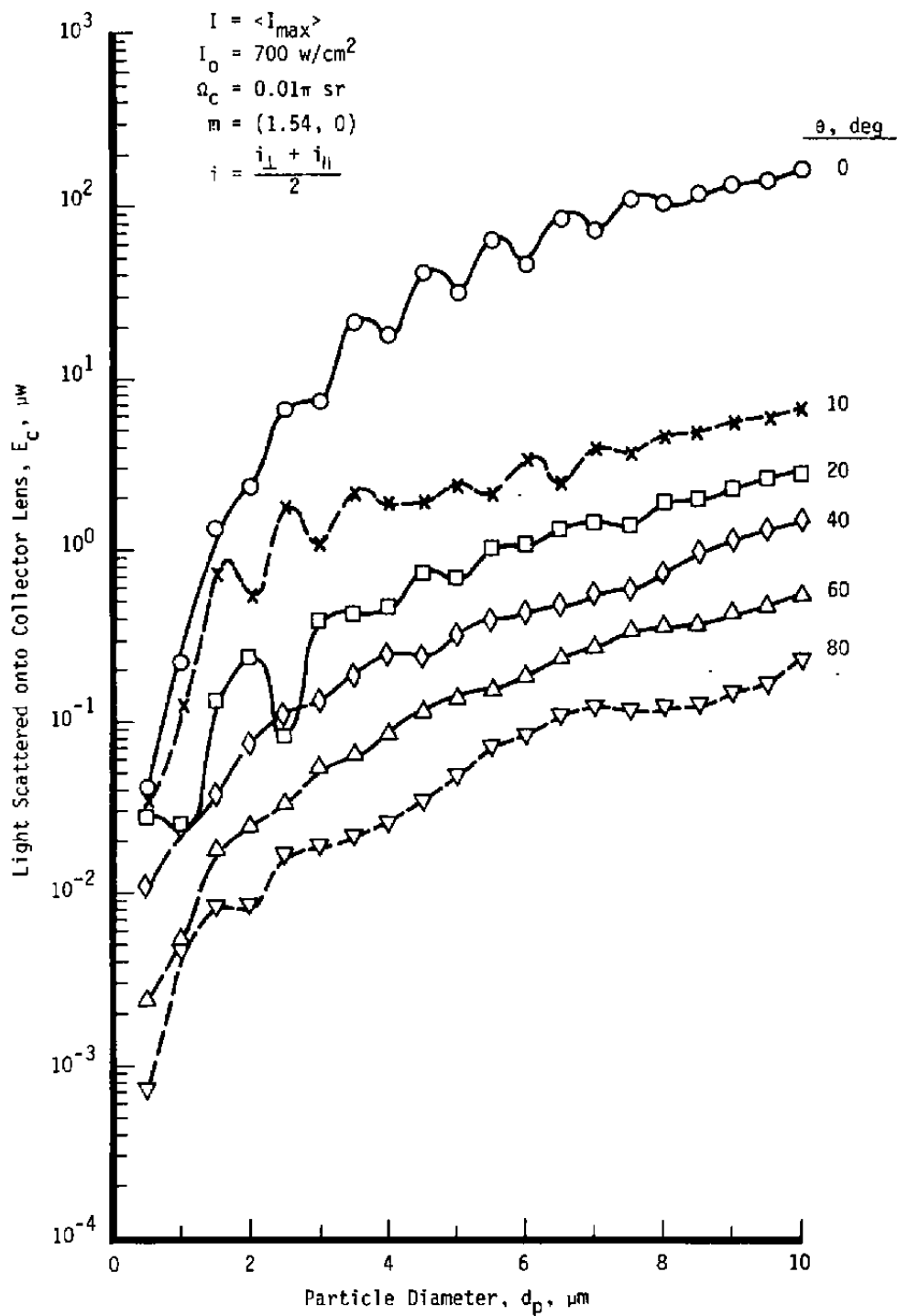


Figure 36. Effect of particle size on light scattered for forward-scatter system.

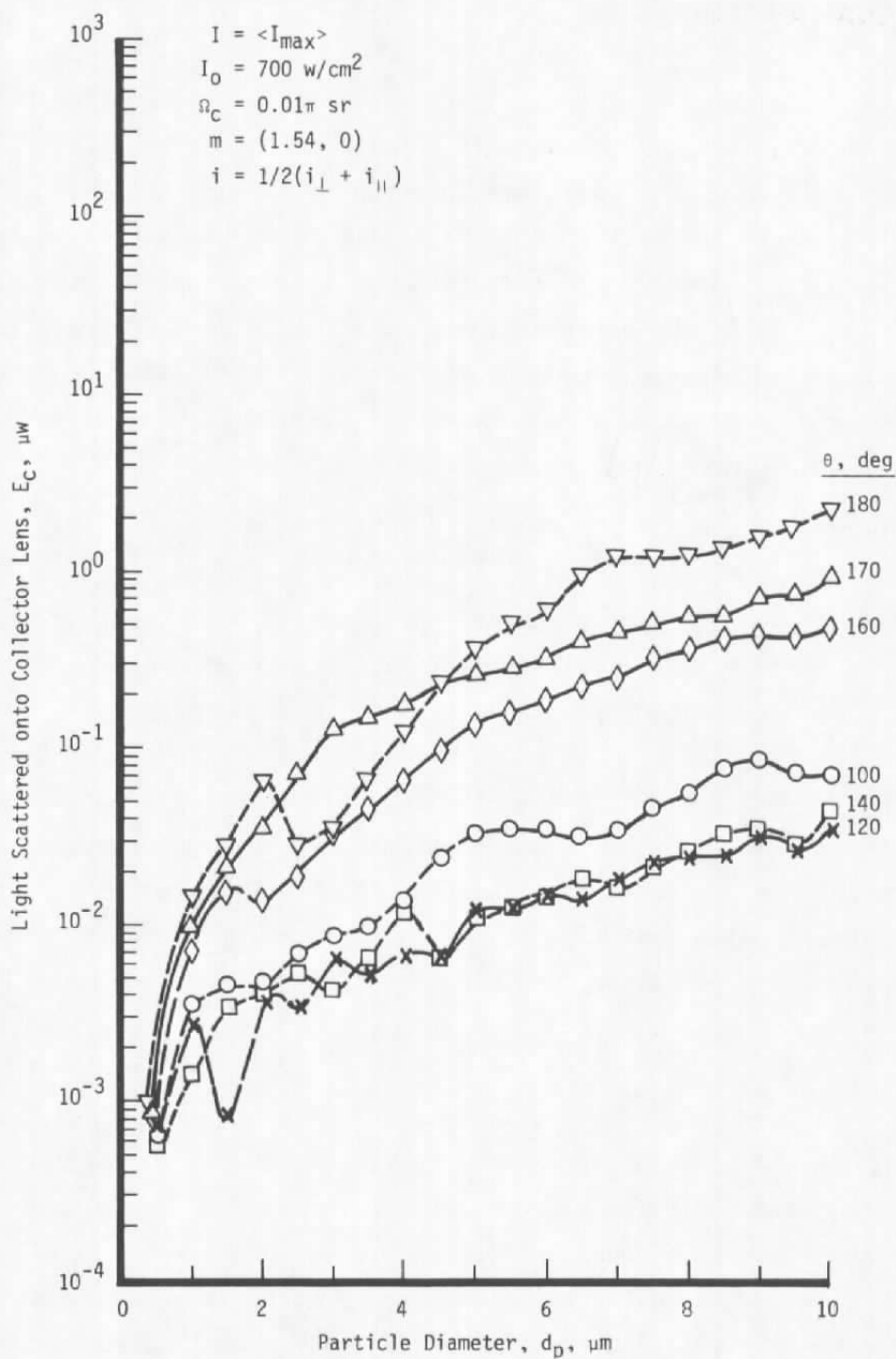


Figure 37. Effect of particle size on light scattered for backscatter system.

3.2 SIGNAL AMPLIFICATION

The theoretical signal levels in Figs. 36 and 37 represent the rate at which scattered light energy is intercepted by the collector optics. To discriminate against particles whose size exceeds a predetermined value requires consideration of the amplitude of the electrical signal at the Doppler data processor (DDP). To proceed from the collected radiation, E_c , to the detected voltage, e_d , consider the amplification and attenuation of the signal by the photomultiplier tube and the LV electronics. For this study, the signal level will be related to collected energy by the linear relation

$$e_d = E_c \left(\prod_{i=1}^M G_i \right) \left(\prod_{j=1}^N T_j \right) \quad (82)$$

where G_i is the ratio of the signal level after amplification to its value entering the i^{th} amplifier and T_j is the corresponding ratio for the j^{th} attenuation process.

For the specific LV being studied, only gains attributable to photomultiplier tube (PMT) amplification need be considered since no other amplifiers were used. Similarly, attenuation was primarily attributable to a laser line filter between the aperture and PMT, as shown in Fig. 1. For the 30-Å bandwidth filter used, the transmission ratio at $\lambda = 0.5145 \text{ } \mu\text{m}$ was $T_1 = 0.765$.

A photomultiplier converts incident radiation into electrical energy by a photoemission process and then amplifies the signal by means of secondary emission. The elements of a typical tube may be regarded as (1) a semitransparent photocathode, which emits electrons because of interaction of the incident radiant energy with electrons in the photocathode material, (2) several dynode stages, in which secondary emission results from the impact of electrons on the dynode surface, and (3) an anode, which collects the electrons emitted in the last dynode stage

and provides the output current for the PMT. Although photomultiplier tubes can be analyzed in detail by quantum statistical techniques, in the present application a PMT will be regarded simply as a linear device characterized by a transfer function H_G so that

$$i_A = H_G E_i T_1 \quad (83)$$

The gain attributable to the PMT is, then

$$G_1 = i_A R_e / E_i T_1 \quad (84)$$

where R_e is the LV electronics circuit resistance. The gain associated with a particular photomultiplier is, however, limited by its supply voltage, e_s , and dynode voltage divider circuitry. Typically, H_G for various tubes may range from 10 to 10^6 ma/ μ w by proper tube choice the LV signals can be amplified to a detectable level. A serious concern for discrimination studies is the observed variation in gain for particular tube types under ostensibly similar conditions. Variations in amplification levels ranging over two orders of magnitude have been observed (Ref. 65). Consequently, discriminating against particles on the basis of signal amplitude must be based on calibration of the PMT system used rather than on manufacturer's specifications.

Such calibrations were performed for several photomultipliers using the arrangement illustrated in Fig. 38. In this calibration a partially transmitting mirror is placed at the center of the probe volume so that an essentially steady anode current results. Note that the laser radiation from the illuminating optics must be attenuated to prevent damage to the PMT. Then, by choosing an appropriate resistance, a voltage level can be read on either a digital voltmeter or an oscilloscope. The illuminating intensity was varied by changing the neutral density filters used to attenuate the laser radiation and/or adjusting the laser power. After each series of measurements the PMT was replaced by a calibrated laser power meter so that the illuminating intensity could be measured.

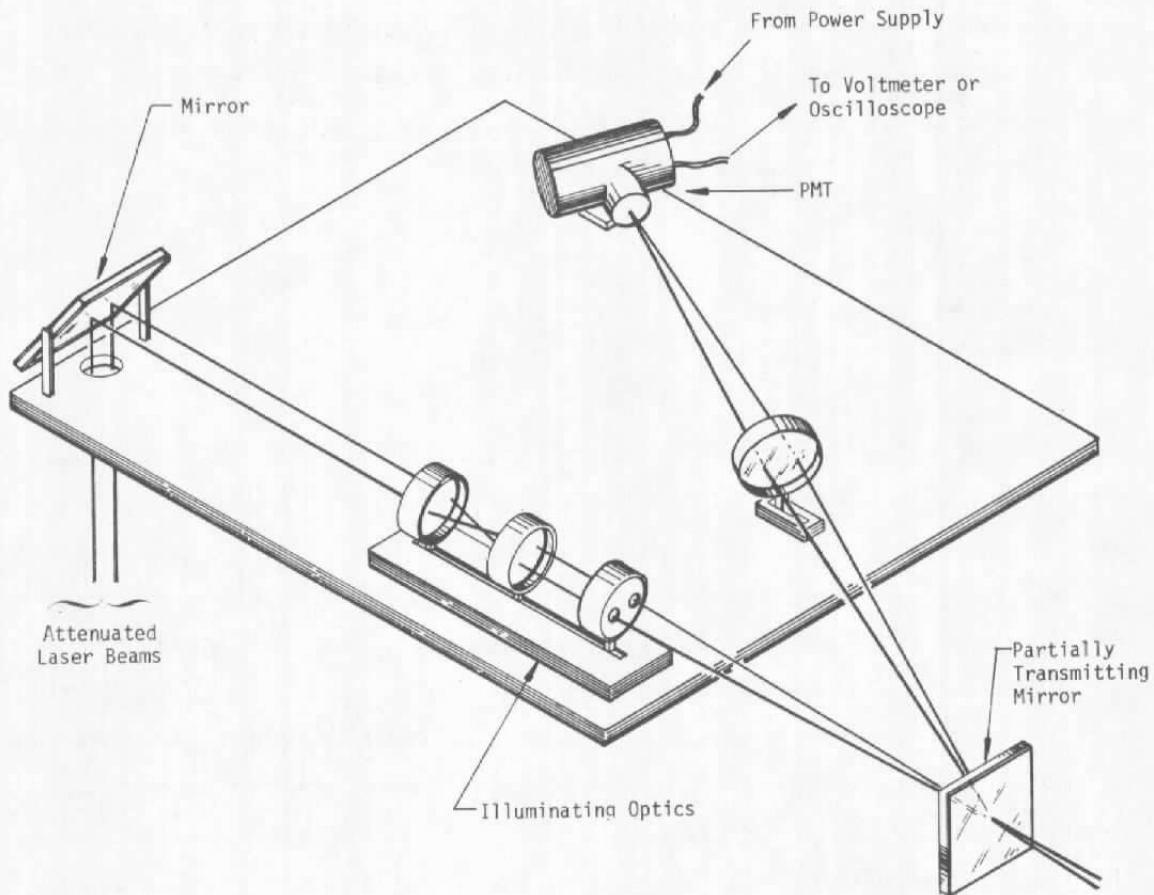


Figure 38. PMT calibration arrangement.

Typical calibration curves for an RCA 931A PMT coupled with a voltage divider circuit, which limited the anode current to about 1 ma, are shown for various supply voltages in Fig. 39. If the amplification function is defined as

$$H_G = \frac{1}{T_1} \left| \frac{\partial i_A}{\partial E_c} \right|_{E_c=0} \quad (85)$$

the variation of H_G with supply voltage can be determined. A comparison of the experimental values with the manufacturer's data (Ref. 65) is made in Fig. 40 and emphasizes the importance of calibration of the particular tube in adequately predicting signal amplitude. Also apparent in Fig. 39, the anode current varies nonlinearly with

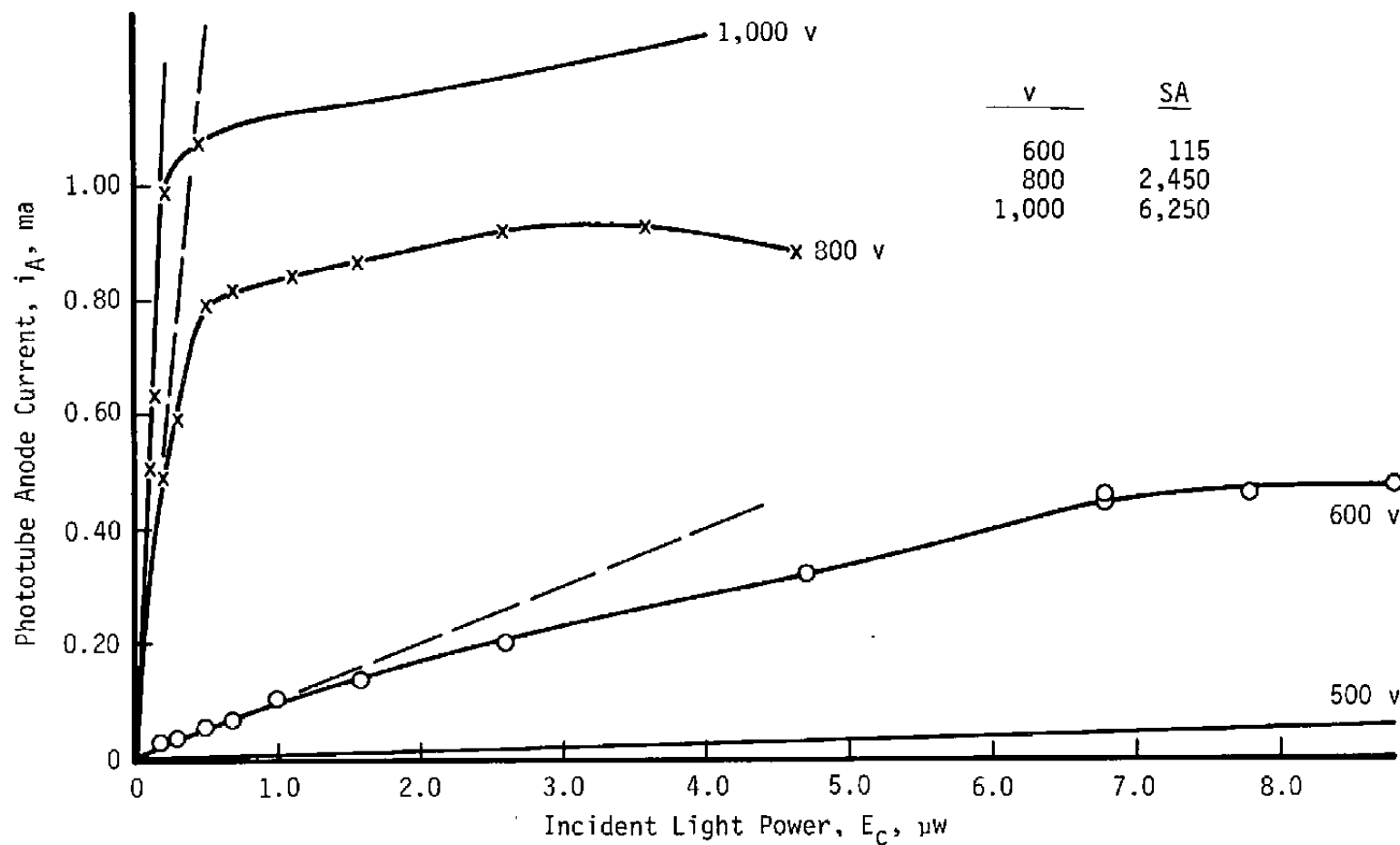


Figure 39. PMT amplification for several power supply voltages.

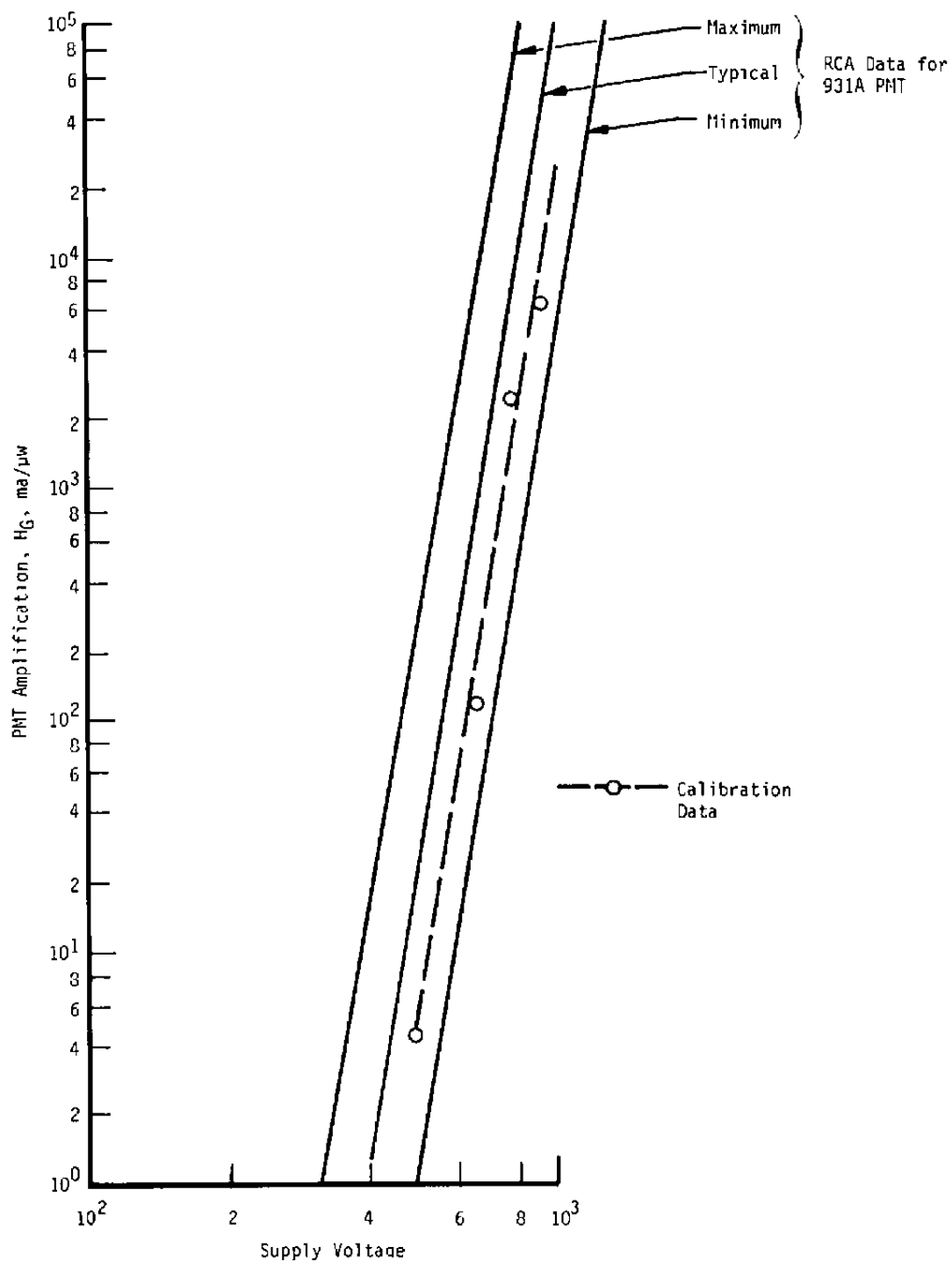


Figure 40. Effect of supply voltage on PMT current amplification.

illuminating intensity once PMT saturation is approached. Therefore, the level of the scattered light must be limited if the linear relation proposed in Eq. (83) is to hold. The observed illuminating intensity needed to produce saturation of the PMT is shown in Fig. 41 as a function of supply voltage. Note that these results apply to a particular PMT and cannot be generalized to include all PMT's of this type.

3.3 EXPERIMENTAL SIGNAL LEVELS

As proposed in Section 3.1, the Mie scattering characteristics of particles traversing the probe volume of a dual-scatter LV were estimated by considering the intersecting beams as a single beam at some equivalent illuminating intensity. The most probable intensity, $\langle I \rangle$ [Eq. (79)], was used to obtain representative signal amplitudes, and the maximum amplitude of the signal was determined from the probability weighted maximum intensity, $\langle I_{\max} \rangle$ (Eq. 81). The adequacy of these equivalent intensities was checked by experimentally determining LV signal amplitudes for monodisperse, spherical particles of various sizes. The confined jet described in Section 2.2 provided a flow free of intrinsic particles for nominal exit velocities of $U_0 = 15$ and 30.5 m/sec. A Berglund-Liu aerosol generator (Ref. 40) provided spherical, oleic acid particles having diameters of either $d_p = 2.0, 5.0, \text{ or } 10.0$ μm . Microscopic sizing of collected samples verified that the particles were essentially spherical and were uniformly of the nominal diameters. Signals were generated by the Bragg-diffracted LV operated in a one-component mode at a collector lens position of $\Theta = 168.4$ deg. At this collector angle, stray reflections from the cell and optical components were negligible, and the laser line filter described earlier eliminated signals from radiation sources having wavelengths other than $\lambda = 0.5145$ μm . PMT calibrations showed that the photomultiplier transfer function, H_G , was 4×10^4 ma/ μw and no other signal amplification was used. The PMT anode signal was terminated with an $R_e = 50$ -ohm impedance, and laser power was varied with particle size to ensure that PMT saturation current was not approached.

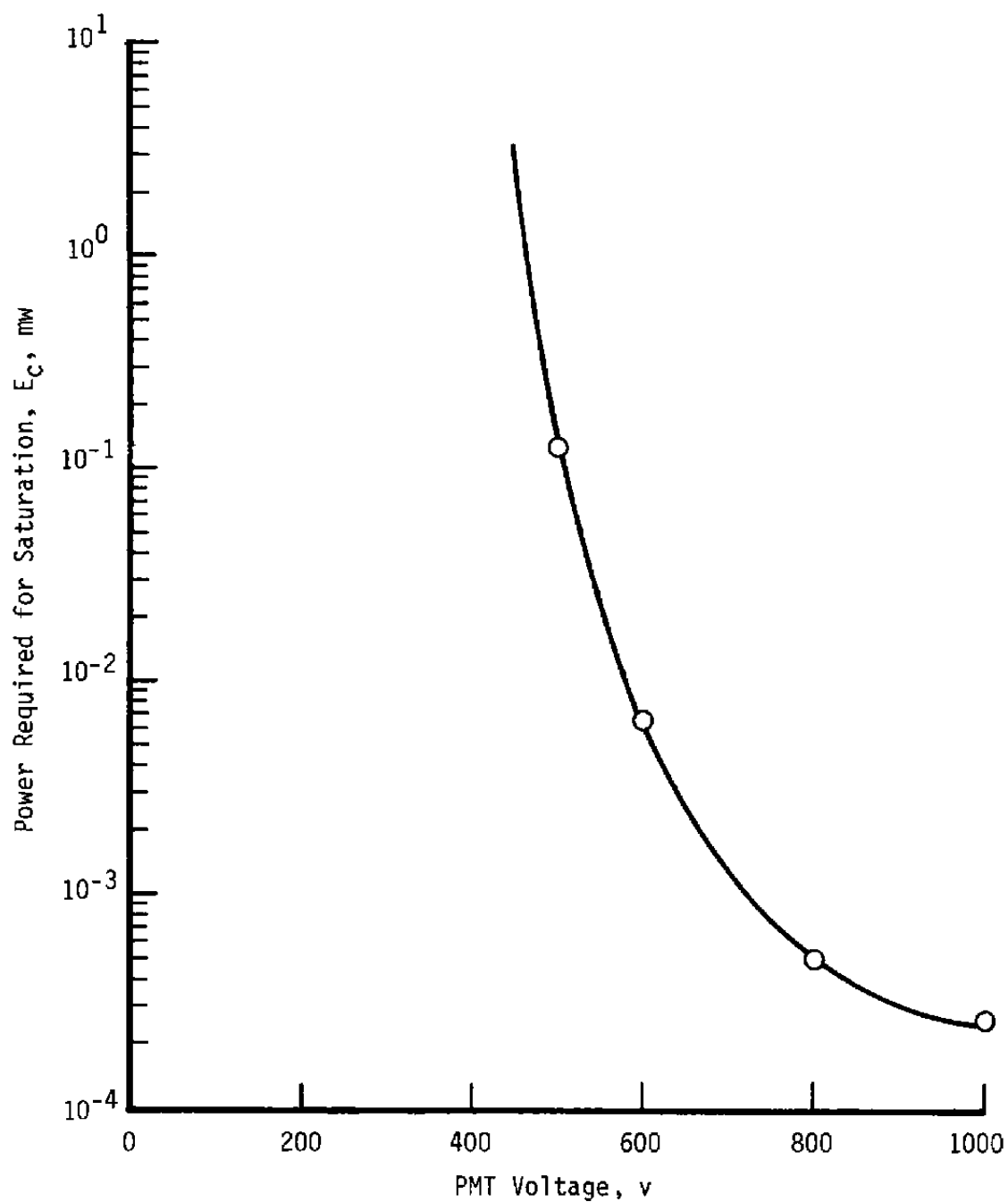


Figure 41. PMT saturation levels.

To determine the maximum amplitude of signals generated by particles traversing the probe volume, the oscilloscope trigger was calibrated using a pulse generator with output signals of known amplitude and a given repetition rate. This signal was input to the oscilloscope, and a frequency counter counted the oscilloscope trigger pulses that resulted when the calibration signal exceeded the trigger level. The oscilloscope trigger was set at a level that decreased the trigger pulse rate to half the pulse generator output rate so that the generator output amplitude provided a precise setting of the voltage level at which the oscilloscope would trigger. The PMT signal was then input to the oscilloscope and sample rate measured by the frequency counter. Data were taken in four 10-sec intervals to obtain the mean data rate over a 40-sec interval. The process was then repeated to obtain the sample rate at successively higher trigger levels. Although the trigger could be calibrated in 2-mv intervals, 10-mv steps were used.

For the PMT and voltage divider used, anode saturation was approached near a signal level of 50 mv. Consequently, the laser power was decreased as the particle size increased to avoid the nonlinear PMT amplification observed (Fig. 39) near PMT saturation. Since the available amplifiers caused serious signal distortion and inversion, the unamplified, low PMT signal levels were used. At these low signal levels, random low-level noise signals were detected at trigger levels below 9 mv. This was evidenced by observed data rates that far exceeded the ability of the seeder to deliver particles to the probe volume. Therefore, detection was limited to signals having amplitudes greater than 10 mv, and the number of particle signals below that level were estimated by the difference between the observed and expected events.

Despite this limitation, remarkably consistent results were obtained in all tests. Figure 42 shows these results in a histogram of oscilloscope sampling probabilities corresponding to each trigger setting. The typical

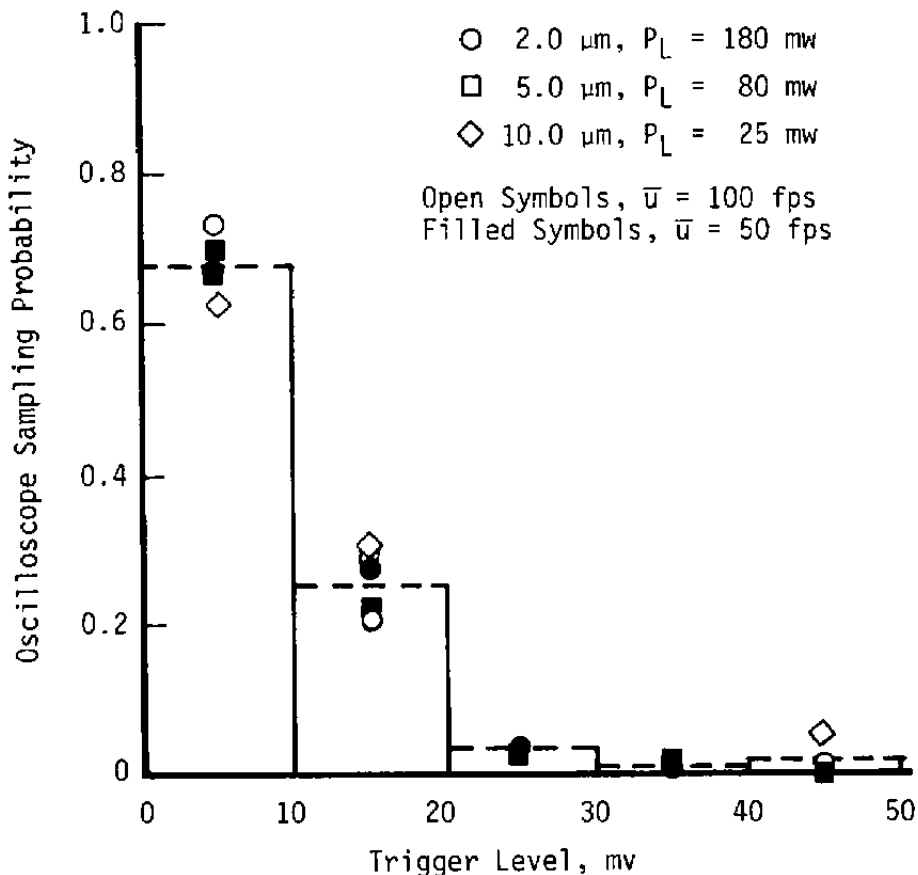


Figure 42. Histogram of oleic acid signal amplitudes.

signal level should be between 10.7 and 13.3 mv in each case, as indicated using the computer model MIELV with an illuminating intensity taken as the peak single line intensity, I_o , for each laser power used. Since Fig. 42 shows that the most probable signal levels are below 10 mv, I_o is too high a value to be used for the illuminating intensity in MIELV calculations. Fortunately, the signal level, e_d , is a linear function of the collected energy, E_c , and thus, in turn, a linear function of the illuminating intensity, so the MIELV predicted signal levels will agree with the most probable observed signal levels if the illuminating intensity is taken as $I_o/2$ to $3I_o/4$. This compares favorably with the value $\langle I_{\max} \rangle = 0.67 I_o$ predicted by Eq. (81). With the uncertainty in the experiments, however, this result can only be taken as evidence that with adequate calibration

the single-beam model of an LV can produce signal amplitudes that are representative of experimental results. Therefore, program MIELV was used to assess the feasibility of sizing or discriminating against particles on the basis of LV signal levels.

3.4 PARTICLE SIZING AND DISCRIMINATION

Figure 43 shows the variation in theoretical signal amplitude for the LV used in these studies at a collector angle of $\theta = 168.4$ deg and an illuminating intensity corresponding to a laser power of $P_L = 150$ mw. The particles are assumed to be oleic acid in air. For particle diameters up to $2.0 \mu\text{m}$ the signal level is a monotonically increasing function of particle size. The decrease in signal level for particles slightly greater than $2.0 \mu\text{m}$, however, limits the useful range for sizing studies to $d_p \leq 1.8 \mu\text{m}$. Therefore, if the signals were suitably amplified the present LV could size oleic acid particles in the range $0.5 \leq d_p \leq 1.8 \mu\text{m}$. The lower limit is set by the noise associated with the system. For $d_p \geq 2.0 \mu\text{m}$, however, the variations in signal levels with changes in particle size would only permit gross size determinations. That is, while a $2\text{-}\mu\text{m}$ particle could be distinguished from one whose diameter was $5 \mu\text{m}$, it would not be possible to distinguish between 3.0- and $3.8\text{-}\mu\text{m}$ particles. It should be noted that it is the particle size parameter, $\alpha = \pi d_p / \lambda$, that actually determines the extent of the region where monotonic increases in signal amplitudes are expected. Therefore, if the LV system used a laser which radiated in the infrared the useful sizing range could be extended as noted in Ref. 35. Specifically, for a wavelength, λ , of $10 \mu\text{m}$ the monotonic range would extend to $d_p \leq 34 \mu\text{m}$ if all other LV system parameters could be maintained.

Although the use of signal amplitudes for particle sizing is limited to specific size range, the use of signal amplitudes for size discrimination is feasible. For the conditions applicable to Fig. 43, discriminating against all signals whose amplitudes exceed $e_d = 8$ mv would exclude all

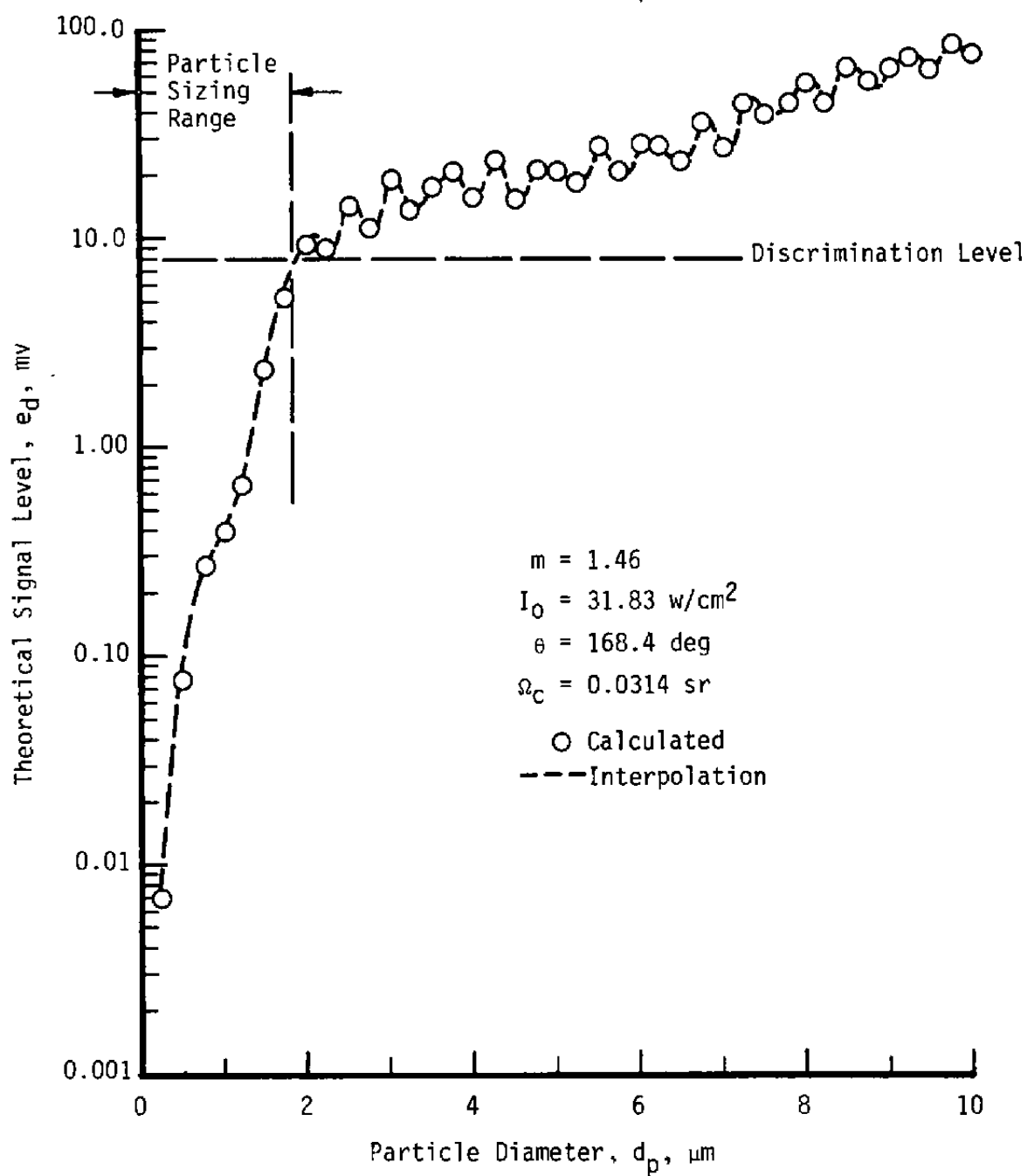


Figure 43. Effect of particle size on signal amplitude.

particles having diameters greater than $2.0 \mu\text{m}$. The variation in signal level with laser power or, equivalently, illuminating intensity is shown in Fig. 44. For a laser power of 300 mw, constraining the LV to process signals of amplitudes less than $e_d = 30 \text{ mw}$ would eliminate particles with diameters greater than $3.25 \mu\text{m}$ (as well as some particles with diameters slightly less than $3.25 \mu\text{m}$). The figure illustrates, moreover, the effect of setting a lower threshold level either deliberately or because of processor limitations or the presence of low-level noise. For the above example no particle below $d_p = 1.75 \mu\text{m}$ could be detected, although this situation could be remedied by introducing suitable amplification after the PMT. In this regard, an amplifier with a gain of 10 would allow detection of $1\text{-}\mu\text{m}$ particles and cause the signals below 30 mv to fall within the monotonic range of Fig. 43, thereby eliminating ambiguities in discrimination limits.

The concept of discriminating against large particles is, perhaps, of most interest in a flow where several types of particles are present. Such a flow would commonly occur when artificial seeding is used to enhance data rates or control the intrinsic particle characteristics. The range of amplitudes expected for air containing natural particles ($m = 1.54$), Ref. 63, aluminum oxide seed particles ($m = 1.72$), and water droplets ($m = 1.33$) is shown in Fig. 45. The observations made on the possibility of sizing particles apply in each of these cases as well, although the region where the amplitude function exhibits monotonic behavior is a strong function of refractive index. Specifically, for water droplets the range for which sizing is possible is $d_p \leq 1.5 \mu\text{m}$, whereas for either Al_2O_3 or intrinsic scatters the limit is approximately $d_p \leq 0.8 \mu\text{m}$. In Fig. 46, these data are replotted for various illuminating intensities. Again the LV can be constrained to exclude signals from large particles. However, low-level discrimination as well as an upper limit must be used if some large-particle signals (H_2O , $d_p \approx 3.0$) are to be eliminated from consideration.

Oleic Acid, $m = (1.46, 0)$

$$H_G = 4 \times 10^4 \frac{\text{ma}}{\text{uW}}$$

$\theta = 168.4 \text{ deg}$

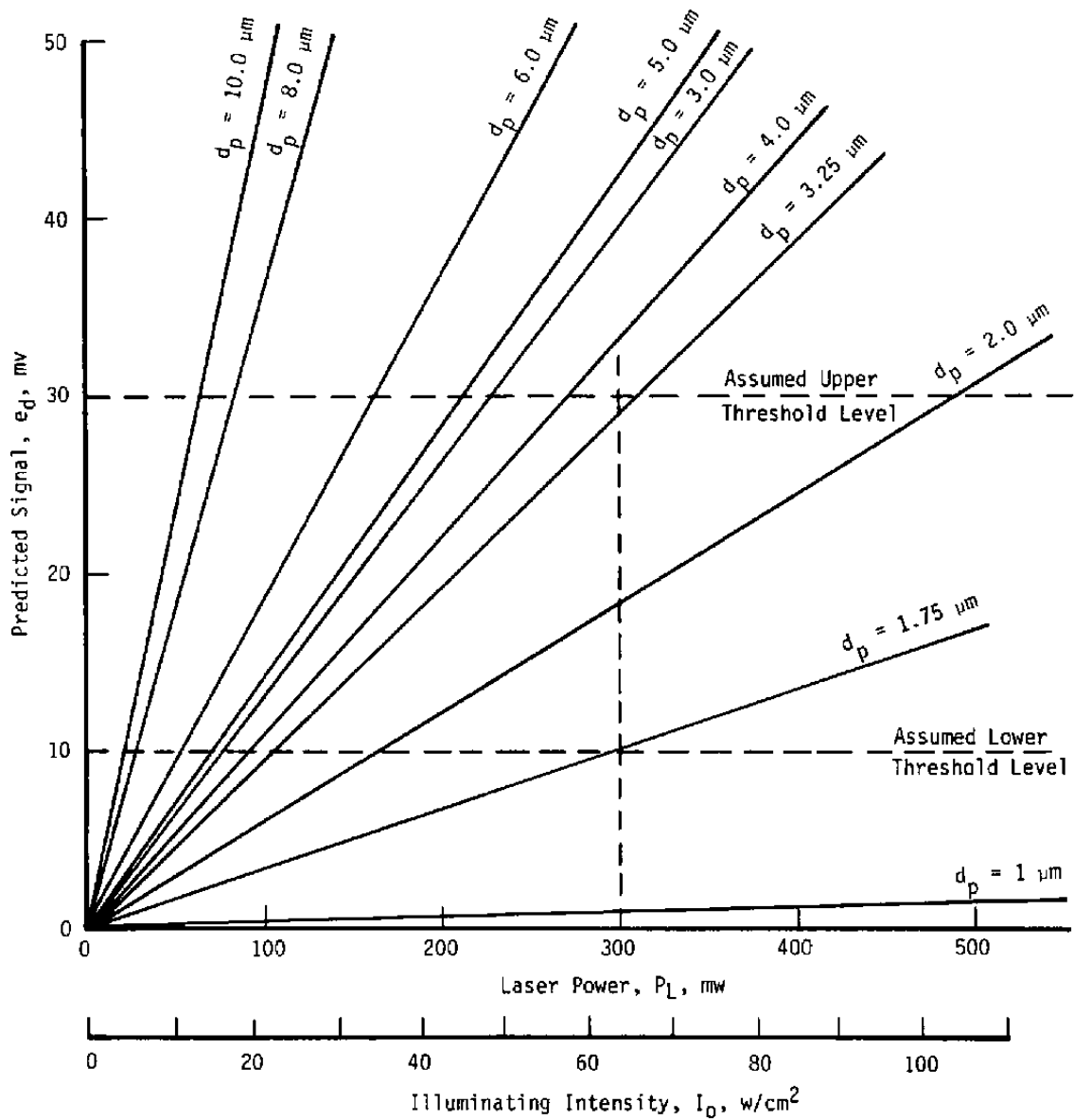


Figure 44. Signal level variation with illuminating intensity.

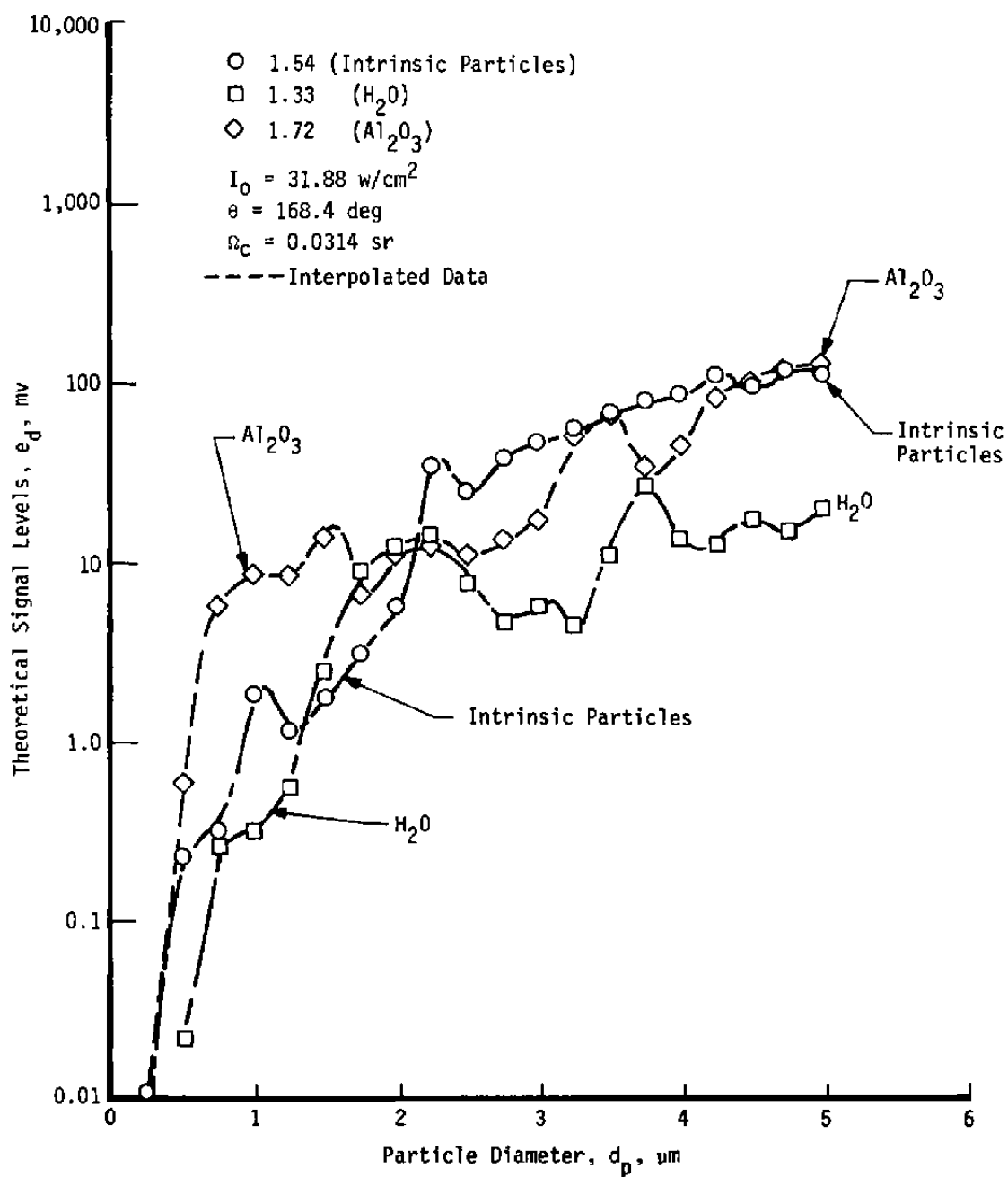


Figure 45. Signal amplitude variation with size for several particulates.

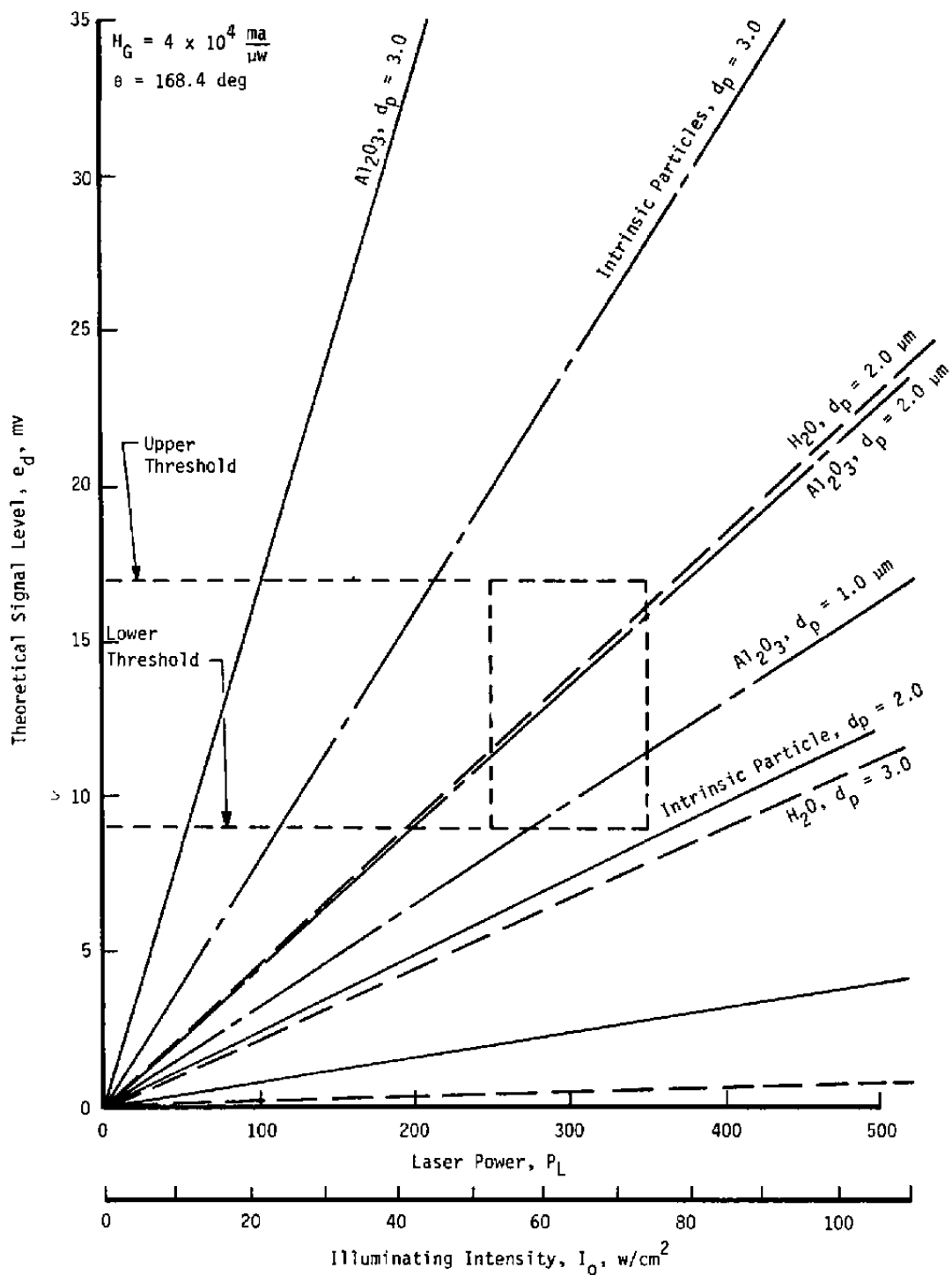


Figure 46. Effect of illuminating intensity on signal amplitudes for several particulates.

In summary, the use of the Mie scattering amplitude of LV signals to size particles implies a degree of control over the experiment that is not always practical. Specifically, use of an LV for this purpose requires:

1. the freedom to choose an optimum collector angle and collector lens so that a monotonic amplitude function can be obtained,
2. knowledge of the refractive index of the particles,
3. calibration of PMT amplification characteristics,
4. choice of laser power to keep the PMT from saturation yet provide adequate S/N ratios for velocity measurement, and
5. low-noise levels in electronic signals.

While some of these constraints may be relaxed in discriminating against large particles, some knowledge of signal amplitude versus particle size must be obtained by calibration or calculation to set the discriminator voltage properly. Furthermore, in a seeded flow with intrinsic particles a low-level discriminator may also be needed to eliminate some large-particle signals. In addition, the results are extremely sensitive to each of the parameters characterizing the Mie scattering process. As a result, extrapolating results to condition that differ even slightly from those considered theoretically or observed experimentally is unreliable. Finally, it must be realized that particle sizing or discrimination from signal amplitudes can only be accomplished in a statistical sense since detailed knowledge of where each particle crosses the probe volume is unattainable.

4.0 CONCLUSIONS

Analytical and experimental studies were performed to determine (1) whether statistical bias in the mean and central moments of velocity determined from individual realization laser velocimeter (IRLV) measurements is a significant source of error and (2) whether the maximum amplitude of LV burst signals could be used to size particles or discriminate against signals from large particles. Both problems are important in the interpretation of LV measurements since affirmative answers to either question could alter both the course of Doppler data processor (DDP) development and the experimental procedures and data reduction techniques used in LV-supported test programs.

The analytical studies of statistical bias showed that, for a bias to exist in IRLV data, the fluid velocity fluctuations and the times between particle arrivals must be correlated. While the sampling mechanisms peculiar to IRLV utilization predict such correlations, it was shown by both limiting statistical arguments and a bias simulation computer program that the correlation function is altered by (1) three-dimensional velocity fluctuations, (2) fluctuations in particle concentration, and (3) data acquisition rate limitations imposed by the DDP and data acquisition systems. The simulation program showed, moreover, that various bias-correcting algorithms proposed for improving IRLV averages in statistically biased situations are effective only at high data rates (in excess of two samples per integral time scale) and might fail at low data rates.

In the experimental program, mean velocities and turbulence intensities in the near field of a subsonic jet were determined (as applicable from pitot pressures, a hot-wire anemometer, and an IRLV system). Although care was taken to produce conditions favorable to the attainment of biased results, no consistent experimental evidence

of bias was found. Furthermore, random selection of the data produced results which were nearly identical to those obtained from the original data sets. Consequently, the velocity-arrival time correlation necessary for obtaining bias was negligible and no bias occurred.

In conclusion, (1) statistical bias is not present in all IRLV data, (2) routine correction for bias can produce serious errors, and (3) modification of DDP's to incorporate bias-correcting algorithms or circuitry is not always warranted. Since random sampling can be readily accomplished using standard computer subroutines, data reduction procedures should include a check for bias using random selection of the recorded data sets. Bias-correcting algorithms should be used only if this technique shows significant bias. Numerical random selection should not be used, however, to correct for bias.

To study the ability of signal amplitude to discriminate particle size, a computer program was developed to (1) determine the Mie scattering amplitudes of signals from particles traversing the probe volume of a dual-scatter LV and (2) compute the signal level expected at the data processor after amplification and attenuation of the scattered signal by the system. For simplicity, the program (MIELV) assumed that the illuminating intensity in the probe volume of a dual-scatter LV system was equivalent to a single-beam intensity determined in an auxiliary program (PVIP).

Experiments were performed to validate the equivalent beam assumption and to ascertain how closely typical photomultiplier tubes correspond to manufacturer's specifications. It was determined that using an equivalent intensity qualitatively gives signal levels that conform to those experimentally observed. Photomultiplier calibrations, however, showed an order of magnitude variation in the amplification obtained with different tubes. For this reason, any sizing or discrimination study must be performed with an accurately calibrated tube.

Based on the results of these experiments, (1) the wide variation in signal levels with particle size, index of refraction, and collector optics design makes it imperative that sizing or discrimination studies be supported with detailed Mie scattering calibrations, (2) the predicted LV signal amplitudes depend upon the particle trajectory through the probe volume so that particle identification can only be performed statistically or by restricting the collector optics to view only a portion of the probe volume, (3) particle sizing is possible only for a limited range of sizes or at particular collector optics scattering angles, (4) the effective sizing range increases linearly with wavelength and can, therefore, be extended by utilizing IR light sources, and (5) discrimination against large particles can be achieved qualitatively even in flows containing several types of particles.

Future DDP's should have low- and high-level discriminators to identify or eliminate signals from large particles during signal processing. The computer programs developed during the study, moreover, should be valuable in the design of LV systems for applications differing appreciably from those considered in this study. Finally, while beyond the scope of this study, the single-beam assumption is not essential to the MIELV program and should be removed in future program developments.

REFERENCES

1. Barnett, D. O. and Giel, T. V., Jr. "Application of a Two-Component Bragg-Diffracted Laser Velocimeter to Turbulent Measurements in a Subsonic Jet." AEDC-TR-76-36 (AD-A025355), May 1976.
2. Barnett, D. O. and Giel, T. V., Jr. "Laser Velocimeter Measurements in Moderately Heated Jet Flows." AEDC-TR-76-156 (AD-A038283), April 1977.

3. Chriss, D. E. "An Experimental Investigation of Ducted, Reactive, Turbulent Jet Mixing with Recirculation." Presented at the 14th JANNAF Combustion Meeting, United States Air Force Academy, August 15-19, 1977.
4. Smith, G. D. and Giel, T. V., Jr. "Two-Component Laser Velocimeter Measurements in a Dump Combustor Flow Field." Proceedings of the Third International Workshop on Laser Velocimetry, Purdue University, July 1978.
5. Barnett, D. O. and Brayton, D. B. "Laser Velocimeter Utilization in Jet Engine Altitude Test Cells." AEDC-TR-77-21 (AD-A041019), June 1977.
6. Barnett, D. O. and Giel, T. V., Jr. "Application of a Two-Component, Bragg-Diffracted LV to Turbulence Parameter Determination and Isothermal, Subsonic Jet." Minnesota Symposium on Laser Anemometry, University of Minnesota, Minneapolis, Minnesota, October, 1975, pp. 146-183.
7. Goethert, W. "Balanced Detection for the Dual-Scatter Laser Doppler Velocimeter." AEDC-TR-71-70 (AD722093), June 1971.
8. Cline, V. A. and Lo, C. F. "Application of Dual-Scatter Laser Velocimeter in Transonic Flow Research." AGARD-CP-193, Applications of Non-Intrusive Instrumentation in Fluid Flow Research, Saint Louis, France, May 1976, pp. 4-1 to 4-12.
9. Lennert, A. E., Brayton, D. B., and Crosswy, F. L. "Summary Report of the Development of a Laser Velocimeter to Be Used in AEDC Wind Tunnels." AEDC-TR-70-101 (AD871321), July 1970.

10. Barnett, D. O. and Giel, T. V., Jr. "Broadening of LV Turbulence Measurements Due to the Dynamics of a Particle Ensemble." Proceedings of the Fifth Biennial Symposium on Turbulence, University of Missouri-Rolla, 1977.
11. Keyser, D. R. "Laser Flow Measurement." ASME Paper 77-WA/FM-2, Presented at the Winter Annual Meeting, Atlanta, Georgia, 1977.
12. Durst, F. and Whitelaw, J. H. "Theoretical Considerations of Significance to the Design of Optical Anemometers." ASME Paper No. 720-HT-7, Heat Transfer Conference, Denver, Colorado, 1972.
13. Meadows, D. M., Whiffen, M. C., and Mayo, W. T., Jr. "Laser Velocimeter for Supersonic Jet Turbulence and Turbulence Spectra Research." AFAPL-TR-74-24, Appendix IV, 1974, pp. 163-189.
14. Durst, F. and Stevenson, W. H. "Properties of Focused Laser Beams and the Influence on Optical Anemometer Signals." Proceedings of the Minnesota Symposium on Laser Anemometer, University of Minnesota, October, 1975, pp. 373-388.
15. Brayton, D. B. Kalb, H. T., and Crosswy, F. L. "A Two-Component Dual-Scatter Laser Doppler Velocimeter with Frequency Burst Signal Readout." Applied Optics, Vol. 12, No. 6, June 1973, pp. 1145-1156.
16. Kalb, H. T. and Cline, V. A. "New Techniques in the Processing and Handling of Laser Velocimeter Burst Data." Review of Scientific Instruments Vol. 47, No. 6, June 1976, pp. 708-711.

17. Durst, F., Melling, A., and Whitelaw, J. H. Principles and Practice of Laser Doppler Anemometry. Academic Press, N. Y., 1976.
18. Mayo, W. T., Jr. "The Development of New Digital Data Processing Techniques." USAF Contract F70600-73-C-003, Third Monthly Progress Report, Appendix, March 1973.
19. McLaughlin, D. K. and Tiederman, W. G. "Biasing Correction for Individual Realization of Laser Anemometer Measurements in Turbulent Flows." The Physics of Fluids, Vol. 16, No. 12, December 1973.
20. Barnett, D. O. and Bentley, H. T., III. "Bias of Individual Realization Laser Velocimeters." Proceedings of the Second International Workshop on Laser Velocimetry, Purdue University, Vol. I, 1974, pp. 428-442.
21. Kreid, D. K. "Laser Doppler Velocimeter Measurements in Non-Uniform Flow: Error Estimates." Applied Optics, Vol. 13, August 1974, pp. 1872-1881.
22. George, W. K., Jr. "Limitations of Measuring Accuracy Inherent in the Laser Doppler Signal." The Accuracy of Flow Measurements by Laser Doppler Methods, Proceedings of the LDA Symposium, Copenhagen, Technical University of Denmark, August 1975, pp. 20-63.
23. Owen, J. M. and Rogers, R. H. "Velocity Biasing in Laser Doppler Anemometers." The Accuracy of Flow Measurements by Laser Doppler Methods, Proceedings of the LDA-Symposium, Copenhagen, Technical University of Denmark, August 1975, pp. 89-114.

24. Buchhave, P. "Biasing Errors in Particle Measurements." The Accuracy of Flow Measurements by Laser Doppler Methods, Proceedings of the LDA-Symposium, Copenhagen, Technical University of Denmark, August 1975.
25. Durao, D. F. G. and Whitelaw, J. H. "The Influence of Sampling Procedures on Velocity Bias in Turbulent Flows." The Accuracy of Flow Measurements by Laser Doppler Methods, Proceedings of the LDA-Symposium, Copenhagen, Technical University of Denmark, August 1975.
26. Karpuk, M. E. and Tiederman, W. G. "Effect of Finite-Size Probe Volume upon Laser Doppler Anemometer Measurements." AIAA Journal, Vol. 14, August 1976, pp. 1099-1105.
27. Quigley, M. S. and Tiederman, W. G., Jr. "Experimental Evaluation of Sampling Bias in Individual Realization Laser Anemometry." AIAA Journal, Vol. 15, February 1977, pp. 266-268.
28. Thermo-Systems, Inc. "Laser Anemometer Systems." TSI 900-477-5M, 1978.
29. Farmer, W. M. "The Interferometric Observation of Particle Size, Velocity, and Number Density." PhD Dissertation, University of Tennessee, Knoxville, 1973.
30. Roberds, D. W. "Electronic Instrument for Interferometric Particle Sizing." PhD Dissertation, University of Tennessee, Knoxville, December 1975.

31. Crosswy, F. L. and Hornkohl, J. O. "Signal-Conditioning Electronics for a Vector Velocity Laser Velocimeter." AEDC-TR-72-192 (AD755842), February 1973.
32. Fridman, J. D., Young, R. M., Seavey, R. E., and Orloff, K. L. "Modular High Accuracy Tracker for Dual Channel Laser Doppler Velocimeter." Proceedings of the Minnesota Symposium on Laser Anemometry, University of Minnesota, October 1975, pp. 485-503.
33. Adrian, R. J. and Earley, W. L. "Evaluation of LDV Performance Using MIE Scattering Theory." Proceedings of the Minnesota Symposium on Laser Anemometry, University of Minnesota, October 1975, pp. 426-254.
34. Chu, W. P. and Robinson, D. M. "Scattering from a Moving Spherical Particle by Two Crossed Coherent Plane Waves." Applied Optics, Vol. 16, March 1977, p. 619.
35. Andrews, D. G. and Seifert, H. S. "Investigation of Particle-Size Determination from the Optical Response of the Laser-Doppler Velocimeter." Stanford University Department of Aeronautics and Astronautics Report. 435, Palo Alto, California, November 1971.
36. Pfeifer, H. J. and Von Stein, H. D. "Application of the Laser Velocimeter in Supersonic Wind Tunnel." Opto-Electronics, Vol. 5, 1973, p. 53.
37. Hinze, J. O. Turbulence. McGraw-Hill, Inc., New York, 1959.
38. Sami, S. "Velocity and Pressure Fields in a Diffusing Jet." PhD Dissertation, University of Iowa, 1966.

39. Glass, M. and Kennedy, I. M., "An Improved Seeding Method for High Temperature Laser Doppler Velocimeters." Combustion and Flame, Vol. 29, 1977, pp. 333-335.
40. Berglund, R. N. "Basic Aerosol Standards and Optical Measurements of Aerosol Particles." PhD Dissertation, Mechanical Engineering Department, University of Minnesota, 1972.
41. Cline, V. A. and Bentley, H. T., III. "Application of a Dual Beam Laser Velocimeter to Turbulent Flow Measurements." AEDC-TR-74-56 (AD785352), September 1974.
42. Abernethy, R. B., et al., Pratt and Whitney Aircraft, and Thompson, J. W., Jr., ARO, Inc. "Handbook of Uncertainty in Gas Turbine Measurements." AEDC-TR-73-5 (AD755356), February 1973.
43. Bruun, H. H. "A Note on the Static and Dynamic Calibration of Constant-Temperature Hot-Wire Probes." Journal of Fluid Mechanics, Vol. 76, Part 1, 1976, pp. 145-155.
44. Bruun, H. H. "Linearization and Hot-Wire Anemometry." Journal of Scientific Instruments, Vol. 4, 1971, pp. 815-820.
45. Hartley, H. O. "The Modified Gauss-Newton Method for the Fitting of Non-Linear Regression Functions by Least Squares." Technometrics, Vol. 3, 1961, pp. 269-280.
46. Champagne, F. H. and Sleicher, C. A. "Turbulent Measurements with Inclined Hot-Wires." Journal of Fluid Mechanics, Vol. 28, p. 182.

47. Berglund, G. D. "A Fast Fourier Transform Algorithm for Real-Valued Series." Communications of the ACM, Vol. 11, No. 10, October 1968.
48. Dimotakis, P. E. "Single Scattering Particle Laser Doppler Measurements of Turbulence." AGARD-CP-193, Applications of Non-Intrusive Instrumentation in Fluid Flow Research, Saint Louis, France, May 1976, pp. 10-1 to 10-14.
49. Stanford, R. A. and Libby, P. "Further Applications of Hot Wire Anemometry to Turbulence Measurements in Helium Air Mixtures." Project Squid Technical Report USCD 5PU, West Lafayette, Indiana, January 1974.
50. Crosswy, F. L. and Brayton, D. B. "Design and Evaluation of a Laser Doppler Velocimeter for the AEDC-PWT 4-Ft Transonic Tunnel." AEDC-TR-78-30, July 1978.
51. Holve, D. and Self, S. A. "An Optical Particle-Sizing Counter for In-Situ Measurements" Project Squid Technical Report SU-2-PU, West Lafayette, Indiana, January 1978.
52. Mie, G. "Beitrage zur Optik Truber Medien." Annalen der Physik, Vol. 25, 1908, pp. 377-445.
53. van de Hulst, H. C. Light Scattering by Small Particles. John Wiley and Sons, New York, 1959.
54. Born, M. and Wolf, E. Principles of Optics. Pergamon Press, Oxford, 1959.
55. Kerker, M. The Scattering of Light and Other Electromagnetic Radiation. Academic Press, New York, 1969.

56. Denman, H. H., Heller, W., and Panconis, W. T. Angular Scattering Functions for Spheres. Wayne State University Press, Detroit, 1966.
57. Howell, H. B. "Angular Scattering Functions for Spherical Water Droplets." Naval Research Laboratory Technical Report NRL R-6955 (AD698492), Washington, D. C., October 1969.
58. Dave, J. V. "Subroutines for Computing the Parameters of the Electromagnetic Radiation Scattered by a Sphere." IBM Report 320-3237, May 1968.
59. Lewis, J.W.L., Curry, B. P., and Weaver, D. P. "Determination of the Size Distribution Function for Particles in a Hypersonic Flow Field." AEDC-TR-77-101 (AD-A056923), July 1978.
60. Weast, R. C., editor. Handbook of Chemistry and Physics. Chemical Rubber Publishing Co., Cleveland, Ohio, 57th Edition, 1977.
61. Plass, G. N. "Mie Scattering and Absorption Cross Sections for Aluminum Oxide and Magnesium Oxide." Applied Optics, Vol. 3, No. 17, July 1964.
62. Rudd, M. J. "A Self-Aligning Laser Doppler Velocimeter." Optical Instruments and Techniques, 1969, pp. 158-166.
63. Wieser, P., Stolzenburg, M., and Baum Mueller, J. "Aerosol Particles: Remarks on the Optical Properties." Applied Optics, Vol. 13, October 1977.

64. Brayton, D. B. "Small Particle Signal Characteristics of a Dual-Scatter Laser Velocimeter." Applied Optics, Vol. 13, October 1974, pp. 2346-2351.
65. RCA Corporation. Photomultiplier Manual. Technical Series, PT-61, Harrison, N. J., 1970.
66. Taylor, G. I. "Diffusion by Continuous Movements." Proceedings of the London Mathematical Society, Ser. 2, Vol. 20, 1921, p. 196.
67. Kampe de Fariet, J. "Stationary Contingent Functions and the Statistical Theory of Homogeneous Turbulence." Annales de la Societ  Scientifique Bruxelles, Ser. I., Vol. 59, 1939, pp. 145-194.
69. Tennekes, H. and Lumley, J. L. A First Course in Turbulence. The MIT Press, Cambridge, Massachusetts, 1972.

APPENDIX A RELATIONSHIP BETWEEN LONG- AND SHORT-TERM AVERAGES

In pulsating flows the temporal mean velocity, \hat{V}_1 , over time interval, Δt_1 , may differ from the temporal mean velocity, V , defined over an infinitely long time interval. The difference between the mean velocities is given by

$$\widehat{(\hat{V}_1 - V)} = \lim_{T \rightarrow \infty} \frac{1}{T} \int_{s_0}^{s_0+T} (\hat{V}_1 - V) ds \quad (A-1)$$

The variance or mean-square value of this difference is

$$\begin{aligned} \widehat{(\hat{V}_1 - V)^2} &= \lim_{T \rightarrow \infty} \frac{1}{T} \int_{s_0}^{s_0+T} (\hat{V}_1 - V)^2 ds \\ &= \lim_{T \rightarrow \infty} \frac{1}{T} \int_{s_0}^{s_0+T} \left(\frac{1}{\Delta t_1^2} \int_{t_0}^{t_0+\Delta t_1} (V - \hat{V}) dt \int_{t'_0}^{t'_0+\Delta t_1} (V - \hat{V}) dt' \right) ds \end{aligned} \quad (A-2)$$

Assuming that the velocity, $V(t)$, is statistically stationary, rearranging the order of integration, and performing a Reynolds decomposition of the velocity, gives

$$\widehat{(\hat{V}_1 - V)^2} = \frac{1}{\Delta t_1^2} \int_0^{\Delta t_1} \int_0^{\Delta t_1} \left(\lim_{t \rightarrow \infty} \frac{1}{t} \int_0^t v(s) v(s') ds \right) dt dt' \quad (A-3)$$

where $v(t)$ is the velocity fluctuation about \hat{V} . The integration in the (t, t') plane is over a square with limits 0 and t . Since the integrand is symmetrical in t and t' , the double integration can be replaced with twice the single integration over the triangle that is half the square. This leads to,

$$\widehat{(\hat{V}_i - \hat{V})^2} = \frac{2}{\Delta t_i^2} \int_0^{\Delta t_i} \left[\int_0^{t'} \left(\lim_{t \rightarrow \infty} \frac{1}{t} \int_0^{t'} v(s) v(s') ds \right) dt' \right] dt \quad (A-4)$$

To alter the form of the integrand in Eq. (A-4) the difference, $s' - s$, is defined as τ , so that Eq. (A-4) can be written

$$\widehat{(\hat{V}_i - \hat{V})^2} = \frac{2}{\Delta t_i^2} \int_0^{\Delta t_i} \left[\int_0^{t'} \left(\lim_{t \rightarrow \infty} \frac{1}{t} \int_0^{t'} v(s) v(s + \tau) ds \right) dt' \right] dt \quad (A-5)$$

The integrand is now recognized as the velocity autocorrelation, defined in coefficient form as

$$R(\tau) = \frac{1}{\bar{v}^2} \lim_{T \rightarrow \infty} \frac{1}{T} \int_0^T v(t) v(t + \tau) dt \quad (A-6)$$

Substituting Eq. (A-6) into Eq. (A-5) gives

$$\widehat{(\hat{V}_i - \hat{V})^2} = \frac{2\bar{v}^2}{\Delta t_i^2} \int_0^{\Delta t_i} \left(\int_0^{t'} R(t') dt' \right) dt \quad (A-7)$$

Equation (A-7) can be integrated in parts, using Leibnitz' rule, to give

$$\widehat{(\hat{V}_i - \hat{V})^2} = \frac{2\bar{v}^2}{\Delta t_i} \int_0^{\Delta t_i} R(\tau) \left(1 - \frac{\tau}{\Delta t_i} \right) d\tau \quad (A-8)$$

This relation is given by Hinze (Ref. 37) who credits Taylor (Ref. 66), and Kampe de Fariet (Ref. 67). The relation is also given by Tennekes and Lumley (Ref. 68).

APPENDIX B MIELV PROGRAM

A program (MIELV) was written to determine the characteristics of laser velocimeter (LV) signals and photomultiplier tube (PMT) signal-to-noise (S/N) ratio. A general Mie scattering routine (SUBROUTINE CALC) provided the Mie scattering functions. In particular, MIELV computes (1) the Mie scattering characteristics of spherical particles traversing a plane electromagnetic wave in an isotropic medium, (2) the scattered energy incident on a collector lens located in a spherical coordinate system with the origin at the particle center, (3) the amplification and attenuation of the signal by the PMT amplifiers and laser line filters typical of LV systems used at AEDC, and (4) the S/N ratio and visibility of the resulting LV signals.

It is assumed that the Mie scattering characteristics of a dual-scatter LV can be represented by the scattering from an equivalent single beam of uniform intensity. The Probe Volume Intensity Program (PVIP, Appendix C) was developed to estimate the equivalent intensities. No restrictions are placed on particle or medium refractive indices or collector optics viewing angle. It is further assumed that the amplification of the LV signal by the LV electronics is a linear process. Both the single-beam model and the S/N ratio calculations assume that the half-angle between the intersecting beams forming the LV probe volume is less than 3 deg. In addition, only flat lenses are considered and the product of refractive index and particle size parameter, β , is restricted to values less than 1,000.

MIELV is based on the theoretical considerations described in detail in Section 3.0, with the exception of the integration of the scattering intensity over the system collector lens. This integration is performed over a disk of radius R (representing the lens) by applying the trapezoidal rule to a grid network of 11 x 11 points. The grid is

defined in a Cartesian coordinate system (x,y,z) with its origin at the center of the lens, and the grid spacing is set to $\Delta X = R/5$ to define grid points

$$\begin{aligned}x_{ij} &= -R + (i - 1) \Delta X \\y_{ij} &= -R + (j - 1) \Delta X\end{aligned}\tag{B-1}$$

If a grid point falls outside the disk, new coordinates for that point are defined by

$$\begin{aligned}x_{ij} &= \begin{cases} \sqrt{R^2 - y_{ij}^2} & : 2 \leq i \leq 10 \text{ and } j > 5 \\ -\sqrt{R^2 - y_{ij}^2} & : 2 \leq i \leq 10 \text{ and } j \leq 5 \end{cases} \\y_{ij} &= \begin{cases} \sqrt{R^2 - x_{ij}^2} & : i = 1 \text{ or } 11 \text{ and } j > 5 \\ -\sqrt{R^2 - x_{ij}^2} & : i = 1 \text{ or } 11 \text{ and } j \leq 5 \end{cases}\end{aligned}\tag{B-2}$$

Each grid point on the lens is converted from the Cartesian coordinate system (x,y,z) , with origin at the center of the lens, to a spherical coordinate system (r,θ,ϕ) with origin at the particle center, as pictured in Fig. B-1. The lens is assumed to be tangent to the sphere that passes through $(L,\theta_\ell,\phi_\ell)$. The coordinates of each grid point are determined with the relations

$$\begin{aligned}x^* &= L \sin \theta - y \cos \theta \\y^* &= x \\z^* &= L \cos \theta - y \sin \theta \\r^* &= \sqrt{x^{*2} + y^{*2} + z^{*2}} \\\theta^* &= \tan^{-1} \left(\frac{\sqrt{x^{*2} + y^{*2}}}{z^*} \right) \\\phi^* &= \phi + \tan^{-1} \left(\frac{y^*}{x^*} \right)\end{aligned}\tag{B-3}$$

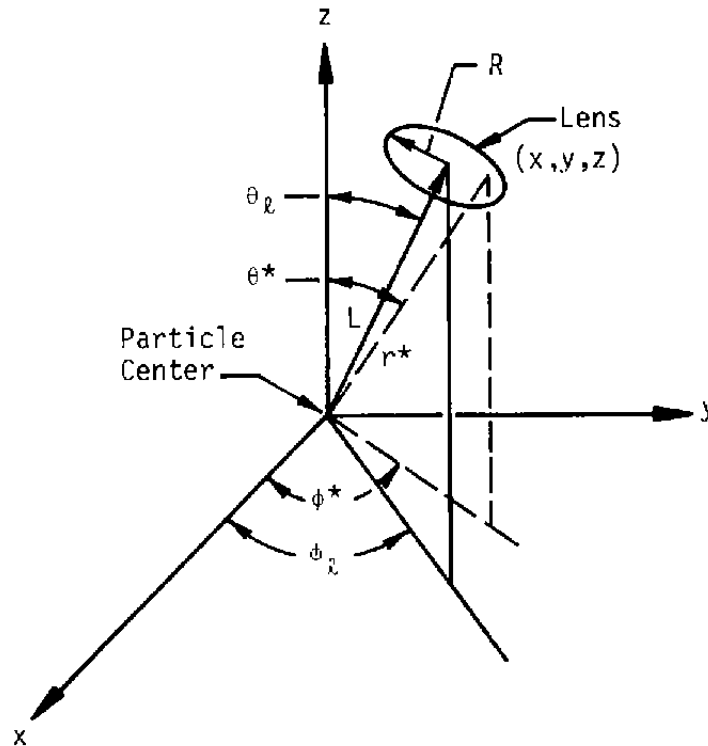


Figure B-1. Scattering coordinate system.

With the point (r^*, θ^*, ϕ^*) , evaluation of functions f_1 and f_2 is performed, where f_1 and f_2 are defined by

$$\begin{aligned} f_1 &= i_{\perp} \sin^2 \phi^* \frac{L}{r^{*3}} \\ f_2 &= i_{\parallel} \sin^2 \phi^* \frac{L}{r^{*3}} \end{aligned} \quad (\text{B-4})$$

After evaluating f_1 and f_2 at all 121 grid points, the program next does the trapezoidal integration by summing up the volumes of elements as shown in Fig. B-2.

The element volumes are given by the relation

$$v = dx \, dy (f_{ij} + f_{i-1, j} + f_{i-1, j-1} + f_{i, j-1}) \quad (\text{B-5})$$

where

$$\begin{aligned} 2dx &= (x_{ij} - x_{i-1, j} + x_{i, j-1} - x_{i-1, j-1}) \\ 2dy &= (y_{ij} - y_{i, j-1} + y_{i-1, j} - y_{i-1, j-1}) \end{aligned} \quad (\text{B-6})$$

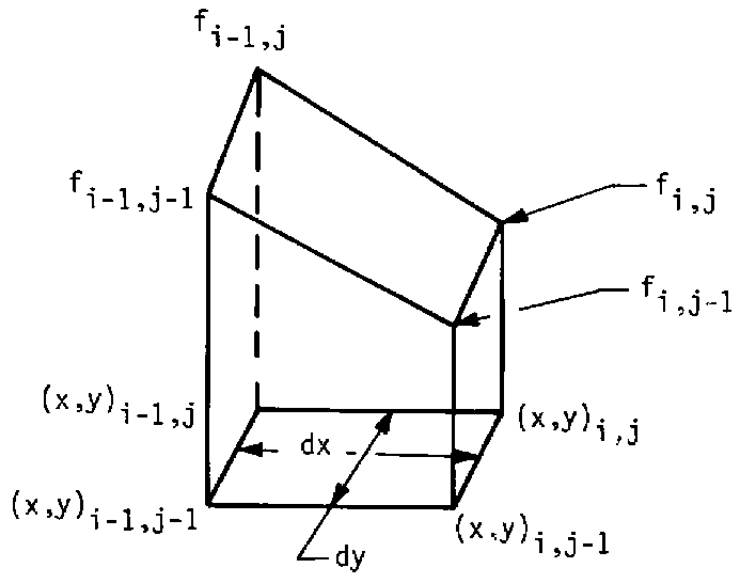


Figure B-2. Trapezoidal integration volumes.

All the volumes are summed to approximate the integrals over the solid collection angle:

$$\int i_{\perp} \sin^2 \phi^* dw \quad (\text{B-7})$$

$$\int i_{\parallel} \sin^2 \phi^* dw \quad (\text{B-8})$$

where the i_{\perp} and i_{\parallel} intensity functions are evaluated at the center of the lens. These integrals are used to evaluate the total energy scattered from the particle onto the collector lens, as

$$E_c = I_1 + I_2 \quad (\text{B-9})$$

where

$$I_1 = \frac{4N_f \eta P_L}{\pi d_p^2} \left(\frac{\lambda}{2\pi 10^4} \right) \int i_{\perp} \sin^2 \phi^* dw \quad (\text{B-10})$$

$$I_2 = \frac{4N_f \eta P_L}{\pi d_p^2} \left(\frac{\lambda}{2\pi 10^4} \right) \int i_{\parallel} \sin^2 \phi^* dw \quad (\text{B-11})$$

The total energy reaching the PMT photocathode is then evaluated using

$$F = E_c \cdot T_1 \quad (\text{B-12})$$

and the PMT anode current is determined from

$$i_a = H_G \cdot F \quad (B-13)$$

However, if i_a is greater than the saturation limit of the PMT, i_a is set to the saturation limit. The total signal amplitude is given as

$$e_d = i_a \cdot R_e \quad (B-14)$$

Next, the theoretical signal-to-noise ratio and particle velocity product is determined from

$$(S/N) \cdot V = F_1 F_2 J_1^2 (\pi d_p \times 10^{-4} / K_\delta) \left(\frac{k_\perp + k_\parallel}{2} \right) \quad (B-15)$$

where

$$F_1 = \eta G^* T / [(6.6 \times 10^{34}) (3 \times 10^{14})] \quad (B-16)$$

$$F_2 = E_c \Omega_c \lambda K_\delta^3 \quad (B-17)$$

with

$$\Omega_c = \frac{\pi R^2}{L^2} \quad (B-18)$$

$$G^* = \frac{G^{2n} (G - 1)}{G^n (G^{n+1} - 1)} \quad (B-19)$$

and where $k_\perp = i_\perp$ evaluated at the lens center for $\theta = 0$, whereas $k_\parallel = i_\parallel$ evaluated at the lens center for $\theta = 0$. Finally, the theoretical particle visibility is calculated from

$$F_3 = \frac{J_1 (\pi d_p \times 10^{-4} / K_\delta)}{\pi d_p \times 10^{-4} / K_\delta} \quad (B-20)$$

The preceding relations form the basis for MIELV which was programmed in Fortran IV for an IBM 370/165 computer. Detailed documentation on the program is available upon request from the Commander, AEDC, ATTN: ACI.

APPENDIX C PROBE VOLUME INTENSITY PROGRAM (PVIP)

This program obtains the local illuminating intensity in the probe volume of a dual-scatter laser velocimeter, as well as various average intensity values for the fringe model of Ref. 64. According to the theory, the probe volume must be formed by the intersection of two equal-intensity laser beams each having a Gaussian light distribution and similar polarization and intersecting at a small angle. In particular, the probe volume is assumed to be an ellipsoid as in Fig. C-1.

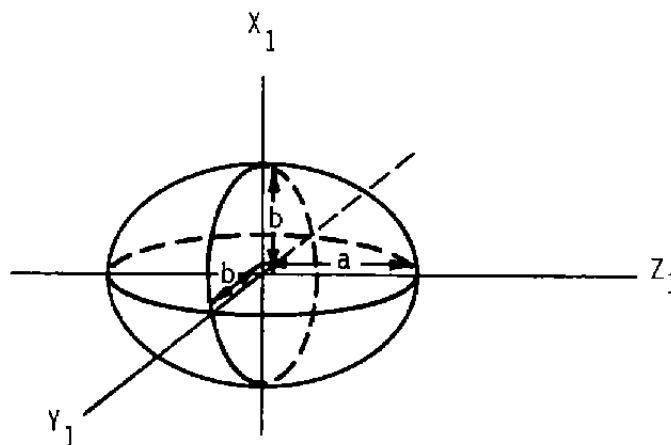


Figure C-1. Ellipsoid probe volume.

The volume of this ellipsoid is known analytically ($V_p = \frac{4}{3} \pi ab^2$), and the accuracy of the numerical integration can be checked by comparing

$$V_P = \int_{-a}^a \left[\int_{-b\sqrt{1-\left(\frac{Z_1}{a}\right)^2}}^{b\sqrt{1-\left(\frac{Z_1}{a}\right)^2}} \int_{-b\sqrt{1-\left(\frac{Y_1}{b}\right)^2-\left(\frac{Z_1}{a}\right)^2}}^{b\sqrt{1-\left(\frac{Y_1}{b}\right)^2-\left(\frac{Z_1}{a}\right)^2}} dX_1 dY_1 dZ_1 \right] \quad (C-1)$$

to the analytical result.

The average intensity in the probe volume, as given in Section 3.1.2, Eq. (77), is

$$\hat{I} = \iiint_{V_P} I^* \left(\frac{X_1}{b}, \frac{Y_1}{b}, \frac{Z_1}{a} \right) dX_1 dY_1 dZ_1 / V_P \quad (C-2)$$

where

$$I^* (X_1^*, Y_1^*, Z_1^*) = I / I_0 = \left[\cosh (4Y_1^* Z_1^*) + \cos (X_1^* \pi Y_1^*) \right] e^{-2[X_1^{*2} + Y_1^{*2} + Z_1^{*2}]} \quad (C-3)$$

with $X_1^* = X_1/b$, $Y_1^* = Y_1/b$, and $Z_1^* = Z_1/a$

Also, the most probable intensity is given in Section 3.1.2, Eq. (79),

$$\langle I \rangle = \frac{\int \bar{I}^* \left(\frac{Z_1}{a} \right) f \left(\frac{Z_1}{a} \right) dZ_1}{\int f \left(\frac{Z_1}{a} \right) dZ_1} \quad (C-4)$$

where

$$\bar{I}^* \left(\frac{Z_1}{a} \right) = \frac{\int_{Y_1} \int_{X_1} I^* \left(\frac{X_1}{b}, \frac{Y_1}{b}, \frac{Z_1}{a} \right) dX_1 dY_1}{\int_{Y_1} \int_{X_1} dX_1 dY_1} \quad (C-5)$$

with

$$f \left(\frac{Z_1}{a} \right) = \frac{2}{\pi} \sqrt{1 - \left(\frac{Z_1}{a} \right)^2} \quad (C-6)$$

The program calculates illuminating intensity at various Z_1^* locations as Y_1^* varies along the probe volume axis from Eq. (C-3). Then the average intensity is calculated as it varies along Z_1^* , from Eq. (C-5).

All integration is accomplished by means of 16-point Gaussian quadrature. The triple integration is performed by a 16-point Gaussian quadrature embedded within a 16-point Gaussian quadrature which itself is embedded within a 16-point Gaussian quadrature. Because of the oscillatory nature of I , the integration over Y is divided into M equal intervals, each of which is performed by a 16-point Gaussian quadrature where

$$M = \frac{NN}{7} + 1 \quad (C-7)$$

This formula was derived after examining results over a range of NN values from 1 to 50.

The preceding relations are incorporated in PVIP which was programmed in Fortran IV for an IBM 370/165 computer. Detailed computer program documentation is available, upon request, from the Commander, AEDC, ATTN: ACD.

NOMENCLATURE

A	Cross-sectional area of probe volume
A, B, C	Constants, Eq. (37)
$A(X), B(X), C(X)$	Constants, Eq. (39)
A_n, B_n	Scattering amplitude coefficients, Eqs. (62) and (63)
a	Semiminor axis of probe volume, Eq. (75)
b	Waist radius of laser beam
$b(X)$	Mixing layer half width, Eq. (38)
c_p	Fluid specific heat at constant pressure
D	Jet exit diameter
d_p	Particle diameter
\vec{E}	Electric field vector
E_c	Rate energy is received by collector, Eq. (68)
e	Exponential (2.71828...), or hot-wire output, Eq. (37)
e_d	Detected voltage, Eq. (82)
e_s	Supply voltage to PMT

$F_1, F_2, F_3,$	Functions, Appendix B
$F(\theta, \phi)$	Angular scattering amplitude function
f	Measured velocity moment, Eq. (1) or lens parameter
$f()$	Probability density function, Eq. (78)
$\langle f \rangle$	Arithmetic average velocity moment, Eq. (3)
f_D	Frequency of particle fringe crossings
f_o	Bragg system reference frequency
f_1, f_2	Functions, Eq. (B-4)
G_i	Stage amplification
G^*	Gain relation, Eq. (B-19)
g_c	Gravitational acceleration
\vec{H}	Magnetic field vector
H_G	PMT transfer function, Eq. (85)
h	Constant, Eq. (37)
I	Illuminating light intensity
I_o	Peak single beam light intensity, Eq. (73)
\hat{I}	Average probe volume light intensity, Eq. (77)

I^*	Nondimensional illuminating light intensity, Eq. (76)
\bar{I}^*	Average intensity along the constant Z_1^* planes, Eq. (80)
$\langle I \rangle$	Most probable probe volume intensity, Eq. (79)
$\langle I_{\max} \rangle$	Most probable maximum probe volume intensity, Eq. (81)
$i_{\perp}(\theta), i_{\parallel}(\theta)$	Scattering intensity functions, Eqs. (66) and (67)
i_A	LV signal current, Eq. (83)
$\vec{i}, \vec{j}, \vec{k}$	Unit vectors
J	Scattered light intensity, Eq. (55)
J_c	Energy unit conversion from Btu to ft-lbf, Eq. (36)
J_n	Bessel function of the first kind
K	Kurtosis, Eq. (35)
K_{δ}	Fringe spacing
k_t	Processing delay time
L	Distance from probe volume to collector lens
L_T	Integral time scale, Eq. (13)

M	Number of samples in a data set or stages of amplification or integer, Eq. (C-10)
m	Refractive index ratio
m_1	Particle refractive index
m_2	Medium refractive index
N	Particle number density or stages of attenuation
NN	Integer, Appendix C
N_f	Number of fringes in the $Z_1^* = 0$, probe volume plane
n	Summation index
P	Pressure, Eq. (36), or point location, Fig. 25
$P()$	Probability
P_L	Laser power
$P_n()$	Legendre polynomials
$Q_n()$	Riccati-Bessel function, Eq. (64)
R	Collector lens radius
$R(\tau)$	Velocity autocorrelation coefficient, Eq. (11)
R_e	LV circuit resistance

$R_{f\Delta t}$	Correlation coefficient, Eq. (7)
R_{NV^n}	Correlation coefficient, Eq. (53)
$R_{V\Delta t}$	Correlation coefficient, Eq. (43)
$R_{V\Delta t*}$	Correlation coefficient for processing delays
r	Radial dimension
$r_o(X)$	Radius of jet core
r_p	Particle radius
r_σ	Core radius for turbulence intensity curve fit, Eq. (39)
S	Skew coefficient, Eq. (23)
\vec{S}	Poynting flux vector
S_c	Collector lens surface area
S_K	Number of realizations in an interval, Eq. (49)
S_M	Number of samples
S_\perp, S_\parallel	Complex amplitude functions, Eqs. (58) and (59)
s	Variable of integration, Appendix A
T	Time interval, Eq. (1)

T_j	Stage attenuation
T_t	Sampling time
\dot{T}	Temperature
t	Time
t_o	Initial time
U	Velocity in the main flow direction
U_o	Jet exit velocity
u,v,w	Fluctuating velocity components
V	Velocity
\hat{V}_i	Temporal mean velocity over interval Δt_i
V_p	Volume of probe volume region
$ \vec{V} $	Velocity magnitude, Eq. (25)
$\langle V \rangle$	Arithmetic average velocity
\hat{V}_i	Mean velocity over the interval Δt_i
V_o, V_1	Sinusoidal velocity parameters, Fig. 20b
X	Axial location from nozzle exit
X_1, Y_1, Z_1	Probe volume coordinate system, Fig. 33

X_1^*, Y_1^*, Z_1^*	Nondimensional probe volume coordinates
x, y, z	Cartesian coordinate system, Fig. 25
x^*	Function
α, β, γ	Error coefficients, Eqs. (30-32)
α	Particle size parameter
α_i	Velocity parameter, Eq. (27)
β	Particle characterizing parameter
γ	Ratio of specific heats, Eq. (36)
ΔP	Differential pressure, Eq. (36)
Δt	Time interval between realizations
Δt^*	Delay time after acquiring a data point, Eq. (40)
$\langle \Delta t \rangle$	Arithmetic average time interval
Δu_i	Velocity precision, Eq. (29)
$\Delta \langle V \rangle$	Confidence interval for the mean, Eq. (33)
ΔX	Finite step size, Appendix B
δN	Number of particles entering probe volume, Eq. (8)
η	Fraction of laser power reaching the probe volume

θ	Convergence angle of laser beams, Fig. 1, or scattering angle, Fig. 25
λ	Wavelength
λ_K	Sampling rate
Π	Series multiplication
π	Irrational number (3.141592...)
π_n	Angular dependence function, Eq. (60)
ρ	Fluid density
Σ	Summation
σ_v	Time-integrated turbulence intensity, Eq. (21)
$\sigma_{<v>}$	Arithmetic average turbulence intensity
$\Delta\sigma_{<v>}$	Confidence interval for the intensity, Eq. (34)
τ	Time difference, Eq. (10), or Doppler burst period, Eqs. (30)-(32)
τ_n	Angular dependence function, Eq. (61)
ϕ_n	Riccati-Bessel function, Eq. (65)
ϕ	Phase angle, Fig. 20b, or scattering coordinate, Fig. 25

Ω_c Collector solid angle

ω Frequency, Fig. 20b

SUBSCRIPTS

a Ambient

C_L Centerline

c Cell gage conditions

i,j,k Indices

max Maximum

r, s Summation indices, Eq. (18)

\perp Perpendicular component

\parallel Parallel component

SUPERSCRIPTS

- Approximate-time-integrated average, Eq. (2)

\wedge True time-integrated average, Eq. (1)

\prime Fluctuating component